博士論文

Blind Deconvolution of 3D Fluorescence Microscopy using Depth-variant Asymmetric PSF

(奥行き可変非対称 PSF を用いた 3 次元蛍光顕微鏡画像のブラインドデコンボリューション)

2015/12/11
Supervisor: Prof. Takeshi Naemura

Graduate School of Information
Science and Technology,
The University of Tokyo

48-127404
金 甫映

Abstract

Three-dimensional (3D) fluorescence wide-field microscopy (WFM) is widely used in biomedical research since 3D observation of cellular structure is possible with high contrast. The 3D WFM images are obtained by piling up 2D images of different in-focus planes. However, there is a problem that an out-of-focus blur obscures the in-focus detail. Restoration of a clear object image of 3D WFM has been challenged.

For the purpose, this thesis gives importance to implement practical deconvolution and improving accuracy of PSF estimation. The practical deconvolution means an implementation of the deconvolution that has an appropriate imaging model with a convergence guarantee on a PC. The practical deconvolution enables to estimate accurate object image with computational cost expectation.

Also, improving accuracy of PSF estimation in this thesis is directly connected to reflect WFM blur properties. WFM lens is designed to focus the specimen plane right above a microscopy stage with the refractive index of immersion layer. However, the 3D WFM observes planes inside specimen; the refractive index of specimen causes peculiar problems. First, the blur varies according to depth. As WFM focuses to deeper plane of specimen, refractive index mismatch between immersion and specimen layer causes severer blur. This causes the elongation in the axial axis. Second, the PSF is specimen-dependent. Even if the pre-measured point spread function (PSF) is given, the PSF is not accurate since the refractive index and the focal distance of the point-like object for pre-measuring and those of the actual specimen are different, which indicates that PSF pre-measurement is useless. Moreover, even if it is in perfect imaging conditions, an imperfection of lens causes asymmetric blur. Based on practical deconvolution for WFM, this thesis solves these problems through depth-variant algorithm, blind deconvolution and asymmetric PSF model utilization. Namely, this thesis covers the main causes of blur in WFM imaging condition and optical system design.

Chapter 3 proposes depth-variant deconvolution. For practical deconvolution, generalized expectation maximization algorithm is introduced and applied to WFM under depth-variant imaging model. PSF is estimated by fitting parameters of the theoretical PSF to the pre-measured PSF. From comparison among existing deconvolution methods, it is proven that the GEM has superior and practical deconvolution method. A normalized correlation coefficient (COR) value between true object image and deconvolution image is used for evaluation. However, the deconvolution result shows that the axial blur is not perfectly suppressed in actual image; the author supposed that the remained blur is caused by the inaccuracy of the pre-measured PSF.

Chapter 4 focuses the inaccuracy of the pre-measured PSF. The inaccuracy occurs since the refractive index and the focal distance vary when users switch the point-like object for pre-measuring into the actual specimen. In this work, I propose the blind deconvolution - the estimation parameters of equation based PSF from the observed image. While Chapter 3 fits parameters to the pre-measured PSF, Chapter 4 fits parameters to the obtained PSF from the observed image. Experiments are implemented using the opened data of micro-bead image, which enables to compare performances to previous algorithms. Since blind deconvolution does not have the true image, the COR cannot be used as evaluation indicators. The micro-bead has determined diameter and hollow sphere shape; therefore, the diameter and the relative contrast between shell and hollow inside can be used for performance indicators. From the indicators, the author proves that the second work completely suppresses the remained blur. However, despite the symmetric sphere shape of the micro-bead, the deconvolution result shows the asymmetric shape.

Chapter 5 focuses the asymmetric result. The asymmetric result alludes that the blur has an asymmetric shape. The author proposes a blind deconvolution using depth-variant asymmetric PSF. While the theoretical PSF model used in the first and the second work considers axial asymmetric but $x-y$ symmetric blur that specimen causes, the third work utilizes xyz asymmetric PSF that not only the specimen but also lens aberrations cause. In this work, the author devised new performance indicators to evaluate symmetry of deconvolution results. Standard deviation values of diameter and shell intensities along x, y and z axis are used as new indicators. This chapter compares performances by indicators that are used in Chapter 4 and the new indicators, which are conducted using the opened data of micro-bead image. Qualitatively, the deconvolution result images show that asymmetric distortions are removed. Quantitatively, while transversal, axial diameter error and contrast in existing method are $236nm$, $477nm$ and 88%, ours have $180nm$, $84nm$ and 98% values. These results show the third work generates superior performances. Also, standard deviation values of diameter and relative contrast for symmetry evaluation are $143nm$ and 4.4%, which are better than $198nm$ and 12.8% values in second work and show that the asymmetry is corrected. Finally, with deconvolution results, the author summarizes deconvolution quality, computational cost according to deconvolution methods, which would be a helpful guide for 3D WFM users.

Differences in performance among three works can basically explain different characteristics of WFM blur. Reflecting characteristics of blur is significantly important key for determining the quality of the deconvolution result.

Acknowledgements

First of all, I want to express my deep thanks to my esteemed supervisor, Prof. Takeshi Naemura, for his guidance throughout my PhD study. I especially appreciate his efforts of helping me became an independent researcher. Without him, I would not have been able to make as much progress as I have achieved in my research.

I would also like to express my appreciation to my committe members: Prof. Emeritus. Katsushi Ikeuchi, Prof. Kiyoharu Aizawa, Prof. Yoichi Sato, Prof. Shin'ichi Satoh, Assoc. Prof. Toshihiko Yamasaki and Assoc. Prof. Yasuyuki Ozeki for their insightful advices that helped me complete my dissertation.

I would like to thank my staffs in Naemura Laboratory, Dr. Rei Kawakami, Dr. Shogo Fukushima and Dr. Naoya Koizumi for their appropriate comments and feedback.

I would like to appreciate the members of Naemura Laboratory. Especially, I would like to thank Dr. Ryo Nakashima for giving me useful comments when I wrote manuscripts and prepared presentations for papers or articles. Leijie Shu and Ryota Yoshihashi helped my algorithm implementation with their hardware knowledge and program skills. Also, thanks to Mikyoung Seo, Dr. Hanyuool Kim, Dr. Youngah Sung and Junghyun Kim for their encouragement and support. Yuri Tsuchida helps administrative works for focusing my research.

A good support system is important to surviving and staying sane in graduate school. I was lucky to be a member of Naemura laboratory. All the members of Naemura laboratory have been kind and help me adjust to laboratory life. It was an wonderful experience for me to share research ideas and to be motivated in our laboratory.

I would like to express my special appreciation to the MEXT program that provided me with the opportunity to gain wider breadth of experience. I also thank

to the Information Science and Technology (IST) staffs with their efforts to make optimal research conditions.

I also want to express my appreciation to the members of robot technology team in Samsung Elec. For their supporting, I could focus on my dissertation with company business.

Last but not the least, I would like to thank my lovely family: father, mother and brother for their endless love and care. They are always extremely supportive when I was struggling. I love them so much, and I would not have made it this far without them. I would particularly like to thank my partner, Seonghyun Shin, for his remarkable patience and moral support, and for being with me during all my ups and downs.

2015/12/02

Boyoung Kim

"Sincerity is the way to Heaven"

Mencius

Contents

List of Tables

List of Figures

Chapter 1

Introduction

1.1 Background

The invention of the microscope enables the exploration of microcosm, which has revealed the secrets of nature. Particularly, in biology and medicine, the microscope has found numerous discoveries that could not be obtained through our eyes. Among the various types of microscopy, with modern microscopes, wide-field fluorescence microscopy (WFM, commonly fluorescence microscopy means wide-field fluorescence microscopy) has been one of the most major tools because of its high contrast, high specificity and high ability of tracking. Emission of fluorescence light is brighter than reflection of light, and this property allows fluorescent micrographs to have high contrast. Colorizing biological structures of interests by different dyes shows high specificity[3]. Moreover, WFM enables users to track activities of dyed region over time because the fluorescence remains for many days or weeks.

Such WFM has been developed to observe 3D cellular structures by generating a series of discrete 2D image planes that are referred to optical sectioning. Fig. 1.1 shows the acquisition of 3D WFM image. The 3D WFM is widely used now.

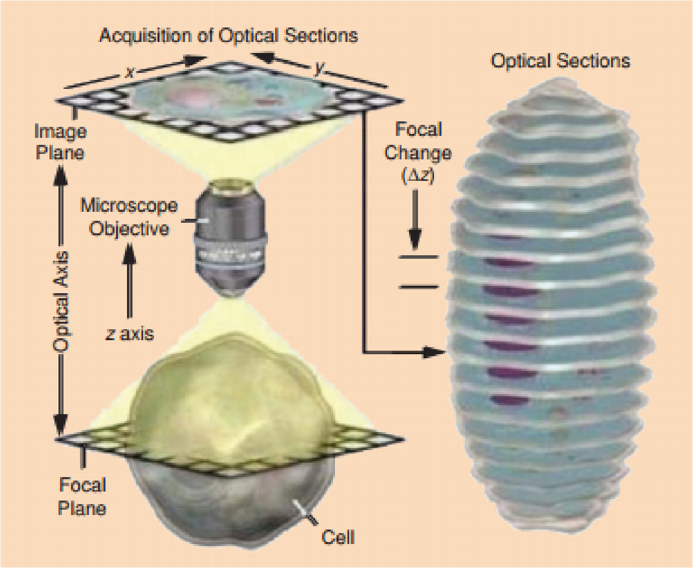

Figure 1.1: Acquisition of 3D microscopy image[1]

However, it has several issues, such as out-of-focus blur obscuring the entire in-focus detail and thereby reducing the contrast of the in-focus object[1]. Two major approaches to overcome these problems have been devised. The first approach is to apply new microscopy optics. Confocal microscopy, the most widely used approach, suppresses out-of-focus blur by means of a pinhole. It, however, has two limitations, namely, slow image acquisition and photobleaching[8]. The second approach is to apply image restoration by a deconvolution algorithm. It enhances the resolution and contrast of blurred WFM images without the limitations affecting the first approach. Therefore, I mainly focus on the second approach.

1.2 Contribution

A goal of this dissertation is an accurate estimation of the object image from the observation image. General imaging model for deconvolution is shown as Fig. 1.2, where $\otimes$ represents the sum of multiples between a point spread function (PSF) and an object. The object image that we want to retrieve is a discrete image of the

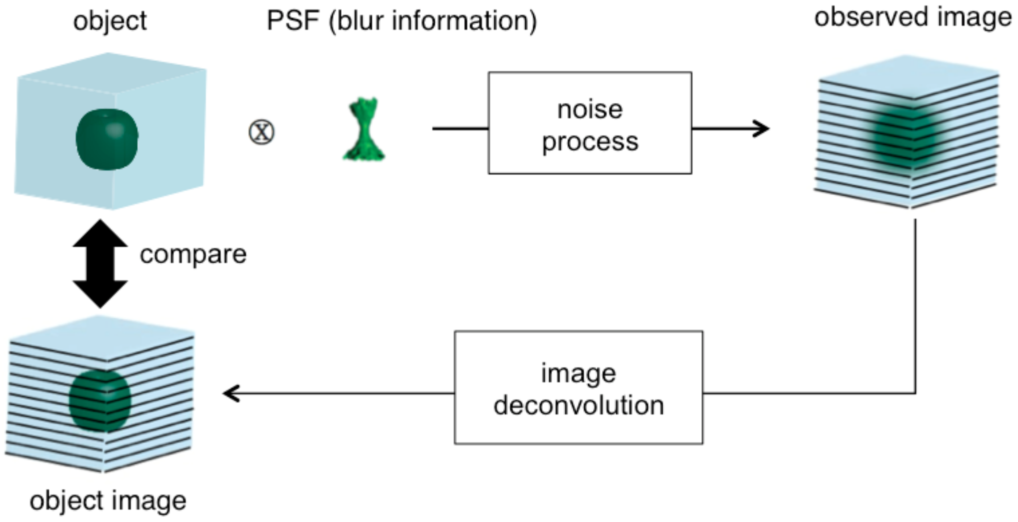

Figure 1.2: Imaging model for deconvolution

object, which is blurred by a PSF. Photons of the blurry object arrive in CCD camera following certain noise process. For achieving the goal, a practical deconvolution algorithm and an accurate PSF are necessary.

Despite the progress of deconvolution algorithms for WFM, however, it is still a big challenge to satisfy noise robustness and the convergence of an objective function. A guarantee of convergence of the objective function considering noise prevents local minimum, thereby leads to accurate image deconvolution results. On the other hand, as higher performance is needed, required computational cost is higher. Such computational cost for users has not been handled as far as I know. This thesis calls these issues as a practical deconvolution and handled it.

Even if the deconvolution process is perfect, without accurate PSF, the goal cannot be achieved. Since 3D WFM has unique imaging condition, it has distinct PSF characteristics from general camera model - depth-variant, specimen-dependent and asymmetric properties. Reflecting these properties determine the accuracy of PSF. Therefore, this thesis focuses on improving accuracy of PSF estimation.

Following subsections illustrates main contributions for the accurate object image estimation.

1.2.1 Practical Deconvolution

This subsection illustrates three contributions that are considered in WFM image deconvolution.

Appropriate Noise Model

WFM only takes photons that are emitted from the dyed molecules in the dark background. This means that taken photons are few. A probability that photons arrive at CCD camera can be expressed by Poisson distribution. In case of many photons, the imaging model can be approximated by Gaussian distribution. This is a reason that a typical imaging model shows Gaussian distribution. However, in case of WFM, the approximation cannot be applied due to a small quantity of photons. Also, since photons are few, effect of noise is huge, relatively. Therefore, deconvolution for WFM has to consider such effect of noise.

Guarantee Convergence

An Error on PSF and a noisy image are inevitable as shown in Fig. 1.2. Generally, for the estimation of object image, iterative image deconvolution methods are mainly used because non-iterative image deconvolution methods are sensitive to the error[1]. The iterative methods restore the object image by maximizing objective function based on statistics model. In this time, if the iterative methods cannot accurately update the object image after iteration, inaccurate object image is estimated as iteration is executed. Therefore, a guarantee convergence of objective function is directly connected to an accurate image deconvolution, which links to the accurate object image estimation.

Implementation on a PC

An expectation of computational cost and performance can help users to select algorithms to meet their requirements. Imaging model that has higher dimensions can express actual imaging well and thereby the deconvolution using the model shows higher performance. However, higher computational cost is also required. Therefore, there is a trade-off between accuracy and computational cost. Required time and memory according to an image size, data type and imaging model can show the highest performance imaging model with a single PC at present.

1.2.2 Improving Accuracy of PSF Estimation

To improve accuracy of PSF estimation, the PSF model has to reflect its characteristics. The author focused following characteristics.

Depth-variant PSF

The blur varies according to depth. WFM is designed to be suitable to the refractive index of immersion layer. However, the refractive index of specimen layer is different from immersion layer, which causes spherical aberration. Therefore, as the optical system focuses on a deeper specimen, the blur becomes severer, which leads to the axial elongation of observation. Previous depth-invariant algorithms could not suppress the elongation since their PSF is only appropriate to a single depth plane.

Specimen-dependent PSF

Generally PSF is unknown and the observed image is only given. There are trials to PSF pre-measurement in previous works [6, 9]. The PSF pre-measurement is executed by an observation of point-like object. They assumed that the pre-measured PSF has same imaging condition. However, the pre-measurement is inadequate due to the specimen dependence. The refractive index and the focal distance are changed when the point-like object for PSF pre-measurement is switched into the specimen to be recorded. Therefore, the actual PSF is specimen-dependent; rather the PSF estimation from the observed image which is called by blind deconvolution is more accurate and suitable.

Asymmetric PSF

The aforementioned two properties came from the gap between actual and designed imaging conditions. However, even if the actual imaging condition is ideal, the blur has a unique asymmetric shape due to imperfection of lens. The lens imperfection brings out various aberrations such as coma and astigmatism, consequently, which occurs a complex asymmetric PSF shape. Ignoring the asymmetry, the deconvolution result would be asymmetric and inaccurate.

As shown in Fig. 1.2, performance of the deconvolution algorithm is evaluated by comparing between the estimated object image and the object. Fig. 1.3 summarizes the goal and contributions on this dissertation.

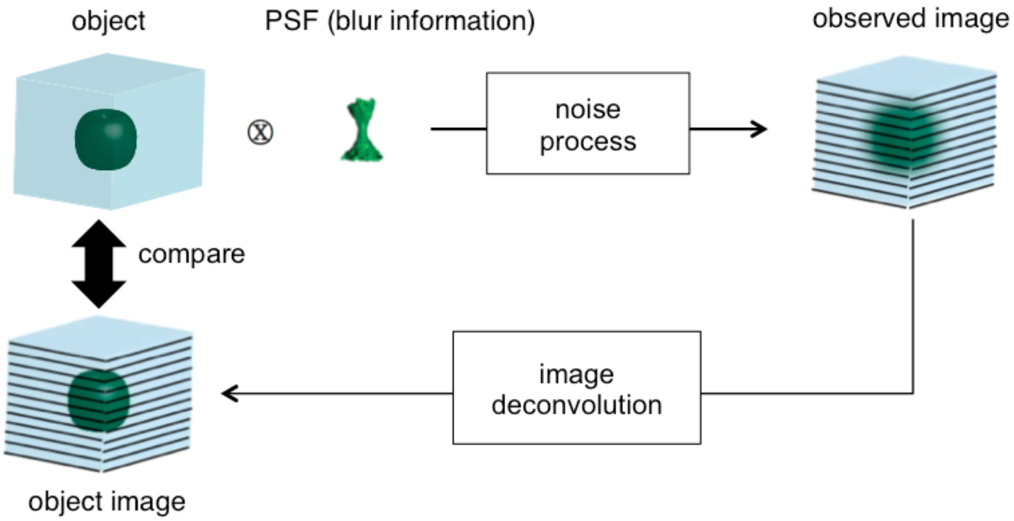

- **Goal: accurate estimation of object image**
- **Contribution**
  - Practical image deconvolution
    - Appropriate noise model
    - Guarantee convergence
    - Implementation on a PC
  - Improving accuracy of PSF estimation
    - Depth-variant PSF
    - Specimen-dependent PSF (Blind estimation)
    - Asymmetric PSF

Figure 1.3: Goal and contributions on this dissertation

1.3 Thesis Overview

This thesis is constructed as the following.

Chapter 1. Introduction

Chapter 2. Related Works

Chapter 3. Depth-variant Deconvolution

Chapter 4. Blind Deconvolution using Depth-variant PSF

Chapter 5. Blind Deconvolution using Depth-variant Asymmetric PSF

Chapter 6. Conclusion

In Chapter 2, previous work related to this dissertation will be reviewed. First, WFM concept compared with other fluorescence microscopy will be introduced for easier understanding the following contents. Next, from general imaging model to the one for WFM will be illustrated as a fundamental study of the main discussion. Computational cost according to imaging model is covered here. Existing PSF estimation methods and image deconvolution algorithms will also be handled and the criteria (limitations) to be considered will be clarified. With the clarifying, in order to apply distinct PSF properties in estimation, reasons of the properties will be illustrated. The handled PSF estimation and image deconvolution algorithms are utilized in proposal sections in Chapter 3, 4, and 5. Finally, the dissertation classifies existing studies based on the criteria and compared with the proposed algorithms.

In the following Chapter 3, 4, and 5, the details of proposed algorithms for accurate image deconvolution will be introduced. Proposed practical image deconvolution that is built in Chapter 3 is applied also in Chapter 4 and 5. From Chapter 3, 4, and 5 can be divided by adding PSF properties depth-variance, specimen-dependence, and xyz asymmetry.

In Chapter 3, depth-variant deconvolution, which provides practical image deconvolution for thick specimen, will be proposed. In this deconvolution, generalized expectation-maximization (GEM) algorithm is first introduced to WFM. GEM algorithm is known as noise robustness and the guarantee convergence. However, the GEM algorithm have been used for CT, MRI images but not appeared in WFM. Using the GEM algorithm, the accurate estimation of the object image is implemented. Also, the deconvolution algorithm proposes the estimation of depth-variant parametric PSFs from the pre-measured PSF, which can generate noise-free depth-variant PSFs. Using the generated PSF, the GEM deconvolution algorithm is implemented on a PC. For evaluation, normalized correlation between a true object image and the estimated object image will be used. Evaluation results will be compared with existing algorithms and depth-invariant version.

In Chapter 4, blind deconvolution using depth-variant PSF, which enables to remove the remained blur in Chapter 3, will be proposed. In the deconvolution, PSF is estimated from the observed image (blind deconvolution) and thereby reflects actual imaging conditions. From the analysis of intensities of the observed image, PSF for centre of the object is initially generated. Then, an optimization of a statistical model estimates depth-variant PSFs from the observed image. The estimated PSF from the observation image removes the remained blur, and the effect will be illustrated. Experiments are implemented using open data in order to compare other commercial software and algorithm. Since true image of the open data is unknown, pre-information (diameter and shape) of the taken object will be evaluation indicators.

In Chapter 5, blind deconvolution using depth-variant asymmetric PSF, which corrects distortions as well as removes blurs, will be proposed. In the deconvolution, estimated PSF includes lens distortions, which enables to estimate asymmetric PSF. Parameters of the distortions are simplified to prevent over-fitting. PSFs and the object image are estimated from the observation image as same as Chapter 4. For the symmetry evaluation, degree of symmetry is measured from the deconvolution result of the symmetric object. Standard deviation of diameters and relative contrast at each axis will be evaluation indicator. Finally, this Chapter summarizes the performance and computational cost according to deconvolution algorithms.

In Chapter 6, the discussion on deconvolution for 3D WFM, the contributions of this dissertation, will be concluded and possible future works are summarized with finishing the dissertation.

The entire structure of this dissertaion is illustrated in Fig.1.4.

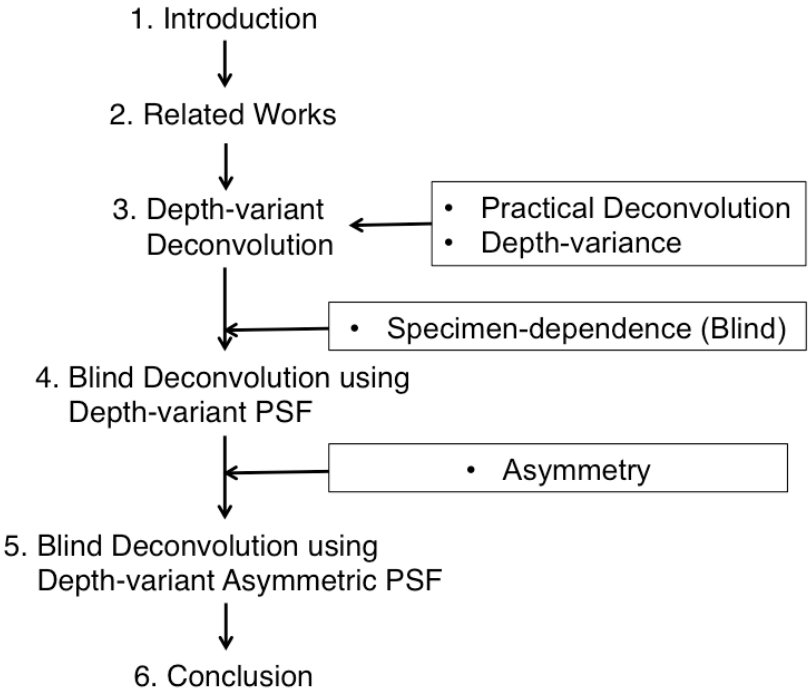

Figure 1.4: Overview of this dissertation

Chapter 2

Related Works

In this chapter, fluorescence microscopy concept and coordinates in the field of microscopy will be introduced. After exploring imaging models for deconvolution, the author makes a brief survey of previous studies on deconvolution algorithms and PSF estimations for WFM. The review will show the limitations in terms of practical deconvolution and improving accuracy of PSF. Also, distinctions of our works will be shown. Finally, previously proposed studies that are used in our proposed methods will be addressed.

2.1 3D Wide-field Fluorescence Microscopy

2.1.1 Concept

The principle of fluorescence microscopy is to detect an emitted light that the specimen illuminates. The emitted light is generated by shooting a light of a specific wavelength to the specimen. The sample is labeled with fluorescent stains or fluorescent protein and it becomes itself the light source[2]. This is concept of a conventional fluorescence microscopy, which is called wide-field fluorescence microscopy (WFM). WFM has three merits as follows.

high contrast: An emission of fluorescent is brighter than reflection of light

high specificity: Colorization biological structures of desired by multiple fluorescence labeling

high ability of tracking : Once stained, it remains for many days or weeks.

These merits show the reason that the WFM have been a key role in cell biology. Fig.2.1 shows the high specificity of the WFM. With these merits, WFM is utilized to genome analysis, protein expression, an observation of cell division and so on. Furthermore, 3D micrograph technique was developed to investigate a 3D structure of the specimen, which is called optical sectioning microscopy. The 3D wide-field micrograph is obtained by piling up a series of discrete 2D image planes. Moving along an axial axis (z axis), the 2D images are captured [10]. Image acquisition process for 3D WFM is represented by Fig. 2.2. However, 3D WFM is faced with a limit in optical resolution. Even if lenses has perfect alignment and no defects, diffraction causes out-of-focus blur and restricts the resolution [11]. This thesis focuses on the limitation.

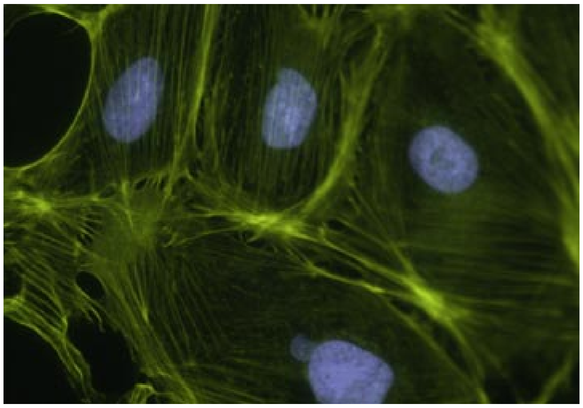

Figure 2.1: Fluorescence double-labeling of mammalian cells by Petra Bjrk. The DNA in the cell nuclei are shown in blue. Microfilament are shown in green.[2]

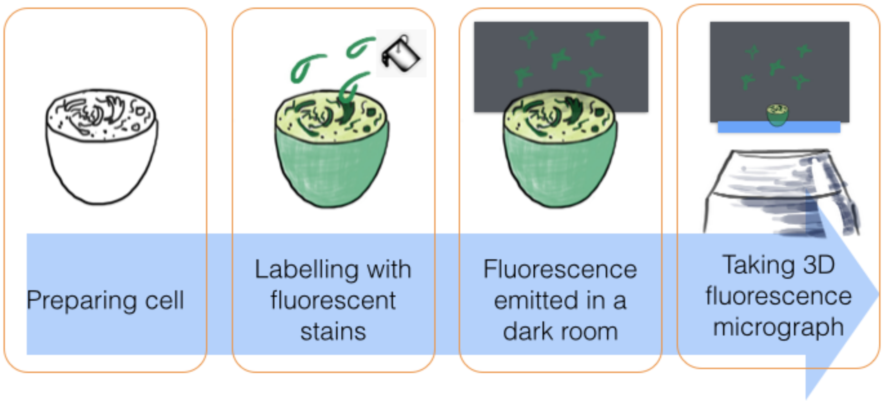

Figure 2.2: Image acquisition process for 3D WFM

2.1.2 Confocal Microscopy versus Deconvolution of Wide-field Microscopy

To overcome the limit of resolution, two major approaches have been conducted. Fig.2.3 shows a schematic of confocal and wide-field microscopy.

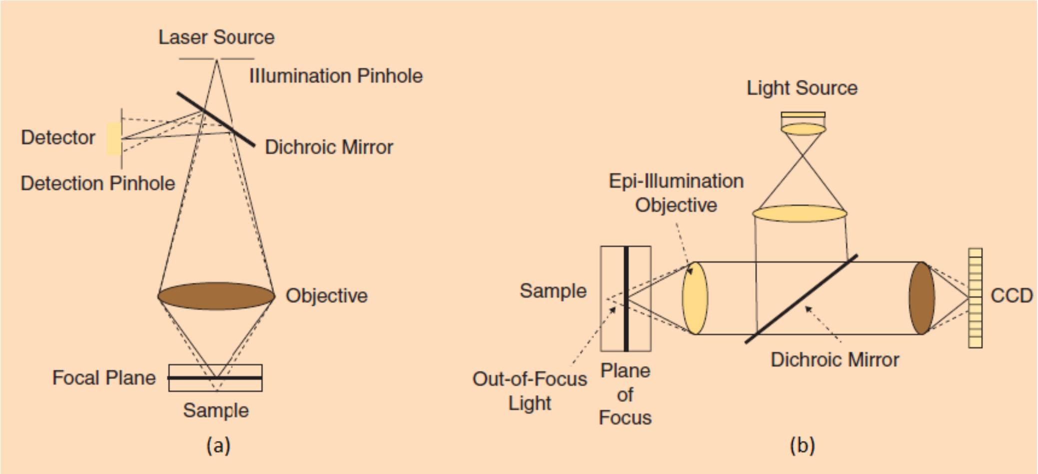

Figure 2.3: Schematic of (a) confocal and (b) wide-field microscopy[1]

Confocal microscopy

The first approach is to apply new microscopy optics. Confocal microscopy, the most widely used approach, suppresses out-of-focus blur by means of a pinhole. As shown in Fig.2.3(a), out-of-focus lights expressed as dotted line are blocked at pinhole. The pinhole plays the role of cutting off most of out-of-focus intensities. However, confocal microscopy cannot remove out-of-focus blur perfectly because the pinhole size is restricted due to reducing the effect of noise. Besides, the amount of light from the pinhole is limited, which causes problems such as slow image acquisition and photobleaching[10]. In order to acquire images pixel by pixel or line by line, the image acquisition of confocal microscopy is slow. Also the light concentration by the pinhole bleaches the dye as shown in Fig.2.4 and causes cell damage.

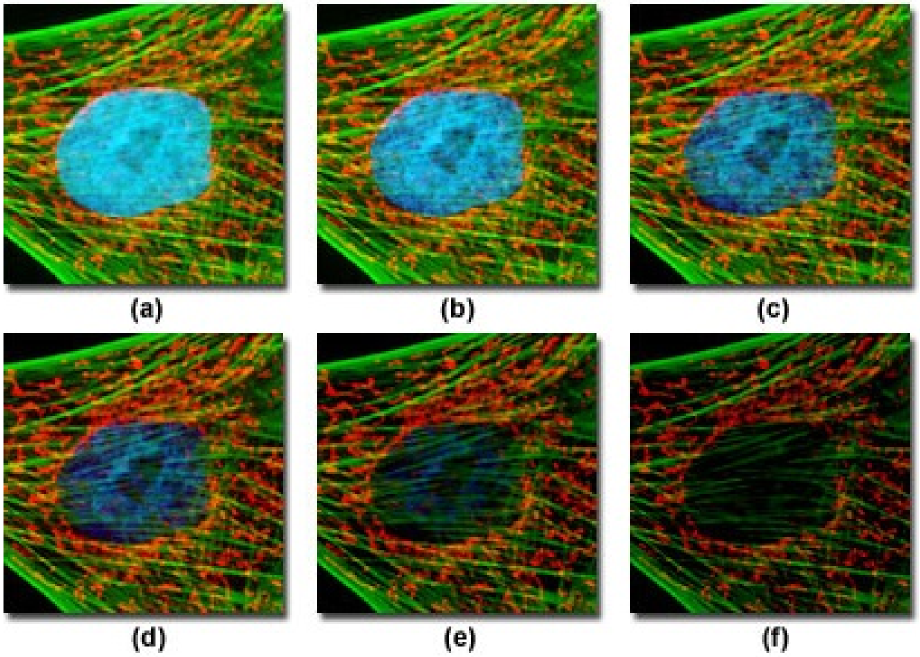

Figure 2.4: Example of photobleaching observed in a series of images captured at different time points for a multiply-stained culture of Indian Muntjac deer epidermis fibroblast cells[3]

Deconvolution of wide-field microscopy

In case of WFM, since the light concentration is weaker than confocal microscopy, problems such as slow image acquisition and photobleaching do not exist. In addition, purchase cost is reasonable. However, out-of-focus blurs come into CCD camera

Table 2.1: Wide-field microscopy compared to confocal microscopy

	No photo-bleaching	Image quality	Acquisition time	Price
Confocal	X	clear	slow	about \$200,000
WFM	O	blurry	fast	about \$35,000

as shown in Fig.2.3(b). The out-of-focus blurs make the observation image blurry. Table.2.1 depicts comparison between confocal microscopy and wide-field microscopy.

A single problem of the WFM is a blurry image observation. This dissertation proposes the deconvolution algorithm of WFM in order to obtain clear observation image with no photobleaching, fast acquisition time and reasonable price.

2.2 Fundamentals on Imaging Model

For ilustrating specifics of previous works and proposals, this section define coordinates and imaging models according to PSF characteristics.

2.2.1 Axes Definition

Prior to introducing related studies, the author introduces axes orientations and coordinates to avoid confusion. Axes definition is shown in Fig. 2.5. The microscopy coordinate system is orthogonal. The optical axis, defined as z axis, is an imaginary line that passes through the center of the objective lens. The x axis and y axis represent row and column of 2D images to be at 90 degree from the z axis and at 90 degree from each other. The origin is located right above the microscope stage and passes the optical axis. Direction from the origin to specimen is regarded as positive direction for z axis. The opposite direction becomes negative direction for z axis. This thesis uses z coordinate with depth. The deep depth means that the z coordinate is far from the origin along positive direction of z axis.

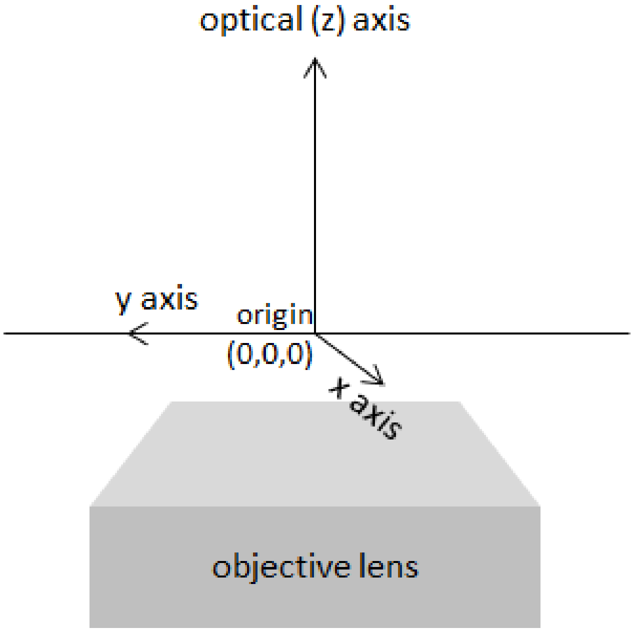

Figure 2.5: Axis definition in microscopy system

Subsequently, coordinates in object and image space are introduced. An object position $\boldsymbol{p}_o = \{x_o, y_o, z_o\}$ is defined by a position in the object image. An image position $\boldsymbol{p}_i = \{x_i, y_i, z_i\}$ is defined by a position in the observed image. In case of fixed depth, radial positions can be used. An object radial position and an image radial position can be expressed as $\boldsymbol{r}_o$ and $\boldsymbol{r}_i$, respectively. A PSF becomes a mapping function between object and image position. The blurry object can be generated between the object image and PSF. Then, photons of the blurry object arrive in CCD camera. Since the emission of photons is random, a probability of the arriving can be modeled by a Poisson noise model[1]. This thesis defines object, observed image and PSF as f, g and h, respectively. Then the coordinates of imaging model can be expressed as shown in Fig.2.6 Based on the definition, the thesis derives imaging models.

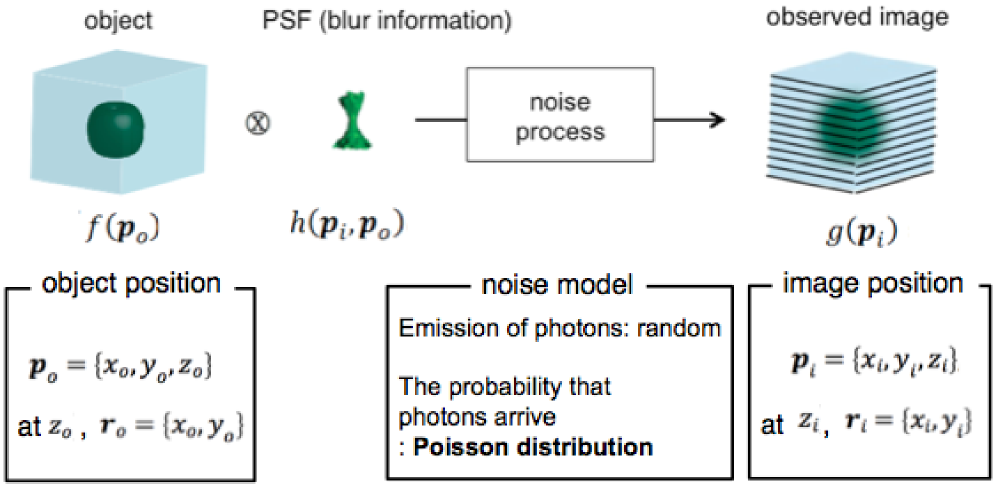

Figure 2.6: Coordinates of imaging model

2.2.2 Imaging Model Without Noise

Without noise process, the observation 3D image, g, could be modeled by the following integral of multiples between a PSF $h_{F(6)}$ and object f that we want to retrieve:

$$\begin{aligned} g(\boldsymbol{p}_i) &= \int f(\boldsymbol{p}_o) h_{F(6)}(\boldsymbol{p}_i, \boldsymbol{p}_o) d\boldsymbol{p}_o \\ \text{where} & \begin{cases} h_{F(6)}(\boldsymbol{p}_i, \boldsymbol{p}_o) \geq 0 \\ \int h_{F(6)}(\boldsymbol{p}_i, \boldsymbol{p}_o) d\boldsymbol{p}_i = 1 \text{ for } \forall\, \boldsymbol{p}_o \end{cases} \end{aligned} \tag{2.1}$$

where the PSF $h_{F(6)}$ has six dimensions $(x_i, y_i, z_i, x_o, y_o, z_o)$. In Eq.(2.1), the first condition for PSF makes image intensities greater than or equal to zero. The second condition for PSF manages to maintain a constant sum of intensities. The aim is to estimate the object f from the observation image g. As shown in Eq. (2.1), in order to estimate the object f given the observation image g, a PSF estimation has to be preceded. The WFM deconvolution method in the beginning assumed space-invariance and symmetry for the sake of simplicity.

The space-invariance reduces dimensions of PSF. Since a space-invariant PSF model does not depend on object space, the PSF model $h_{F(6)}(\boldsymbol{p}_i, \boldsymbol{p}_o)$ can be transformed as $h_{SI(3)}(\boldsymbol{p}_i) \overset{\text{def}}{=} h_{F(6)}(\boldsymbol{p}_i, 0)$. The PSF $h_{SI(3)}$ represents 3D (x_i, y_i, z_i) and space-invariant PSF. Then the image model in Eq.(2.1) can be simplified like as:

$$g(\boldsymbol{p}_i) = \int f(\boldsymbol{p}_o) h_{SI(3)}(\boldsymbol{p}_i - \boldsymbol{p}_o) d\boldsymbol{p}_o = \left(f * h_{SI(3)}\right)(\boldsymbol{p}_i) \tag{2.2}$$

where $*$ denotes a convolution operator. The PSF symmetry assumption further simplifies the image equation. To have point symmetry, the coordinates must be equidistant from the origin, and the PSF is converted as: $h_{SIS(1)}\left(|\mathbf{p}_i - \mathbf{p}_o|\right)$. $h_{SIS(1)}$, where $h_{SIS(1)}$ denotes a space-invariant, symmetric and 1D PSF. Then the image equation Eq.(2.2) is converted as follows:

$$\begin{aligned} g(\boldsymbol{p}_i) &= \int f(\boldsymbol{p}_o) h_{SIS(1)}\left(|\mathbf{p}_i - \mathbf{p}_o|\right) d\boldsymbol{p}_o \\ &= \left(f * h_{SIS(1)}\right)(\boldsymbol{p}_i) \end{aligned} \tag{2.3}$$

As depicted in Eq.(2.3), 6D PSF in Eq.(2.1) is converted to 1D PSF. However, the PSF in Eq.(2.3) does not reflect that photons in WFM pass specimen layer. WFM lens is designed to focus the specimen plane right above a microscopy stage with the refractive index of immersion layer as blue line in Fig.2.7(a). If the refractive index of specimen n_s is same with one of immersion layer, the optical path passes the designed path like as the red dotted line in Fig.2.7(b). In practice, the mismatch between the refractive indices of the immersion layer n_i and specimen layer n_s causes axially asymmetric blur, which is depicted as red line in Fig.2.7(b). The axial asymmetry separates axial coordinates and radial coordinates in PSF so that they have different spread. Since the radial symmetry is still remained, the PSF model in Eq.(2.3) can be converted like as: $h_{SIRS(2)}\left(|\mathbf{r}_i - \mathbf{r}_o|, z_i\right)$ where $h_{SIRS(2)}$ indicates a space-invariant, radially symmetric and 2D PSF. The image model in Eq.(2.3) is transformed as

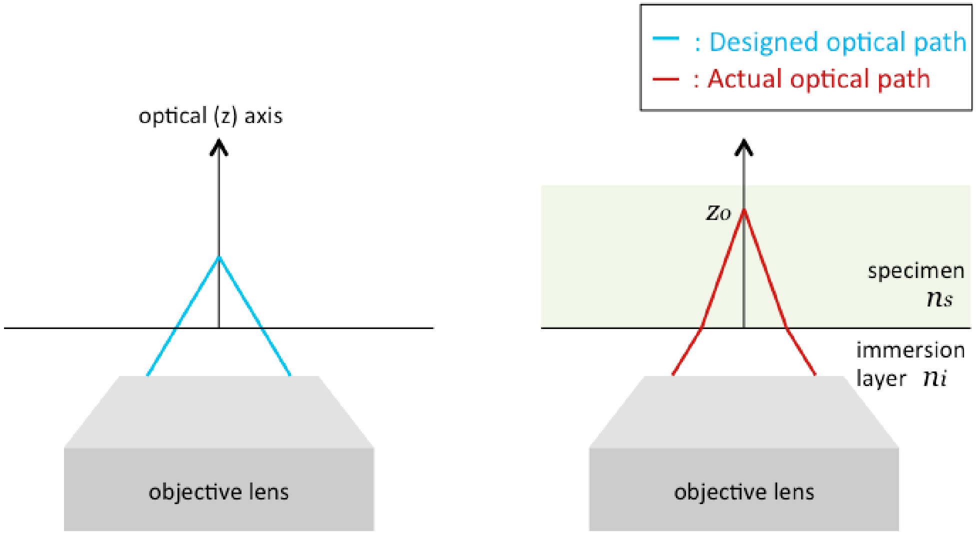

(a) no specimen assumption
(no specimen)
$n_i = n_s$

(b) actual observation
(with specimen)
$n_i = n_s$

Figure 2.7: Designed optical path and actual optical path

follows:

$$\begin{aligned} g(\boldsymbol{p}_i) &= \int f(\boldsymbol{p}_o) h_{SIRS(2)} \left(\left| \mathbf{r}_i - \mathbf{r}_o \right|, z_i - z_o \right) d\boldsymbol{p}_o \\ &= \left(f * h_{SIRS(2)} \right) (\boldsymbol{p}_i) \end{aligned} \tag{2.4}$$

However, for thick specimens, the image model is not that simple as Eq.(2.4). It is noticeable that as WFM focuses deeper inside in a specimen (the depth z_o has a bigger value), the mismatch increases. This phenomenon causes depth-variance of PSF (dependence of depth z_o). Then the PSF is converted to $h_{DVRS(3)} \left(\left| \mathbf{r}_i - \mathbf{r}_o \right|, z_i, z_o \right)$ where $h_{DVRS(3)}$ denotes depth-variant, radially symmetric and 3D PSF. The image model that reflects the depth-variance is as follows:

$$g(\boldsymbol{p}_i) = \int f(\boldsymbol{p}_o) h_{DVRS(3)} \left(\left| \mathbf{r}_i - \mathbf{r}_o \right|, z_i - z_o, z_o \right) d\boldsymbol{p}_o \tag{2.5}$$

Table 2.2: Summary of PSF models

			z (depth)		
			invariant		variant
			symmetric	asymmetric	
xy	variant	asymmetric	-	-	$h_{F(6)}$
	invariant		-	$h_{SI(3)}$	$h_{DV(4)}$
		symmetric	$h_{SIS(1)}$	$h_{SIRS(2)}$	$h_{DVRS(3)}$

In terms of axial axis, PSF in Eq.(2.5) includes not only the difference between the coordinates in image space and object space but also the axial location in object space, which makes PSF in Eq.(2.5) depth-variant. On the other hand, PSF in Eq.(2.4) does not include the axial location in object space. Since it is known that the radial symmetry is marginal [1], most existing work[12, 13, 14, 15, 16, 17, 18, 19, 20] assumed radial symmetry. Proposed deconvolutions in Chapter 3 and 4 also use this imaging model. If the radial asymmetry is not ignored, the PSF is like as: $h_{DV(4)}(\boldsymbol{p}_i - \boldsymbol{p}_o, z_o)$, where $h_{DV(4)}$ indicates the depth-variant, asymmetric and 4D PSF. The following equation expresses the image model using the converted PSF:

$$g(\boldsymbol{p}_i) = \int f(\boldsymbol{p}_o) h_{DV(4)} \left(\boldsymbol{p}_i - \boldsymbol{p}_o, z_o\right) d\boldsymbol{p}_o \tag{2.6}$$

The proposed deconvolution in Chapter 5 utilizes this imaging model for nonnegligible radial asymmetry of PSF.

The image model for WFM deconvolution has been developed by adding PSF characteristics - axial asymmetry, depth-variance, radial asymmetry. The progress is expressed as equations from Eq.(2.3) to Eq.(2.6). Each PSF models according to characteristics are summarized in Table.2.2. It is noticeable that dimensions of PSF increases and the image model gets close to $h_{F(6)}$ as PSF expresses its shape freely without restriction. The high dimensional PSF model requires expensive computational cost, but at the same time, it well expresses actual PSF shape and restores the object more accurately.

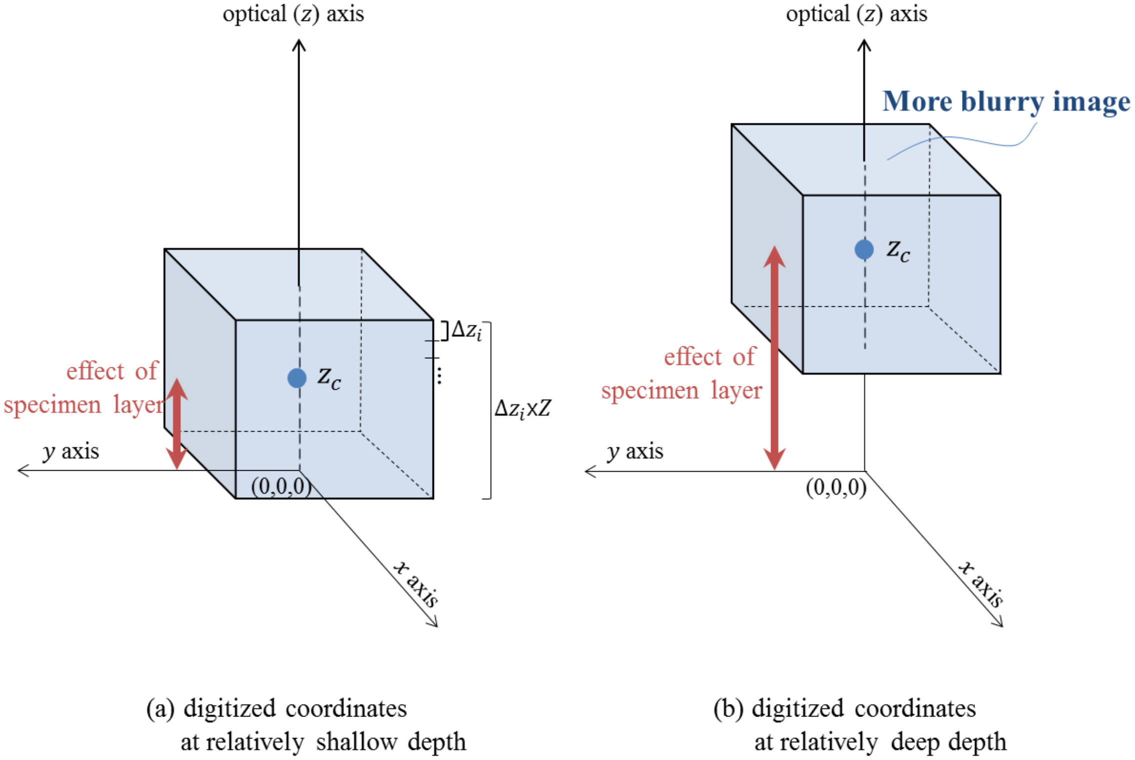

Figure 2.8: Digitized coordinates at relatively shallow and deep depth

2.2.3 Digitized Imaging Model

So far, coordinates of the image model have been continuous. Hereafter, image models are depicted as discrete, because the observed images were digitized and the estimated object cannot be continous. In other words, the image models have been illustrated theoretically, but hereafter, the image models include both theory and illustration for implementation.

When an image is digitized, its intensity is known only on a discrete grid. Therefore, the smallest we can obtain is one voxel and the intervals of the continuous coordinates can be approximated as one voxels. The size of a single voxel is the same for an observed image, object and PSF.

Since the object that must be retrieved has a finite image size, the coordinates of the digitized image have a finite range, in contrast to those in the continuous model.

Also, the estimated object becomes an object image because the estmated one has discrete coordinates. The digitized coordinates are depicted in Fig. 2.8. The finite space is divided by X, Y and Z voxels, which are the numbers of observed image voxels along the x-, y- and z-axes, respectively. Also, z_c is defined as the centre point of the area of interest of the object along the z-axis. Then, the digitized object location can be represented like as:

$$\boldsymbol{p}_o = (x_o, y_o, z_o) : |x_o| \leq \frac{X-1}{2}\Delta x_o, |y_o| \leq \frac{Y-1}{2}\Delta y_o, |z_o - z_c| \leq \frac{Z-1}{2}\Delta z_o \qquad (2.7)$$

Where Δx_o, Δy_o and Δz_o represents one voxel size in object space along each axis. The finite coordinates are represented by a blue box in Fig. 2.8. The reason that the position of the centre of the object z_c is included in the range of the digitized z-axis is as follows. A PSF in the depth-variant image model is determined by an object position z_o that is a distance from the origin (0,0,0) along the z-axis. Therefore, we determined the range of the digitized z-axis according to allocated pixels based on the point z_c. In general, the interesting part is located in the specimen layer, which can be characterized by the condition $z_c \geq 0$. While images taken at shallow depths are less affected by refractive index of the specimen layer as depicted in Fig. 2.8(a), those taken at greater depths are significantly affected as depicted in Fig. 2.8(b). The digitized observation image is given by

$$\boldsymbol{p}_i = (x_i, y_i, z_i) : |x_i| \leq \frac{X-1}{2}\Delta x_i, |y_i| \leq \frac{Y-1}{2}\Delta y_i, |z_i - z_c| \leq \frac{Z-1}{2}\Delta z_i \qquad (2.8)$$

For easier understanding of the digitized image model, we define the current depth of object as follows:

$$z_n = z_c + \left(n - \frac{Z-1}{2}\right)\Delta z_o \qquad (2.9)$$

The depth-variant PSF $h_{DV(4)}$ in Eq.(2.6) is converted to h_n and the subscript n of PSF represents the fixed depth of the object. In the same manner as the continuous model in Eq. (2.1), sum of PSF equals to one.

$$\sum_{\boldsymbol{p}_i} h_n\left(\boldsymbol{p}_i\right) = 1 \text{ for } \forall\, n \tag{2.10}$$

Also, we rewrite the object image $f(\boldsymbol{p}_o)$ as the $f_n(\boldsymbol{p}_o)$ to match the converted PSF as follows:

$$f_n(\boldsymbol{p}_o) = \begin{cases} f(\boldsymbol{p}_o) & \text{where } z_n = z_o \\ 0 & \text{where } z_n \neq z_o \end{cases} \tag{2.11}$$

Namely, the Eq.(2.11) represents each x-y slice in 3D zero matrix. And the object image satisfies following condition: $\sum_{n=0}^{Z-1} f_n(\boldsymbol{p}_o) = f(\boldsymbol{p}_o)$. Blurred image for each slice of object image can be obtained by 3D space-invariant convolution.

$$g_n\left(\boldsymbol{p}_i\right) = f_n\left(\boldsymbol{p}_o\right) * h_n\left(\boldsymbol{p}_i\right) \tag{2.12}$$

Now, the image model in Eq.(2.6) can be converted to a digitized image model as follows:

$$g\left(\boldsymbol{p}_i\right) = \sum_{n=0}^{Z-1} g_n\left(\boldsymbol{p}_i\right) \tag{2.13}$$

In this dissertation, the digitized image model in Eq. (2.13) is employed. Fig.2.9 (b) represents the calculation of the depth-variant model. The calculation of the shift-invariant image model is depicted in Fig.2.9 (a). While image models using shift-invariant PSFs such as $h_{SIS(1)}$, $h_{SIRS(2)}$ and $h_{SI(3)}$ can be calculated as a single convolution operation, the depth-variant image model requires as many convolution operations as the number of z stacks Z.

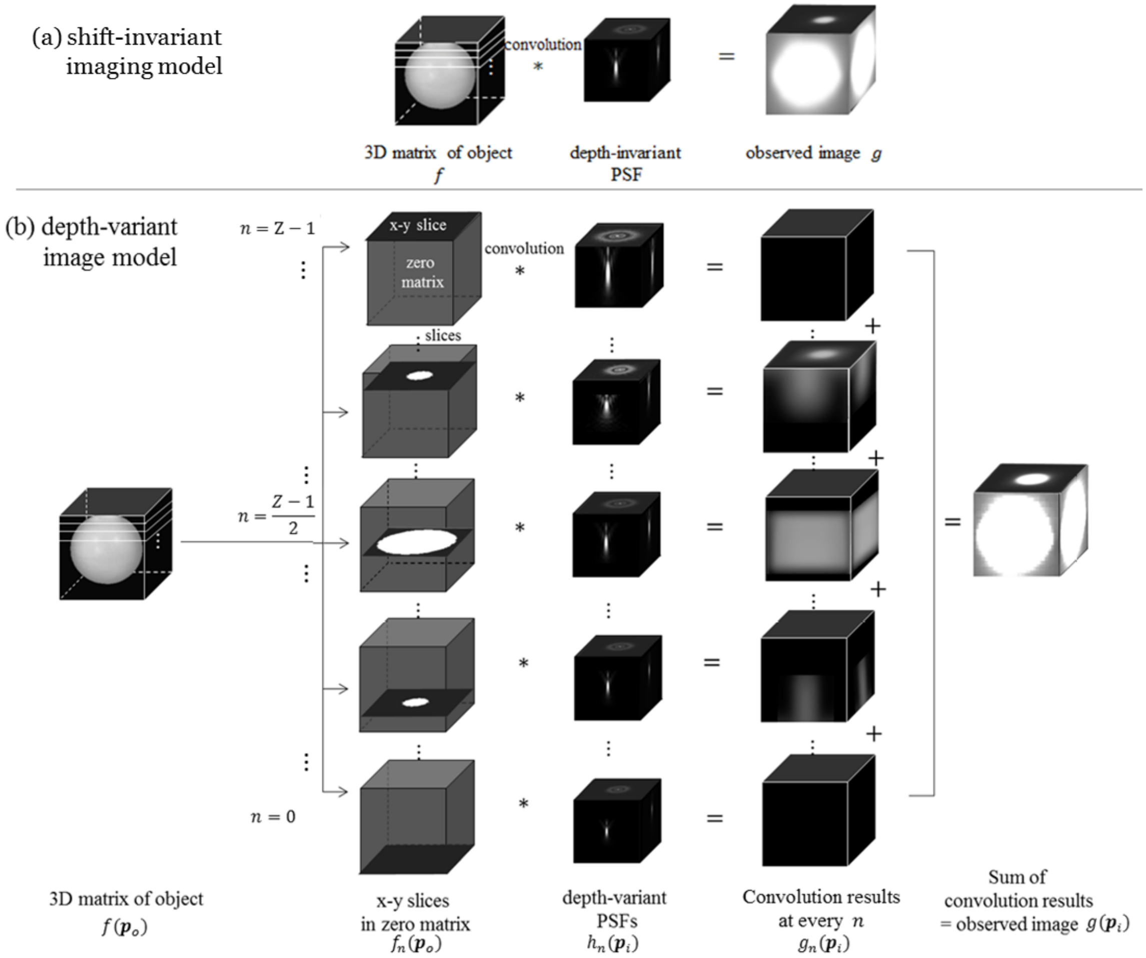

Figure 2.9: Shift-invariant imaging model and depth-variant imaging model (a) space-invariant image model : single 3D convolution between object image and depth-invariant PSF (b) depth-variant image model: sum of convolution results at every x-y planes

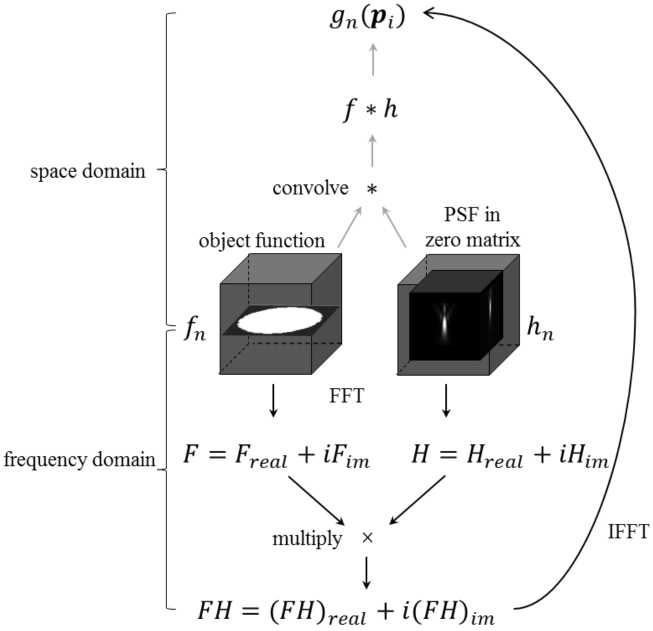

Figure 2.10: Convolution using fast Fourier transform

Convolution operation is calculated by a multiple of signals in the frequency domain for calculation speed. The calculation of a convolution operation is depicted in Fig. 2.10. A single convolution operation requires two fast Fourier transform (space to frequency domain), one multiplication and one inverse fast Fourier transform (frequency to space domain).

$$g\left(\boldsymbol{p}_i\right) = \sum_{n=0}^{Z-1} \mathrm{IFFT}\left(F_n H_n\right) \tag{2.14}$$

Where F_n and H_n denote the object image f_n and PSF h_n in frequency domain, respectively. As denoted in Eq.(2.14), the observed image is obtained by sum of inverse fast Fourier transform of $(F_n H_n)$. When PSF is loaded, even if PSF size is smaller than image size, PSF size is expanded to observed image size in order to multiple in frequency domain. Namely, the PSF voxels are placed in the center of an array of all zeros and utilize this array to calculate multiple in frequency domain, which is depicted in Fig. 2.10.

Depth-variant deconvolution requires the same number of convolution operations as of z stacks, resulting in high computational cost, as depicted in Fig. 2.9. This may be a reason why most existing methods have not proposed it. At present, a regular desktop PC can run programs with high memory requirements that could not be executed in the past.

2.2.4 Summary of Existing Studies according to Imaging Model

In the previous subsection, we examined various imaging models. The dimension of the imaging model is variant to PSF characteristics. There are important PSF characteristics shown below.

- ***Depth-variance***
- ***Specimen-dependent PSF (blind deconvolution)***
- ***Asymmetry***

The PSF varies according to locations of image and object, which represents the depth-variant PSF characteristic. This characteristic is because a spherical aberration of WFM is caused by refractive indices mismatch between the immersion medium and the specimen. As the optical system focuses on a deeper specimen, the spherical aberration increases. This aberration phenomenon is the mechanism of the depth-variant characteristics for 3D WFM.

Even if the PSF is measured previously, imaging condition between the PSF pre-measurement and the actual imaging is different. In the procedure of switching the point-like object for pre-measurement into the specimen, the focal distance and the refractive index vary. This thesis calls the variance according to specimen by specimen-dependence. To solve this problem, the PSF has to be estimated from the observed image. Unlike the general methods, in Chapter 4 and 5, blind deconvolution is used for the accuracy not for user convenience.

Also, even if the specimen and imaging conditions are ideal, the PSF of WFM has an asymmetric shape due to an imperfection of the lens. In case of a parametric PSF that are used in existing studies, it is modeled by a symmetric PSF along x-y axis. Because PSF asymmetry along z axis is relatively severer than along x-y axis, they ignore the asymmetry along x-y axis. One study used a non-parametric PSF[6], which has a risk to estimate an inaccurate PSF that loses its diffraction and aberration pattern by noise.

These three characteristics cover all possible major causes of blurs in WFM imaging condition and optical system design. Based on introduced three PSF characteristics, the author classified previous studies and proposals, which is depicted in Table.2.3. This thesis considers the asymmetry term in Table.2.3 to be satisfied when the PSF is radially (x-y axis) as well as axially (z axis) asymmetric. The third row in Table.2.3 shows deconvolution methods according to the PSF characteristics of depth-variance and asymmetry. The reflection of PSF characteristics is an important key of a deconvolution performance. As shown in Table.2.3, Depth-variant deconvolution appeared in the 2000s. Because the depth-variant deconvolution became

Table 2.3: Summary of existing studies on WFM deconvolution

Depth-variant		✓		✓
Asymmetric			✓	✓
PSF model	$h_{SIRS(2)}$	$h_{DVRS(3)}$	$h_{SI(3)}$	$h_{DV(4)}$
Non-blind (specimen -independent)	JOSA A92a[12] Sig. Proc93[13] SPIE96[14]	JOSA A04[15] SPIE10[16] Maalouf 10[17] **Chapter 3**	JOSA A93[21] Science95[22]	JOSA A07[6]
Blind (specimen -dependent)	JOSA A92b[18] JOSA A99[19] SPIE13[20]	**Chapter 4**	Applied Opt95[23] PAMI10[24] ISBI12[25]	**Chapter 5**

available on a PC as the development of a PC. Specifics between computational cost and imaging model are addressed in Chapter 5. The proposed method in Chapter 3 uses the known PSF that is depth-variant radially symmetric, as existing studies used[15, 16, 17]. Chapter 3 proposes a practical deconvolution using the PSF model, which will be addressed in next section. On the other hand, proposed methods in Chapter 4 and 5 utilize PSF models that are not used in existing methods. As shown in Table.2.3, deconvolution methods in Chapter 4 and 5 estimates the object image accurately by improving PSF accuracy. The proposed method in Chapter 5 includes all significant characteristics depth-variance, specimen-dependence and asymmetry.

As for evaluation, the mean square error (MSE) or the normalized correlation coefficient (COR) is used as performance indicators in general. These indicators only can be utilized when the true image is known (non-blind approaches). Chapter 3 also utilizes the normalized correlation coefficient for evaluation. On the other hand, blind approaches do not have the true image. Therefore, they evaluate performance with actual image of micro-bead that has determined shape and diameter[25, 26]. The micro-bead has a determined diameter and a hollow sphere shape. Therefore, the diameter and the relative contrast between shell and hollow inside are used for performance indicators. Since proposed algorithms in Chapter 4 and 5 are also blind approach, the author also used these indicators.

2.3 Image Deconvolution

From this section, the author considers the noise process. The noise process in imaging model follows a Poisson model, since photons illuminated from specimen arrive in the lens and consequently create a random number of light photons[1]. Among many deconvolution algorithm methods under Poisson noise model, the author chose generalized expectation-maximization (GEM) algorithm, which estimates the ideal image accurately by guaranteeing noise robustness and convergence. The GEM algorithm has not appeared in WFM before the author proposed it. Every existing deconvolution methods under Poisson noise model with regularization term approximate differentiation of intensities at a present iteration as at a previous iteration, which is not correct. This section introduces schemes of them in the following subsections. Also, the author theoretically proves that the GEM is more accurate method than the deconvolution using approximated regularization term.

2.3.1 Image Deconvolution under Poisson Noise Model

An estimated observed image λ in this subsection is defined by sum of multiples between the determined PSF h and the object image f. From λ definition, the operator $\otimes$ is defined as follows.

$$\lambda = \sum_{\boldsymbol{p}_o} f\left(\boldsymbol{p}_o\right) h\left(\boldsymbol{p}_i, \boldsymbol{p}_o\right) \overset{\text{def}}{=} f \otimes h \tag{2.15}$$

The observed image in this subsection is renamed by k.

$$k = g\left(\boldsymbol{p}_i\right) \tag{2.16}$$

Then, the objective function is easily derived. Under Poisson noise assumption, the objective function can be expressed as:

$$p\left(g|f,h\right) = \prod_{\boldsymbol{p}_i} \frac{\lambda^k e^{(-\lambda)}}{k!} \tag{2.17}$$

The objective function is the conditional probability - the observation probability given the true object image and the PSF. General image deconvolution under Poisson noise model maximizes the objective function in Eq.(2.17).

2.3.2 Richardson Lucy Algorithm

Richardson Lucy (RL) algorithm is a deconvolution method that maximizes the objective function in Eq.(2.17), iteratively. Since RL algorithm is most widely used in WFM deconvolution, the author introduces the concept and the specific.

To estimate the ideal image that maximize Eq. (2.17), a derivative of Eq. (2.17) should be found. Since the direct derivative of Eq. (2.17) is difficult, the objective function is replaced with the negative log-likelihood function that is obtained by a negative logarithm of the objective function:

$$\begin{aligned} J_{data}(f) &= \sum_{\boldsymbol{p}_i} (\lambda - k\log(\lambda) + \log(k!)) \\ &= \sum_{\boldsymbol{p}_i} (f \otimes h - g\log(f \otimes h) + \log(g!)) \end{aligned} \tag{2.18}$$

For the non-trivial task of the negative log-likelihood functional, RL algorithm estimates the object image using the principle of an optimization transfer[27]. The optimization transfer principle converts the minimization problem of a negative log-likelihood function J_{data} to the minimization problem of the surrogate functions $\Phi(f; f^s)$, where f^s is the estimated object image f at the sth iteration. It is verified that the sequence of the minimizers of the surrogate functions converges to the minimizer of the negative log-likelihood function, supposing that the surrogate function satisfies the following conditions[27]:

$$\begin{aligned} \Phi(f; f^s) &\geq J_{data}(f) \\ \Phi(f^s; f^s) &= J_{data}(f^s) \end{aligned} \tag{2.19}$$

To design a surrogate function for the Poisson likelihood function given the sth estimated image $f^s = [f^s(1), f^s(2), ...]$, the author describes the following identity [27]:

$$\lambda = f \otimes h = \left(f^s \otimes \left(\frac{h}{f^s \otimes h}\right)\right)\left(\frac{f}{f^s}\left(f^s \otimes h\right)\right) \tag{2.20}$$

After taking the logarithm of Eq.(2.20), applying the convex inequality derives

$$-\mathrm{log}\lambda = -\mathrm{log}\left(f \otimes h\right) \leq \left(f^s \otimes \left(\frac{h}{f^s \otimes h}\right)\right) \mathrm{log}\left(\frac{f}{f^s}\left(f^s \otimes h\right)\right) \tag{2.21}$$

Combining negative log-likelihood in Eq.(2.18) with the inequality in Eq.(2.21) leads to the following surrogate function:

$$\Phi(f; f^s) = -\sum_{\boldsymbol{p}_i} f \otimes h + \sum_{\boldsymbol{p}_i} g\, f^s \otimes \frac{h}{f^s \otimes h} \mathrm{log}\left(\frac{f}{f^k} f^s \otimes h\right) \tag{2.22}$$

It is remarkable that the surrogate function in Eq.(2.22) satisfies the condition in Eq.(2.19). The minimization solution of the surrogate function can be yielded by the derivative with respect to f:

$$\frac{\partial \Phi(f; f^s)}{\partial f} = -\sum_{\boldsymbol{p}_i} h + \frac{f^s}{f} h \otimes \frac{g}{f^s \otimes h} \tag{2.23}$$

Then, the object image that satisfy the derivative with zero is derived in Eq.(2.24), which is called Richardson Lucy (RL) algorithm [28, 29]:

$$f^{s+1} = f^s \left(h \otimes \frac{g}{h \otimes \hat{f}^s}\right) \tag{2.24}$$

The PSF is normalized as $\sum_{\boldsymbol{p}_i} h = 1$. However, it often causes a noise amplification problem because of ill-posed problem. To prevent the ill-posed problem, the objective function should incorporate a regularization term that penalizes intensity variations.

2.3.3 One Step Late Algorithm

This part introduces image deconvolution using the approximated regularization function. WFM image usually has a low SNR, which leads to noise amplification deconvolution results. Therefore, deconvolution algorithm should penalize difference of intensities to suppress noises. Therefore, the cost function (negative objective function) is modified as follows:

$$J_{penalized}(f) = \Phi(f; f^s) + \gamma R(f) \tag{2.25}$$

where γ is the regularization parameter. $f(\boldsymbol{p}_o)$ that minimize Eq. (2.25) would be an ideal image.

$$R(f) = \sum \psi\left([Df]_n\right) \tag{2.26}$$

where $D = [d_{ij}]$ is a matrix used for determining the difference adjacent pixels. Generally total variation regularization is chosen as the regularization constraint. Total variation regularization preserves edges due to its linear penalty on difference between adjacent pixels, it can be defined by [30, 31]:

$$\psi(f) = \sqrt{f^2 + \epsilon^2} \tag{2.27}$$

where a small positive number ϵ is used for making the function differentiable. Minimizing the cost function in Eq.(2.25), the ideal image can be estimated as follows:

$$\begin{aligned} \hat{f} = \arg\min J_{penalized}(f) &= \frac{\partial J_{penalized}(f)}{\partial f} \\ &= \frac{\partial \Phi(f; f^s)}{\partial f} + \gamma \frac{\partial R(f)}{\partial f} \end{aligned} \tag{2.28}$$

However, the total variation penalty couples each pixel in the restoration with its adjacent neighbors in such a way that a direct derivative for minimizing the cost function is not possible[14]. As the means of solving this problem, one step late (OSL) algorithm approximates the difference between adjacent pixels as the difference between the value of a current pixel and the values of the neighboring pixels from the previous iteration [32, 25]. The final form using OSL can be determined as follows:

$$f^{s+1} = \left(h \otimes \frac{g}{h \otimes \hat{f}^s} \right) \frac{f^s}{1 - \gamma div(R(f^s))} \tag{2.29}$$

where *div* stands for the divergence. However, a restored image using the approximation is not accurate since this method does not converge to the solution monotonically.

2.3.4 Generalized Expectation-Maximization Algorithm

Although it is not possible to yield the minimizer of Eq. (2.25) directly in a pixel-wise iterative procedure, it is possible to determine the minimizer of Eq. (2.25) by a sub-iteration procedure. A non-separable quadratic surrogate function of the regularization term can be defined as [27]:

$$\psi\left([Df]_n\right) \leq q([Df]_n\,; [Df^{s,m}]_n) \tag{2.30}$$

where $f^{s,m}$ is the estimated image at the mth sub-iteration and q denotes a quadratic surrogate function. This can be done by designing a separable quadratic surrogate function of the regularization function. Using De Pierro's additivity trick, the quadratic surrogate function can be converted as follows [33, 34]:

$$\begin{aligned} q([Df]_n\,; [Df^{s,m}]_n) =& q\left(\sum_p \frac{|d_{np}|}{d_n} \left(\frac{d_{np}}{|d_n|} d_{np}\left(f - f^{s,m}\right) + [Df^{s,m}] \right) ; [Df^{s,m}] \right) \\ \leq& \sum_p \frac{|d_{np}|}{d_n} q\left(\frac{d_{np}}{|d_n|} d_{np}\left(f - f^{s,m}\right) + [Df^{s,m}]\,; [Df^{s,m}] \right) \end{aligned} \tag{2.31}$$

The quadratic function $q(t;q) = \psi(q) + \dot{\psi}(q)(t-q) + \frac{1}{2}\breve{c}(q)(t-q)^2$, with $\breve{c}$ that guarantees the first inequality. One may determine the optimal curvature $\breve{c}$ by following the Hubers method [35]. The inequality in Eq. (2.30) is due to a convex inequality, in which equality is completed if $f = f^{s,m}$. From Eq.(2.30)and Eq. (2.31), the surrogate function of the regularization function $R_s(f; f^{s,m})$ meets the following condition [27]:

$$R(f) \leq \sum_{n}\sum_{p} \frac{|d_{np}|}{d_n} q\left(\frac{d_{np}}{|d_n|} d_{np}\left(f - f^{s,m}\right) + \left[Df^{s,m}\right]; \left[Df^{s,m}\right]\right) = R_s\left(f^{s,m}\right) \quad (2.32)$$

Then, the surrogate function of the regularization function is designed as the additively separable function. The derivative of the surrogate function with respect to f can be derived as follows as [27]:

$$\frac{\partial R_s(f; f^{s,m})}{\partial f} = \left.\frac{\partial R(f)}{\partial f}\right|_{f=f^{s,m}} + (f - f^{s,m})\breve{c} \quad (2.33)$$

By using the surrogate function of Eq. (2.32), the minimizer $f^{s,m}$ can be yielded as follows:

$$f^{k,s+1} = \arg\min\left(\Phi(f; f^s)\right) + \gamma R_s\left(f; f^{s,m}\right) \quad (2.34)$$

Taking the derivative of the surrogated cost function in Eq. (2.34) and computing it to zero derives the following quadratic equation [27]:

$$0 = -\sum h + \frac{f^s}{f}\left[g \otimes \frac{h}{h \otimes f^s}\right] + \gamma\left(\left.\frac{\partial R(f)}{\partial f}\right|_{f=f^{s,m}} + \left(f - f^{s,m}\right)\breve{c}\right) \quad (2.35)$$

The solution of the quadratic equation in Eq. (2.35) can be derived analytically [27], which is expressed as follows:

$$f^{(s,m+1)} = \begin{cases} \frac{\sqrt{b^2\left(f^{(s,m)}\right) + \breve{c}a\left(f^{(s,m)}\right)} - b\left(f^{(s,m)}\right)}{\breve{c}}, & \text{when } a\left(f^{(s,m)}\right) < 0 \\ \frac{a\left(f^{(s,m)}\right)}{\sqrt{b^2\left(f^{(s,m)}\right) + \breve{c}a\left(f^{(s,m)}\right)} + b\left(f^{(s,m)}\right)} & \text{when } a\left(f^{(s,m)}\right) \geq 0 \end{cases} \quad (2.36)$$

where $\check{c}$ and m represent curvature and sub-iteration, respectively. $a\left(f^{(s,m)}\right)$ and $b\left(f^{(s,m)}\right)$ are defined as

$$\begin{aligned} a\left(f^{(s,m)}\right) &= f^{(s,m)}\left\{h \otimes \frac{g}{h \otimes f^{(s,m)}}\right\} \\ b\left(f^{(s,m)}\right) &= \frac{1}{2}\left(1+\gamma\frac{\partial R\left(f^{(s,m)}\right)}{\partial f} - \check{c}f^{(s,m)}\right) \end{aligned} \tag{2.37}$$

several iterations of the procedure would reach the minimum solution of the cost function defined in Eq. (2.25). I depicted the scheme of GEM algorithm in Fig. 2.11 In Fig. 2.11, the negative log-likelihood function, surrogate function, quadratic surrogate function and separable quadratic surrogate function are denoted as $J_{data} + \gamma R(f)$, $J_{penalized}(f) = \Phi(f; f^s) + \gamma R(f)$, $\Phi(f; f^s) + \gamma R_Q(f; f^{s,m})$ and $R_S(f; f^{s,m})$, respectively. This iterative technique guarantee the convergence of cost function, which was proven to be effective in medical image reconstruction problems [36, 33, 34]. However, GEM has a problem of slow converge speed toward the final result.

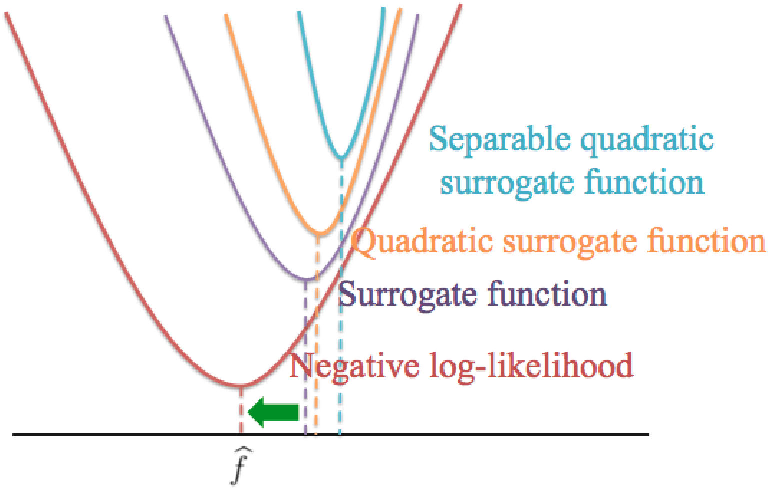

Figure 2.11: Concept of GEM algorithm

2.3.5 Summary of Existing Studies according to Deconvolution Algorithm

Practical image deconvolution for WFM should satisfy appropriate noise model and guarantee of convergence. Existing algorithms that are introduced are summarized in Table.2.4.

Table 2.4: Summary of existing studies according to deconvolution algorithm

		convergence	
		not guaranteed	guaranteed
noise	sensitive	-	RL algorithm [18, 23, 37, 38, 17, 24, 16]
	robust	OSL algorithm [5, 21]	GEM algorithm

Image deconvolution that satisfies both noise robustness and convergence has not been applied in WFM. For the practical image deconvolution, the authour first introduced the GEM algorithm to WFM and the proposal is described in Chapter 3.

2.3.6 Acceleration of Iterative Deconvolution

To accelerate the converge speed, the acceleration with GEM algorithm is used in Chapter 3 and 4. Iterative image deconvolution algorithms are nonlinear and provide more effective restoration than simple techniques such as linear inverse filtering. A chronic problem of iterative image deconvolution is slow convergence speed. To increase the speed of convergence, Biggs proposed an acceleration method using vector extrapolation [4]. The acceleration method predicts where each pixel in the image is going from the correction obtained by an each iteration. A new point c^s is predicted, and an existing iterative image restoration algorithm is applied to generate the next estimate f^{s+1} and gradient l^s as follows:

$$\begin{aligned} c^s &= f^s + \alpha^s \left(f^s - f^{s-1}\right) \\ &= f^s + \alpha^s \left(\varphi\left(f^{s-1}\right) - f^{s-1}\right) = f^s + \alpha^s l^{s-1} \\ f^{s-1} &= c^s + l^s = \varphi\left(f^s\right) \\ \alpha^{s+1} &= \frac{\left(l^s\right)^T l^{s-1}}{\left(l^{s-1}\right)^T l^{s-1}} \end{aligned} \tag{2.38}$$

Fig. 2.12 shows an illustration of the acceleration method. The vector extrapolation enables to accelerate iterative image deconvolution algorithms by predicting subsequent point using previous points.

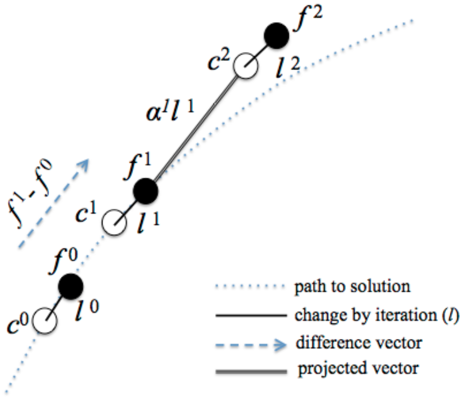

Figure 2.12: Illustration of the acceleration method.

In their experiments, RL deconvolution achieves an average speed up of 40 times after 250 iterations [4], which is depicted in Fig. 2.13.

The acceleration method shows considerable promise in accelerating other types of iterative image deconvolution.

Figure 2.13: Blurred and restored images using RL. (a) blurred, (b) unaccelerated RL (250 iteration), (c) accelerated RL (250 iteration), (d) unaccelerated RL (10000 iteration)[4]

2.4 PSF for WFM

In order to estimate an accurate object image f, an accurate PSF estimation have to be preceded. This section introduces three PSF models that are utilized in this dissertation. First PSF model is the experimental PSF, which is an observation of the point-like object. Second one is the most popular Gibson's parametric PSF, which is a depth-variant and radially symmetric PSF model. Last one is the Zernike polynomial parameterized PSF, which is a depth-variant and asymmetric PSF model. Chapter 3 proposes the estimation of parameters in Gibson's model to the experimental PSF. Chapter 4 proposes the estimation of parameters in the Gibson's PSF model from the observed image. Chapter 5 proposes the estimation of parameters in the Zernike polynomial PSF model from the observed image.

2.4.1 Experimental PSF

In experimental PSF approach, images of one or more point-like objects are recorded. The blur from the point-like object itself is regarded as PSF, which follows literally the meaning of PSF. A fluorescence micro-bead is typically used for the point-like object. The size of the micro-bead should be smaller than a resolution of WFM. The resolution of WFM is defined as follows [39]:

$$resolution = \frac{\lambda}{2\,\mathrm{NA}} \tag{2.39}$$

where λ and NA represent the wavelength of the emitted light and the numerical aperture.

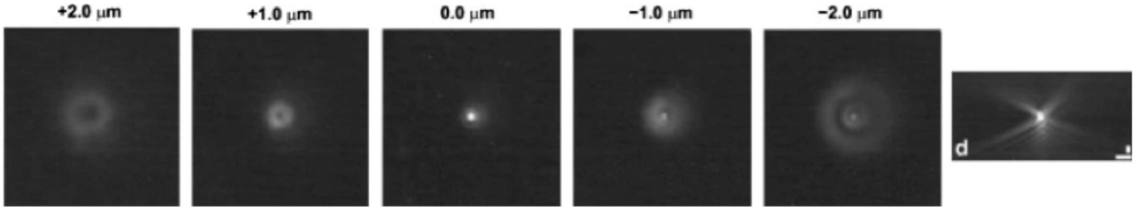

Figure 2.14: Sequential focal planes through experimentally determined PSF. Distances above and below focus are shown from +2.0 μm to -2.0 μm. [5]

3D experimental PSF is obtained by recording micro-bead images moving the focus, which is represented in Fig. 2.14. The experimental PSF images are also recorded moving along an axial axis in the same way with the specimen image recording. Recorded 3D image leaving the micro-bead at a certain position becomes the 3D PSF at one depth. However, it is necessary to obtain experimental PSFs at all depths since PSFs at several depths are different. To obtain depth-variant PSFs, there was a study to get experimental PSFs at several depths, which is depicted in Fig. 2.15 [6]. Experimental PSF has an advantage that the PSF reflects the actual experimental setup [5]. Therefore, the obtained PSF include all types of aberration symmetric and

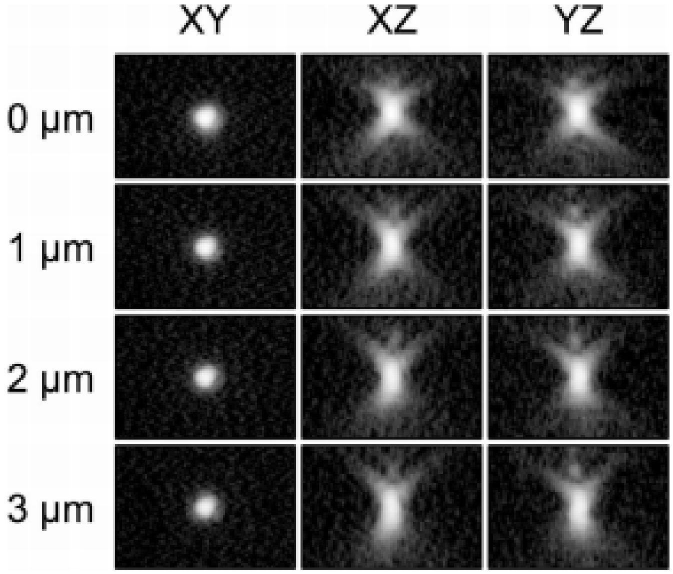

Figure 2.15: Depth-variant experimental PSFs [6]

asymmetric factors of PSF. However, making the same condition of the experimental PSF measurement as of the actual imaging is almost impossible; the object position and the refractive index of specimen can be changed. Besides, noises in the recorded experimental PSF is regarded as blur [1]. Since the micro-bead is smaller than the resolution of WFM, not surprisingly the recorded image has many noises compared to signal. Moreover, general biologists or medical scientists have a difficulty to making samples with micro-bead at certain multiple depths.

2.4.2 Parametric PSF: Gibson's Model

Theoretical parameterized PSF is calculated based on equations from the optical physics. The Gibson's model is based on Kirchhoffs integral formula. This model generates a 3D WFM PSF by substituting optical parameters. These parameters are refractive indices and optical distances (z coordinates in object and image space).

The Gibson's PSF model is given as [40]

$$h_{DVRS(3))}\left(\left|\boldsymbol{r}_i-\boldsymbol{r}_o\right|,z_i,z_o\right)=\left|\int_0^1 e^{ik_0\Lambda(z_i,z_o,\rho)}J_0\left(\left|\boldsymbol{r}_i-\boldsymbol{r}_o\right|k_0\mathrm{NA}\rho\right)\rho d\rho\right|^2 \tag{2.40}$$

where k_0 denotes the vacuum wave number, NA is the numerical aperture, and $\Lambda\left(z_i,z_o,\rho\right)$ represents the optical path difference (OPD) between the design and actual conditions. J_0 denotes the Bessel function of the first kind of the zero.

The depth-variance (axial shift-variance) is caused by the mismatch between object and immersion layer, which is the change of the PSF as a function of the position along the optical axis of the object plane [40]. An optical path of WFM is designed for specimens that are mounted immediately above the coverslip in a medium that is index matched to the immersion layer. In actual system, however, actual optical path does not pass as designed. Because a position that WFM focuses is different from the position immediately above the coverslip and refractive index of specimen is also different from the immersion layer. I depicted the designed and actual optical path in Fig. 2.16. The optical path difference (OPD) between designed and actual optical path causes spherical aberration, which makes asymmetric PSF along z axis. Fig. 2.17 shows Spherically aberrated PSF.

The bigger OPD makes more severe blur. In other words, taking the focus on a deeper layer in specimen (along z axis, as distance from origin increases) makes severe blur. The OPD equation that reflects the depth-variant characteristic is as follows:

$$\begin{aligned}&\Lambda\left(z_i,z_o,\rho\right)=\\&z_o\sqrt{{n_s}^2-\mathrm{NA}^2\rho^2}+t_g\sqrt{{n_g}^2-\mathrm{NA}^2\rho^2}-t_{g^*}\sqrt{{n_{g^*}}^2-\mathrm{NA}^2\rho^2}-t_{i^*}\sqrt{{n_{i^*}}^2-\mathrm{NA}^2\rho^2}\\&+\left(z_o-z_i+n_i\left(\frac{t_g}{n_g}-\frac{t_{g^*}}{n_{g^*}}-\frac{z_o}{n_s}+\frac{t_{i^*}}{n_{i^*}}\right)\sqrt{{n_i}^2-\mathrm{NA}^2\rho^2}\right)\end{aligned} \tag{2.41}$$

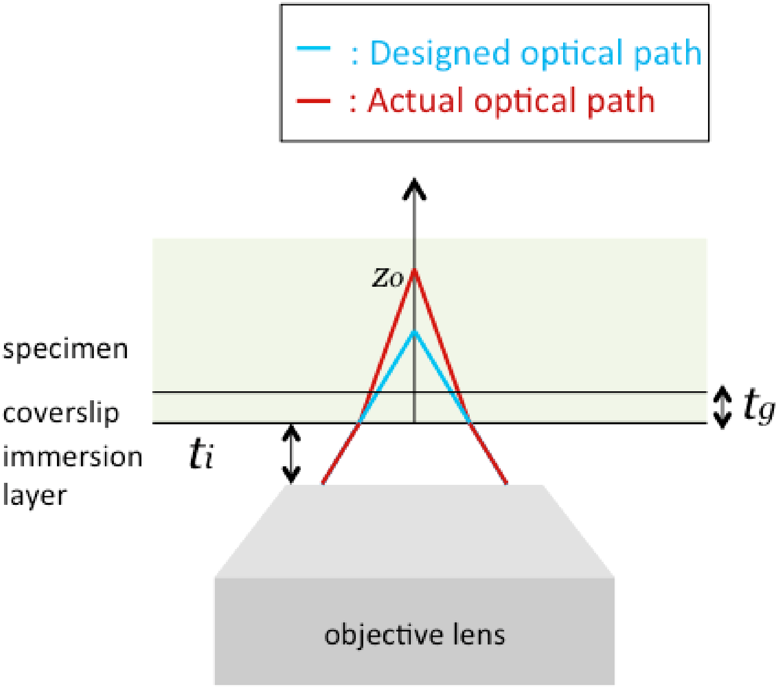

Figure 2.16: Optical path difference.

where n_g, n_s and n_i represent the actual refractive indices of the coverslip, specimen and immersion layer, while t_{g^*} and t_{i^*} are the design values for the thickness of coverslip and the immersion layer. n_{i^*} and t_g are actual refractive index of immersion layer and actual thickness of coverslip. From the Eq. (2.41), mismatch between designed and actual imaging condition causes the OPD.

In practice, a corrective ring on the objective exists to minimize the contribution of coverslip-induced aberrations, OPD is simplified and defined by [41]:

$$\Lambda\left(z_i, z_o, \rho\right) = z_o\sqrt{{n_s}^2 - \mathrm{NA}^2\rho^2} - t_{i^*}\sqrt{{n_{i^*}}^2 - \mathrm{NA}^2\rho^2} + \left(z_o - z_i + n_i\left(-\frac{z_o}{n_s} + \frac{t_{i^*}}{n_{i^*}}\right)\sqrt{{n_i}^2 - \mathrm{NA}^2\rho^2}\right) \tag{2.42}$$

From Eq. (2.40) (2.42), Gibson's PSF model has x-y symmetric and z asymmetric shape; Gibsons model covers only diffractions and spherical aberration. Since the

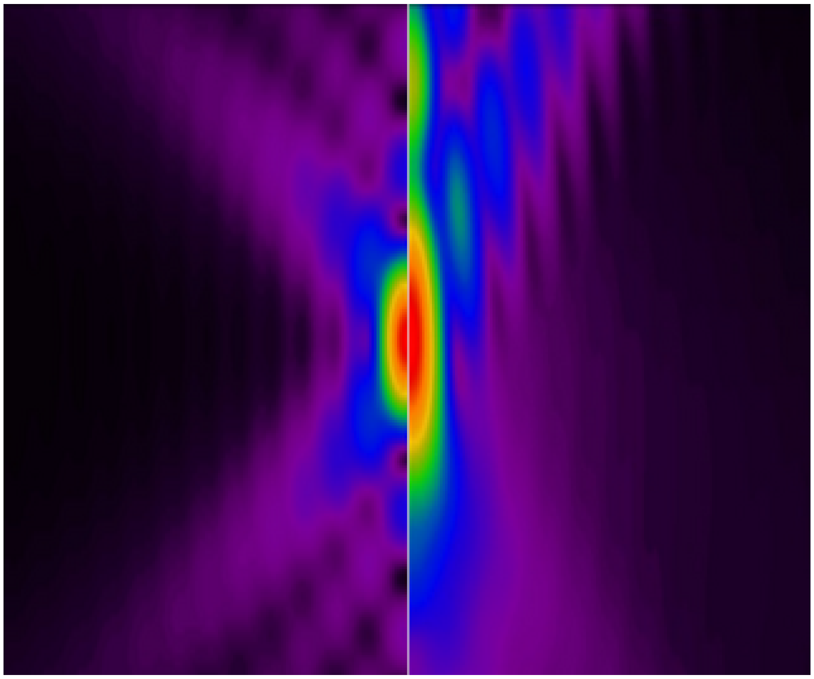

Figure 2.17: x-z slice through the focus distribution of a NA = 1.3 lens. Left: no spherical aberration; right: imaging into a medium with refractive index 1.4 at a depth of 10 micron [7]

PSF is obtained by the equation, there is no noise. Gibson's PSF model can generate depth-variant PSF at any depth by controlling z_o and z_i values. However, to generate depth-variant PSFs, obtaining parameters (n_i, n_s, z_o) that reflects actual imaging condition must be preceded. Besides, Gibson's model would be less accurate than a Zernike polynomial PSF model due to excluding x-y asymmetric factors such as coma, curvature of filed and astigmatism aberration.

2.4.3 Parametric PSF: Zernike Polynomial PSF Model

Zernike polynomial PSF model $h_{DV(4)}(\boldsymbol{p}_i, z_o)$ is a parametric PSF that include all aberrations, which is expressed as the multiple of magnitude of complex-valued amplitude PSFs at excitation and emission wavelength.

$$h_{DV(4)}(\boldsymbol{p}_i, z_o) = \left| \bar{h}(\boldsymbol{p}_i, z_o; \lambda = \lambda_{em})^2 \right| \tag{2.43}$$

where $\bar{h}(\boldsymbol{p}_i, z_o; \lambda = \lambda_{em})$ is complex-valued amplitude PSF at emission wavelength. The complex-valued amplitude PSF is the 3D Fourier transform of an amplitude optical transfer function that has values only on a spherical cap of radius n_i/λ limited by the aperture angle[42]. The complex-valued amplitude PSF is defined by[43]:

$$\begin{gathered}\bar{h}(\boldsymbol{p}_i, z_o; \lambda) = \\ \sum_{k_x}\sum_{k_y} p(k_x, k_y)\Lambda\left(k_x, k_y, z_o, n_i, n_s\right) e^{2i\pi z_i\sqrt{(n_i/\lambda)^2-(k_x+k_y)^2}} e^{2i\pi(k_x(x_i)+k_y(y_i))}\end{gathered} \tag{2.44}$$

where $\Lambda\left(k_x, k_y, z_o, n_i, n_s\right)$ indicates aberration function that the refractive index mismatch induces and it represents depth-variance of PSF[43]. λ represents wavelength. When the complex-valued amplitude PSF at emission wavelength is numerated, corresponding emission wavelengths ($\lambda = \lambda_{em}$) is used. The pupil fuction $p(k_x, k_y)$ in Eq. (2.44) can express lens imperfection. With perfect lens, the pupil function $p(k_x, k_y)$ has all ones in $\sqrt{k_x^2 + k_y^2} \leq n_i/\lambda$. However, actual lens has defects. Distorted pupil function have various values in $\sqrt{k_x^2 + k_y^2} \leq n_i/\lambda$ and it makes asymmetric PSF shape. Hanser's PSF model expresses the distorted pupil function as combination of modulus ω and phase ϕ functions as follows:

$$p(k_x, k_y) = \omega(k_x, k_y)e^{i2\pi\phi(k_x,k_y)} \tag{2.45}$$

Modulus and phase functions are expressed by Zernike polynomials [43].

$$\begin{aligned}\omega(k_x, k_y) &= \sum_n M_n Z_n(k_x, k_y) \\ \phi(k_x, k_y) &= \sum_n N_n Z_n(k_x, k_y)\end{aligned} \tag{2.46}$$

where Z_n represents Zernike polynomials. The pupil function of Hanser's model consists of 79 Zernike polynomials. The other part of Eq. (2.44) can be seen in the reference paper in detail[43].

The Zernike polynomial PSF model has every advantage of the Gibson's model - no noise, simple generation of depth-variant PSFs. The point that the Zernike polynomial PSF model is superior to Gibson's model is that the Zernike polynomial PSF model can express all type of aberration; Zernike polynomial PSF has an asymmetric shape along all directions. However, like as Gibson's model, it is difficult to obtain the modulus and phase parameters that reflect actual imaging condition.

2.4.4 Summary of PSF Estimation Methods

Table.2.5 compares existing PSF estimation methods.

Table 2.5: Comparison of WFM PSF Models

		Experimental PSF (noisy)	Parametric PSF	
			Gibson's PSF	Zernike polynomial PSF
PSF	Depth-variance		✓	✓
	Specimen-dependence			
	xyz Asymmetry	✓		✓

Existing PSF methods do not reflect specimen-dependence. From the most widely used Gibsons model, this thesis proposes new PSF estimation methods. Table.2.6 summarizes proposed method with utilizations of PSF models.

Table 2.6: Summary of proposed PSF estimation methods

		Chapter 3 (experimental PSF + Gibson's PSF)	**Chapter 4** (Gibsons PSF from observed image)	**Chapter 5** (Zernike PSF from observed image)
PSF	Depth-variance	✓	✓	✓
	Specimen-dependence		✓	✓
	xyz Asymmetry			✓

Chapter 3 (Proposal 1) proposes fitting the Gibson's theoretical PSF to the experimental PSF, which is applicable to real data when imaging condition of actual data is same as of experimental PSF. And it has advantages of simple PSF generation at any depths and no noise. Chapter 4 (Proposal 2) utilizes Gibson's theoretical PSF. Chapter 4 estimates optical parameters in Gibson's theoretical PSF from the observed actual image, which can be applicable to any real data. Chapter 5 (Proposal 3) utilizes Zernike polynomial theoretical PSF which is further accurate PSF model. Chapter 5 also can be applicable to any real data since parameters are estimated from the observed actual image.

2.5 Summary

In this chapter, 3D WFM concept and existing works are introduced to share the core goal with the readers of this thesis. The author has aimed to estimate accurate object image. The object image is estimated by deconvolution algorithm and PSF information. As a foundation of main discussion, imaging model according to PSF properties, deconvolution algorithms and existing PSF estimation methods have been reviewed. It is confirmed that photons of WFM image follow Poisson distribution and include many noise since arrived photons in CCD are few. Also, for accurate deconvolution, it is reviewed that convergence of iterative algorithm is significant. On the other hand, from the distinct characteristics of WFM, it is revealed that PSF has unique characteristics - depth-variance, specimen-dependence and asymmetry. It is reviewed that reflecting these characteristics is connected to PSF dimensions and computational cost.

The author divided criteria to two parts practical image deconvolution and improving PSF estimation. Practical image deconvolution includes criteria to be considered in deconvolution process. When deconvolution algorithm is implemented, appropriate noise model (noise considered imaging model under Poisson distribution), the convergence and implementation on a PC should be considered. The author unites these three criteria to one criteria called as practical image deconvolution. Improving PSF estimation part has three criteria (depth-variance, specimen-dependence and asymmetry) that are covered in PSF characteristics.

Table.2.7 shows the overview of the image deconvolutions which are proposed in this thesis. The main discussion starts from depth-variant deconvolution for practical deconvolution with 3D WFM. With introduction GEM algorithm to WFM image with depth-variant imaging model is proposed in Chapter 3. As removing blurs along optical axis from specimen-dependent PSF estimation, blind deconvolution using depth-variant deconvolution is proposed in Chapter 4. Finally, as correcting distortions from asymmetric PSF modeling, blind deconvolution using depth-variant asymmetric PSF is proposed in Chapter 5. Also, computational cost and performance according to deconvolution methods are summarized in Chapter 5.

Table 2.7: Research matrix of the deconvolution algorithms proposed in this thesis

		Chapter 3	**Chapter 4**	**Chapter 5**
Practical image deconvolution		✓	✓	✓
PSF	Depth-variance	✓	✓	✓
	Specimen-dependence		✓	✓
	xyz Asymmetry			✓

Chapter 3

Depth-variant Deconvolution

This chapter addresses the challenging problem on the practical image deconovlution. Specifically, the author aims to propose the deconvolution that guarantees convergence of objective function under the appropriate imaging model. Of course, the deconvolution should be implemented on a PC. The practical deconvolution provides accurate object image estimation result when a PSF is given.

However, existing deconvolution methods in WFM have not satisfied appropriate imaging model and convergence. the author proposes to use GEM algorithm as an image deconvolution. The GEM algorithm yields a pixelwise iteration that converges to the minimizer of the objective function that assumes a few photons.

The author also proposes a new PSF estimation methods that is applicable to actual image. The method estimates PSF by fitting a parameteric Gibson's model to a point-like object image. Then, depth-variant PSFs are generated shifting object and image coordinate along z axis. Since the PSF obtained by the proposed method involves the actual imaging condition from the point-like object image, which is appropriate for the actual image. While the experimental PSF has noise that confuses with blur, estimated PSF model has no noise because the PSF is generated by using mathematical formula.

A flowchart of the proposed method is depicted in Fig.3.1. From step A to step B show the proposed PSF estimation. From the estimated PSF, step C generates depth-variant PSFs by shifting depth parameters. Finally, in step D, introduced GEM algorithm is implemented using the generated PSFs.

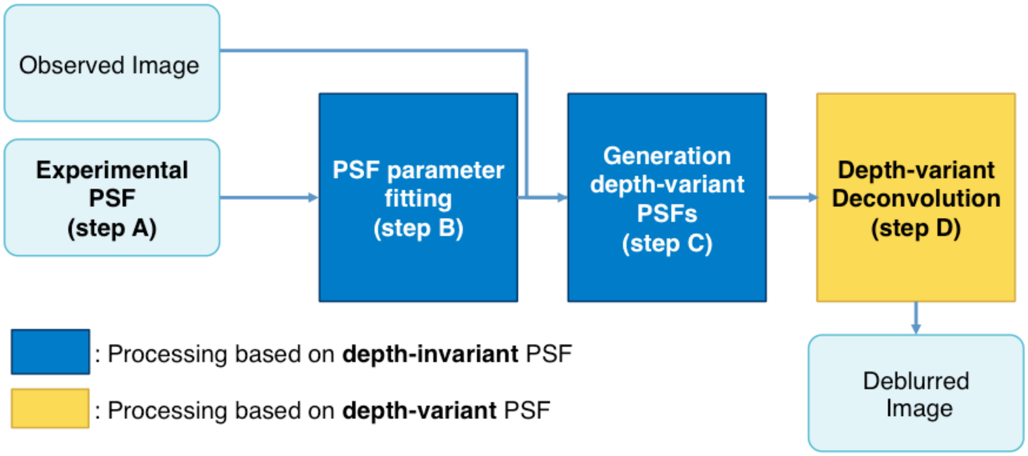

Figure 3.1: Flow chart of depth-variant deconvolution

This chapter verifies the effectiveness of the depth-variant GEM algorithm in comparison with classic methods such as the depth-invariant RL method, the depth-variant RL method, and the depth-invariant GEM method in simulations and experiments using microbeads. From this chapter, it is confirmed that the introduction of the GEM algorithm based on depth-variant imaging model can be practical deconvolution for WFM, which is the main contribution of this chapter.

3.1 Introduction

Despite depth variant charcteristic of PSF, many existing methods assume a depth-invariant PSF for simplicity and restored the observed image using well-developed shift-invariant deconvolution algorithm such as the RL algorithm [19, 14, 12, 44, 45]. Since the actual PSF is unknown, some methods obtain the PSF by using an image of point-like obejct and use the estimated PSF for deconvolution. Others try to estimate both the unknown PSF and the ideal image simultaneously through blind deconvolution approaches [19, 45]. However, the deconvolution results of such depth-invariant deconvolution algorithms are limited since the PSF used for the deconvolution does not reflect actual imaging condition. Besides, the PSF changes along the depth direction, which leads to unaccurate deconvolution results. To overcome these limitations, two studies proposed a depth-variant (DV) PSF estimation: experimentally obtained depth-variant PSF [6] and analytically computed PSF [15]. The former method requires placing the point-like object at each depth in micrometer unit, this is not easy for typical users. The latter method generate depth-variant PSFs based on a parametric Gibson's model [40]. However, this method is only applicable to actual images since the actual optical parameters cannot be known, therby the investigator tested only simulation images with known parameters. To my knowledge, there have been no studies on depth-variant deconvolution for practical observed images except for one recent study for confocal microscopy [46], probably due to the demanding expensive computations.

Because the intensity at each pixel in WFM follows a Poisson random variable [15, 44], most existing deconvolution methods for 3D WFM are based on the RL algorithm [28] that maximizes the Poisson likelihood function using the expectation maximization optimization approach. Even though the depth-variant RL method is more accurate than depth-invariant ones, its deconvolution result is still insufficient due to its noise sensitivity. Because the maximization of the likelihood function is ill-posed in the sense that the solution is not unique, deconvolution result of RL yields a noisy image [1, 27]. Therefore, one must incorporate a regularization function based on a priori information on the true image to yield a more enhanced image [14, 12, 44].

Regularized RL methods using a depth-variant PSF have been seldom studied except for recent two studies for confocal microscopy [47, 48]. On the contrary, there exist several studies on regularized depth-invariant deconvolution methods [14, 12, 44, 21, 49, 50]. The performance of depth-invariant methods is not satisfactory because the depth-variant PSF is only suitable to certain depth. In addition, the performance of many existing methods are limited since ineffective regularization functions were used. It is well known that the most useful a priori information is that of an ideal image with small intensity variations in the spatial domain, which requires a coupled regularization function defined by intensity differences in adjacent pixels. However, probably for simplicity, existing methods are based either on the intensity of each pixel (not the difference between pixels) or on approximations for computing differences between neighboring pixels [32, 47, 50]. I suppose that the scarcity of coupled regularization functions can be attributed to the belief that performing an RL-type pixelwise update is impossible for a coupled regularization function [14]. Although there are investigations based on the coupled roughness penalty function [48, 21], the methods require the simultaneous optimization of entire pixels, which is often computationally intractable. Existing regularized deconvolution methods with DV-PSF do not provide RL type iterative update algorithm to minimize negative Poisson likelihood plus regularization function.

3.2 Proposed Method

3.2.1 PSF Estimation

To estimate an accurate the image, two different techniques are investigated: experimental PSF and theoretical PSF. The experimental PSF treats the image of point-like object itself as a PSF. While the experimental has advantage of reflecting actual imaging condition, it regards recorded noise as blur also. Therefore, it is difficult to apply the experimental PSF to actual image deconvolution, directly. On the other hand, the theoretical PSF is analytically computed equation, which does not include any noise. However, it is also hard to apply the deconvolution for the actual image since optical parameters of the theoretical PSF is unknown.

I propose a new PSF estimation method by fitting a parameteric theoretical PSF model in Eq. (2.40) and Eq. (2.41) to a point-like object image [51, 52]. The PSF estimation and generation process can be illustrated by Fig. 3.2.

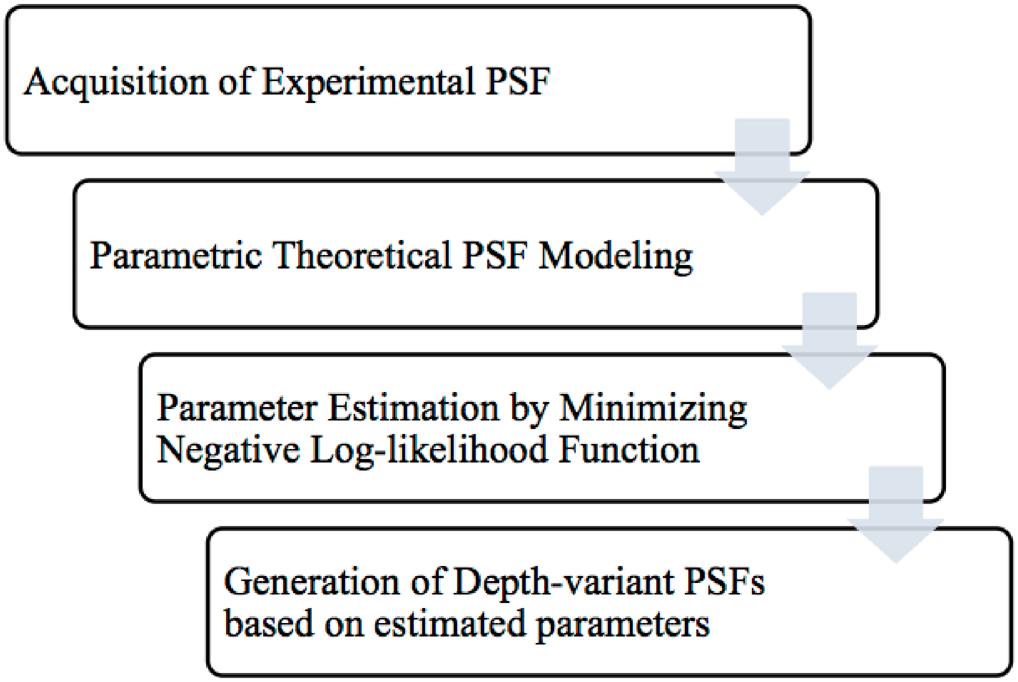

Figure 3.2: PSF estimation and generation process

For this, acquiring the 3D image of a micro-bead is proceded, which is experimental PSF. The micro-bead should be smaller than the Abbe's resolution in Eq. (2.39). A theoretical PSF (in this chapter, h means $h_{SIRS(3)}$) is calculated with pixel size and numerical aperture in accordance with WFM specification. Then, the proposed method estimate unknown parameters in theoretical PSF by minimizing the negative log-likelihood function. The likelihood function assume the Poisson distribution.

$$p\left(h_{exp}|h\right) = \prod_{\boldsymbol{p}_i} \frac{h^{h_{exp}} e^{(-h)}}{h_{exp}!} \tag{3.1}$$

where h_{exp} is experimental PSF. The Eq. (3.1) represents a probability of a point source observation. I convert maximization of likelihood to minimization of negative log-likeihood. The negative log-likelihood is defined as follows:

$$\begin{aligned}\left(\hat{z_o}, \hat{n_i}, \hat{n_s}, \hat{n_g}, \hat{t_g}\right) &= \underset{z_o, n_i, n_s, n_g, t_g}{\arg\min} \left\{ \sum_{\boldsymbol{p}_i} \left(h - h_{exp} \log\left(h\right)\right) \right\} \\ &= \underset{z_o, n_i, n_s, n_g, t_g}{\arg\min} \left\{ \sum_{\boldsymbol{p}_i} \left(h\left(\left|\boldsymbol{r}_i - \boldsymbol{r}_o\right|, z_i; z_o, n_i, n_s, n_g, t_g\right)\right.\right. \\ &\left.\left. - h_{exp} \log\left(h\left(\left|\boldsymbol{r}_i - \boldsymbol{r}_o\right|, z_i; z_o, n_i, n_s, n_g, t_g\right)\right)\right) \right\}\end{aligned} \tag{3.2}$$

In the experiment section, I report the experimental PSF and my proposed PSF results. In order to reduce a processing time for parameter estimation, the negative log-likelihood using simplified OPD equation is as follows:

$$\begin{aligned}&\left(\hat{z_o}, \hat{n_i}, \hat{n_s}\right) \\ &= \underset{z_o, n_i, n_s}{\arg\min} \left\{ \sum_{\boldsymbol{p}_i} \left(h\left(\left|\boldsymbol{r}_i - \boldsymbol{r}_o\right|, z_i; z_o, n_i, n_s\right) - h_{exp} \log\left(h\left(\left|\boldsymbol{r}_i - \boldsymbol{r}_o\right|, z_i; z_o, n_i, n_s\right)\right)\right) \right\}\end{aligned} \tag{3.3}$$

These can find the optimal parameters and the location of the micro-bead using a non-linear optimization method. When minimizing the negative log-likelihood function, I used the simplex method [53]. Among estimated parameters, controlling estimated z_i and z_o can generate depth-variant PSF.

3.2.2 GEM Algorithm

Since the depth-variant RL method is sensitive to noise, it is desired to impose a regularization function that discourages large variations in restored images to alleviate the noise effect. The regularized penalized cost function is defined as Eq. (2.25) and

Eq. (2.27). To suppress noises, I utilize GEM algorithm that is mentioned in related works part.

3.3 Experimental Results

3.3.1 PSF Estimation

In first experiment, I tested how well the proposed method fit the experimental PSF. I prepared a sample of a diluted solution of $0.2\mu m$ diameter Fluoresbrite Yellow Green Fluorescent Microspheres (Polyscience Inc., PA, USA) and dried the solution onto a cover slip. Then, the sample was imaged using a 40, 0.95 NA objective lens with an Olympus IX-71 inverted microscope. Using the 65×65×59 acquired image with spacings of $0.11 \times 0.11 \times 0.64$ μm, we estimated the PSF parameters and the location of the microbead using the method defined in Eq. (3.3). To estimate the parameters that minimize the objective function defined in Eq. (3.3), we used the simplex optimization method [54].

The acquired experimental PSF is depicted in Fig. 3.3 and Fig. 3.4. It can be seen that the experimental PSF includes non-negligible noise. I estimated parameters of theoretical PSF in Eq. (2.40) and Eq. (2.41). The generated PSF based on estimated parameters is represented in Fig. 3.5 and Fig. 3.6.

Fig. 3.7(a) and Fig. 3.7(b) show the xz sections of the acquired microbead image and the estimated PSF image (the estimated center location of the microbead on the z axis is 26.9 μm), respectively, whereas Fig. 3.7(c) and 3.7(d) show the xy sections of the acquired bead and the estimated PSF image (a slice at $z =$36.7 μm), respectively. The estimated n_i and n_s values are 1.53 and 1.13, respectively.

The normalized correlation coefficient (COR) value of the acquired image and the estimated PSF image is used for evalutation of the fitting result. The COR value is calculated as follows:

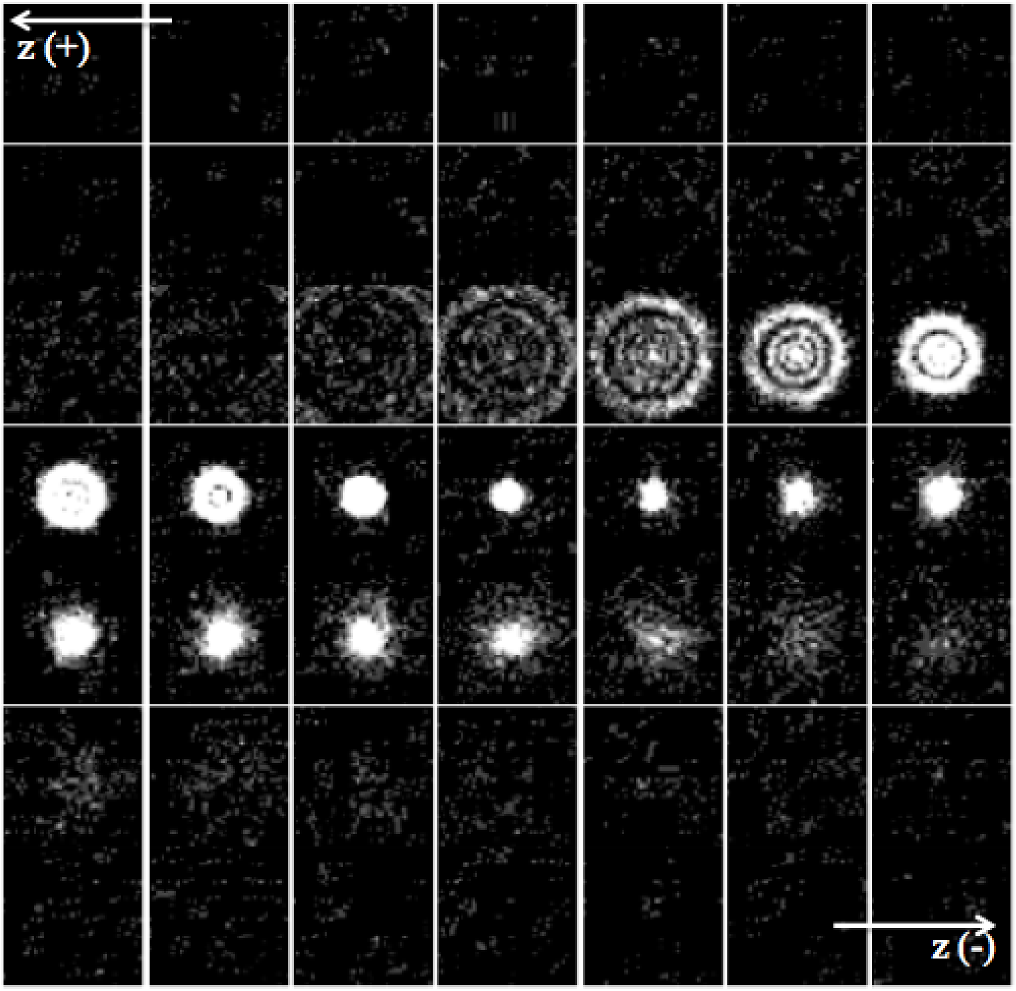

Figure 3.3: x-y profiles of experimental PSF

$$\text{COR} = \frac{\sum\left((f_{ac} - \overline{f_{ac}})(f_e - \overline{f_e})\right)}{\sqrt{\sum(f_{ac} - \overline{f_{ac}})^2 \sum(f_e - \overline{f_e})^2}} \tag{3.4}$$

where f_{ac} and f_e denote the acquired image and the estimated image, respectively. $\overline{h_{ac}}$ and $\overline{h_e}$ represent avarage of the acquired image and he estimated image, respectively. The COR value in this experiment was 0.903 (close to 1), which shows the validity of the proposed fitting method.

Figure 3.4: x-z profile of experimental PSF

3.3.2 Simulations

We conducted simulation studies to evaluate the performance of the proposed method in comparison with the invariant Richardson-Lucy (INV-RL) method, the invariant generalized expectation maximization (INV-GEM) method, and the depth-variant Richardson-Lucy (DV-RL) method. First, we generated a synthetic $20\mu m$ diameter microsphere object with its center location on the z axis being at a depth of $10\mu m$. Then, we convolved the synthetic object using the constructed PSF model under Poisson noise. We generated such synthetic noisy and blurred observed images (65×65×111, with spacings of 0.5 μm for the x, y, and z axis) for five different signal to noise ratios (SNRs) and attempted to restore the true object using the INV-RL, INV-GEM, DVRL, and DV-GEM methods. We repeated iterations of the four methods for 200 times, which ensures the relative change of objective function value is less than $1 \times e^{-5}$ for all the methods. We also tested the performance of the INV-RL and the DV-RL method with a stopping strategy [55], which attempts to avoid restoring noisy image by early termination of the iteration before convergence. To do that, we compute mean square error between restored image and true image, and terminate the iteration when the error is minimized. Although this strategy is not applicable

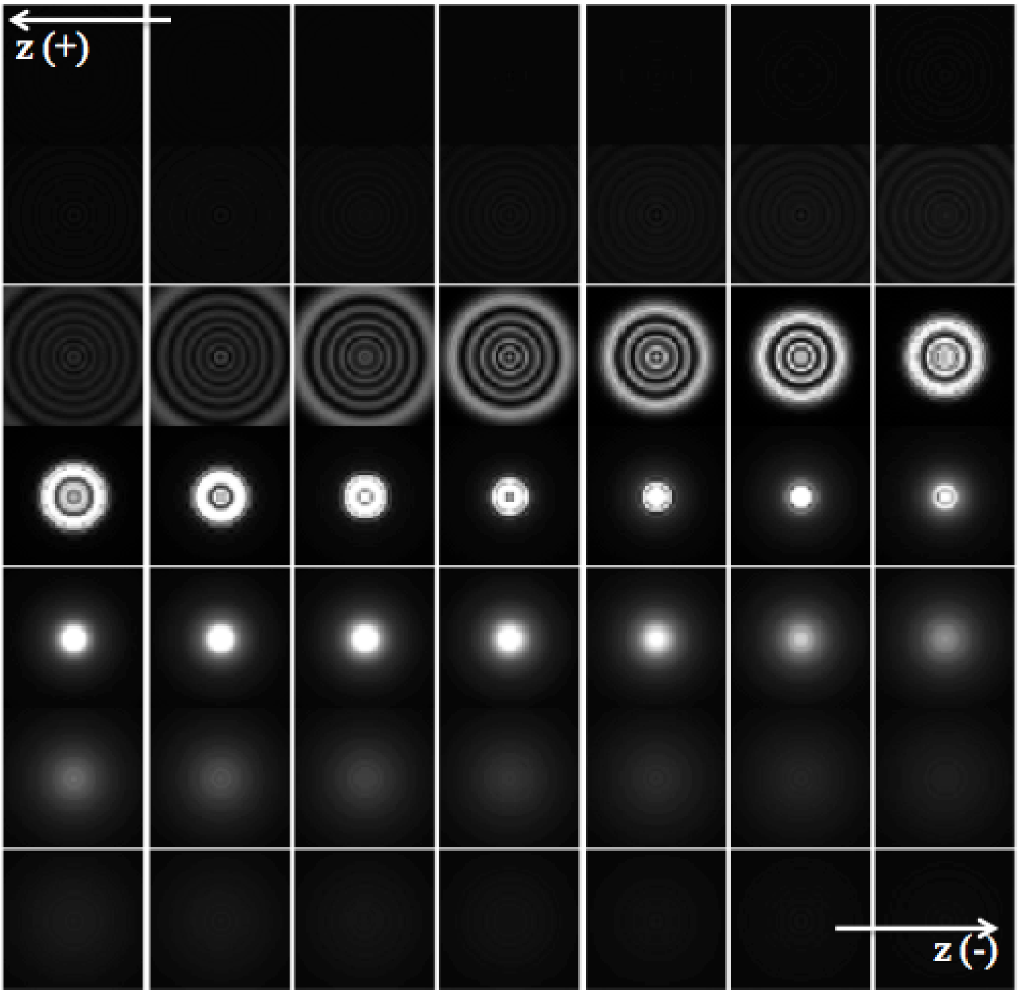

Figure 3.5: x-y profiles of estimated PSF

for real experimental data since true image is not available, we report this results for comparison purpose.

Fig. 3.8(a) and 3.8(b) show the xz profile of the true microsphere-shape synthetic object and that of the noisy blurred image used for simulation. Fig. 3.8(c) 3.8(h) show the restored images using the INV-RL, INV-RL with stopping strategy, INV-GEM, DV-RL, DV-RL with stopping strategy, and DV-GEM methods. For depth-invariant methods such as INV-RL and INV-GEM, we used the PSF model at z =10 μm for deconvolution. Fig. 3.9(a) and 3.9(b) show the xy section (at z = 10 μm) of the true object and the noisy blurred image. Fig. 3.9(c) 3.9(h) show the restored

Figure 3.6: x-z profile of estimated PSF

images using the INV-RL, INV-RL with stopping strategy, INV-GEM, DV-RL, DVRL with stopping strategy, and DV-GEM methods, respectively. As one can see in the figures, invariant methods such as INV-RL and INV-GEM were unable to effectively restore the xz section of the true object. Although the DV-RL method was able to restore the spherical shape in the xz profile, the image was noisy because the method does not incorporate a regularization function. Although the stopping strategy was able to reduce noise a little bit more than the INVRL and DV-RL methods without stopping strategy, the resulting images (Figs. 3.8(d), 3.8(g), 3.9(d) and 3.9(g)) are still noisy. Compared with other methods, the DV-GEM method restored the true object more effectively even in the presence of noise.

Table 3.1: COR values of true object image and restored images obtained by using the four methods.

	Restoration methods				
SNR (dB)	Noisy and blurred	INV-RL	INV-GEM	DV-RL	DV-GEM
30	.724	.955	.955	.975	.975
25	.723	.949	.951	.969	.973
20	.719	.932	.944	.950	.966
15	.706	.883	.944	.898	.965
10	.670	.769	.949	.778	.960

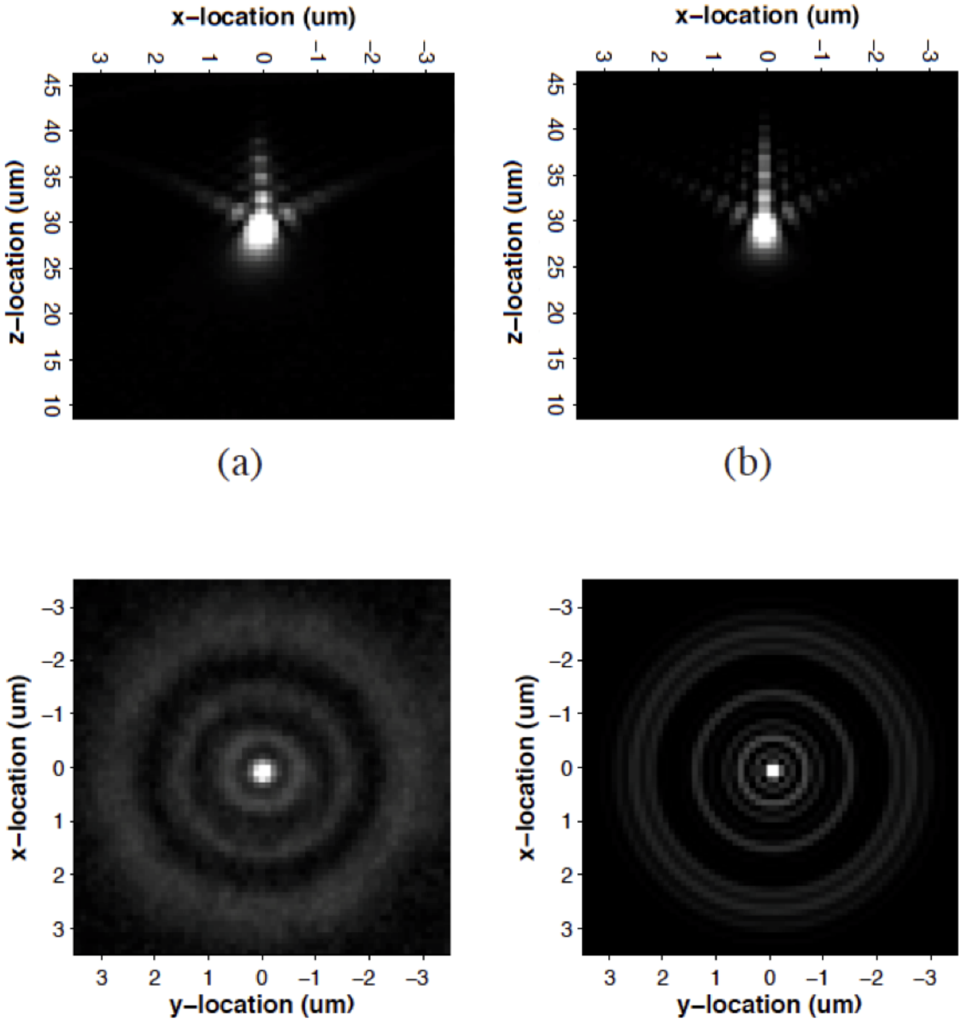

(a)

(b)

Figure 3.7: Micro-bead image and fitted PSF: (a) xz profile of acquired microbead image; (b) xz profile of estimated PSF image; (c) xy profile of acquired image at $z = 36.7\ \mu m$; (d) xy profile of estimated PSF image at $z = 36.7\ \mu m$.

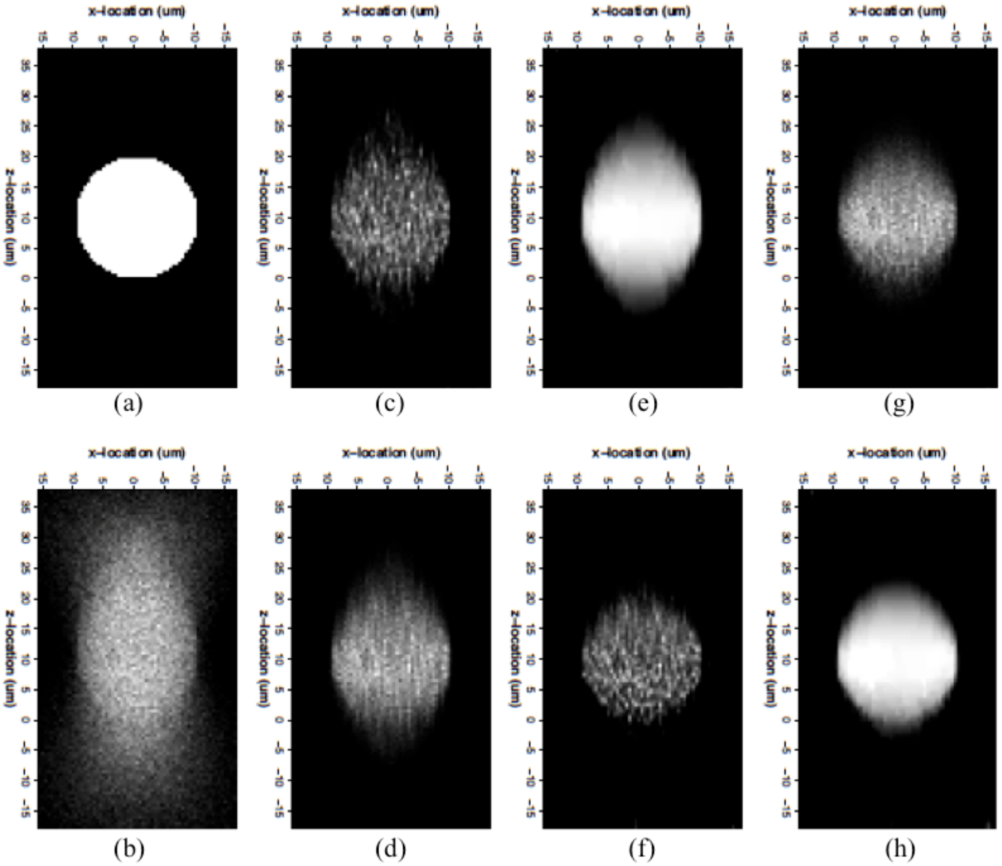

Figure 3.8: Images of xz profiles in simulation: (a) true image; (b) blurred and noisy image (SNR=15dB); (c) INV-RL; (d) INV-RL (stopping) (e) INV-GEM; (f) DV-RL; (g) DV-RL (stopping); (h) DV-GEM.

To study the statistical properties of the INV-RL, INV-GEM, DV-DL and DV-GEM methods, we repeated the restoration 10 times using 10 different noise realizations. Table.3.1 shows the average COR values between the true object and the restored images for the 10 restorations obtained by using the four methods. As shown in the table, the proposed DV-GEM method outperformed the other methods. Note that the performance of the depth-variant methods was better than that of the depth-invariant methods. In addition, the DV-GEM method outperformed the DV-RL method for all SNR cases. In particular, if the noise is severe, the performance of the DV-GEM method was much better than that of the DV-RL method. When

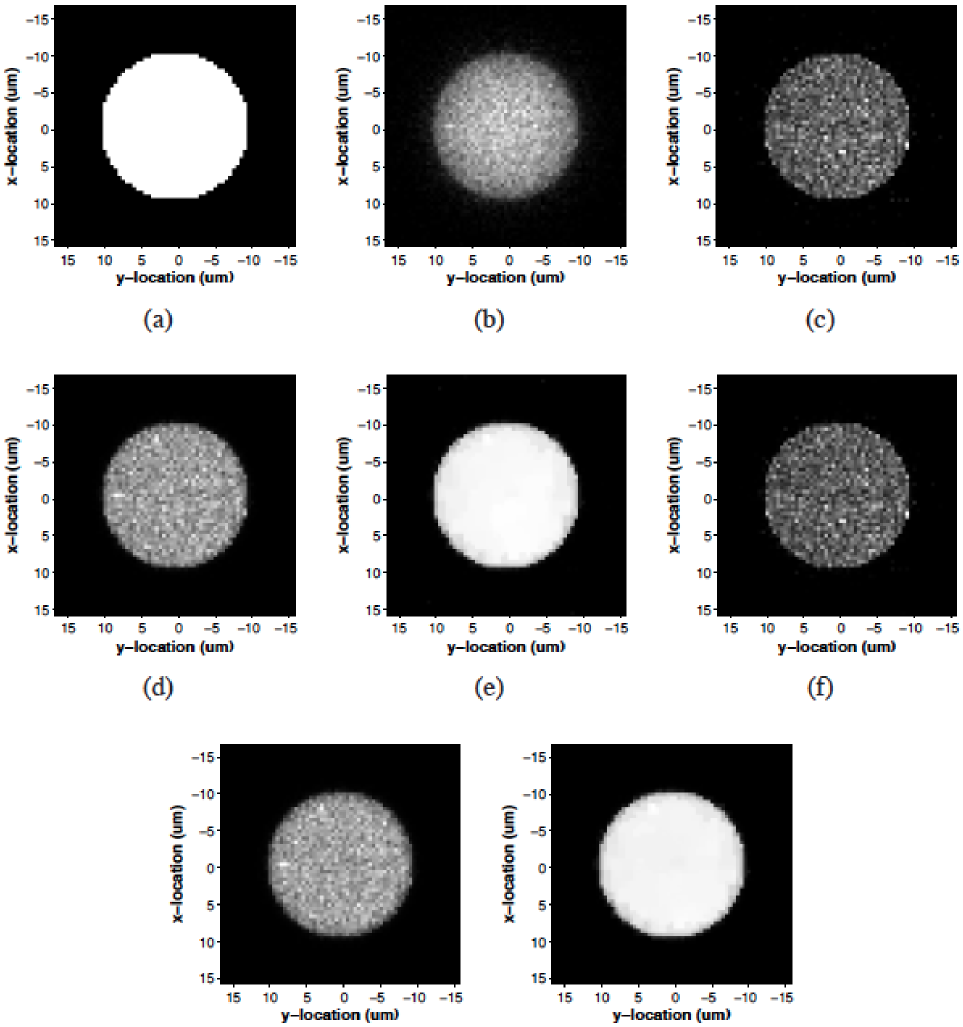
(a) (b) (c)

(d) (e) (f)

Figure 3.9: Images of xy profiles in simulation: (a) true image; (b) blurred and noisy image (SNR=$15dB$); (c) INV-RL; (d) INV-RL (stopping) (e) INV-GEM; (f) DV-RL; (g) DV-RL (stopping); (h) DV-GEM.

the SNR was very good (e.g., 30 dB case), the performance of the DV-RL was almost the same as that of the DV-GEM method. For the INV-GEM method and the DV-GEM method, we selected the regularization parameter manually in a way such that restored images are smooth enough. One may attempt to automatically tune the regularization parameter using methods such as generalized cross validation [56]. We defer investigation on the automatic regularization parameter tuning to a future study.

Table 3.2: Computation time of the four methods per iteration (unit is second).

	INV-RL	INV-GEM	DV-RL	DV-GEM
computation time	.65	.92	72.95	73.24

We also report computation time of the four methods implemented using MATLAB (Mathworks, USA). Table.3.2 shows computation time of the four methods per iteration on a workstation that has two Intel Xeon X5650 processors (2.67GHz) and 96 GB memory. As expected, depth-variant methods required much more computation time due to computationally intensive depth-variant convolution operation. However, the DV-GEM method required only slightly more computation time than the DV-RL method. Note that computation time for depth-variant methods can be reduced using a parallel processing algorithm and/or more advanced computers.

3.3.3 Bead Experiment

We also tested the performance of the proposed method for real images in comparison with the conventional methods such as the INV-RL method, the INV-GEM method, and the DVRL method. We acquired the image of 20μm diameter Fluoresbrite Yellow Green Fluorescent Microspheres (Polyscience Inc., PA, USA) under the same condition as in the acquisition of the 0.2μm diameter microbeads for the PSF estimation. Then, we attempted to restore the true object using the four methods. Fig. 3.10(a) shows the xz section of the acquired image while Figs. 3.10(b) - 3.10(e) show the results using INV-RL, INV-GEM, DV-RL, and DV-GEM methods, respectively. For the depth-invariant methods such as INV-RL and INV-GEM, we used a PSF at $z = 17.97\ \mu m$, which is around the center of the slices of the acquired microbead image, for deconvolution. As one can see in Figs. 3.10(b) and 3.10(c), the restored images based on the depth-invariant PSF have longer support size than the true image especially along the z axis. This result is consistent with the results from the simulations in the preceding subsection and results from previous investigations [57]. This problem can be reduced by using the DV-PSF for deconvolution. Fig. 3.10(d) and 3.10(e) show the restored images using the DV-RL method and the DV-GEM method, respectively. As one can see in the figures, both methods yielded better deconvolved images than the depth-invariant based methods in the sense that the support size along the z axis is closer to the truth. As expected, the DV-RL method generated a noisier image than the DV-GEM method. It is to be noted that unlike in the results from the simulation studies, the axial blur along the z axis are not removed completely. We suspect the experimental PSF is not accurate. Because it is hard to say the refractive index and the focal distance is not changed in the procedure of switching the point-like bead into the $20\mu m$ bead. Also, we suspect that the performance might be even more enhanced by using a blind deconvolution method that allows reflecting actual imaging condtion. We handle this problem in the next chapter. Fig. 3.11(a) shows that xy section of the acquired image at $z = 17.97\ \mu m$ and Figs. 3.11(b) 3.11(e) show the results using INV-RL, INV-GEM, DV-RL, and DV-GEM methods, respectively. As one can see in the figures, the total variation (TV) penalty function was able to reduce noise in the restored images without blurring edges very much.

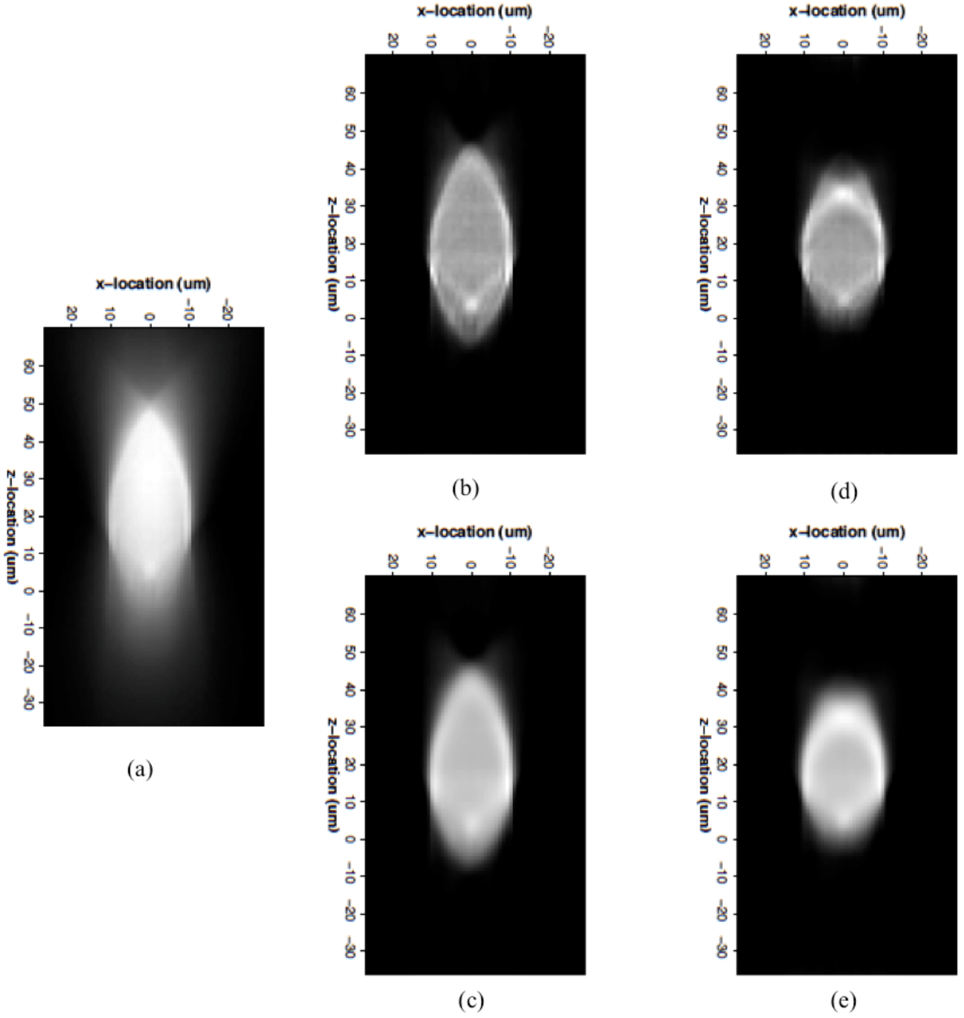

Figure 3.10: Images of xz profiles in real experiments: (a) observed; (b) INV-RL; (c) INV-GEM; (d) DV-RL; (e) DV-GEM.

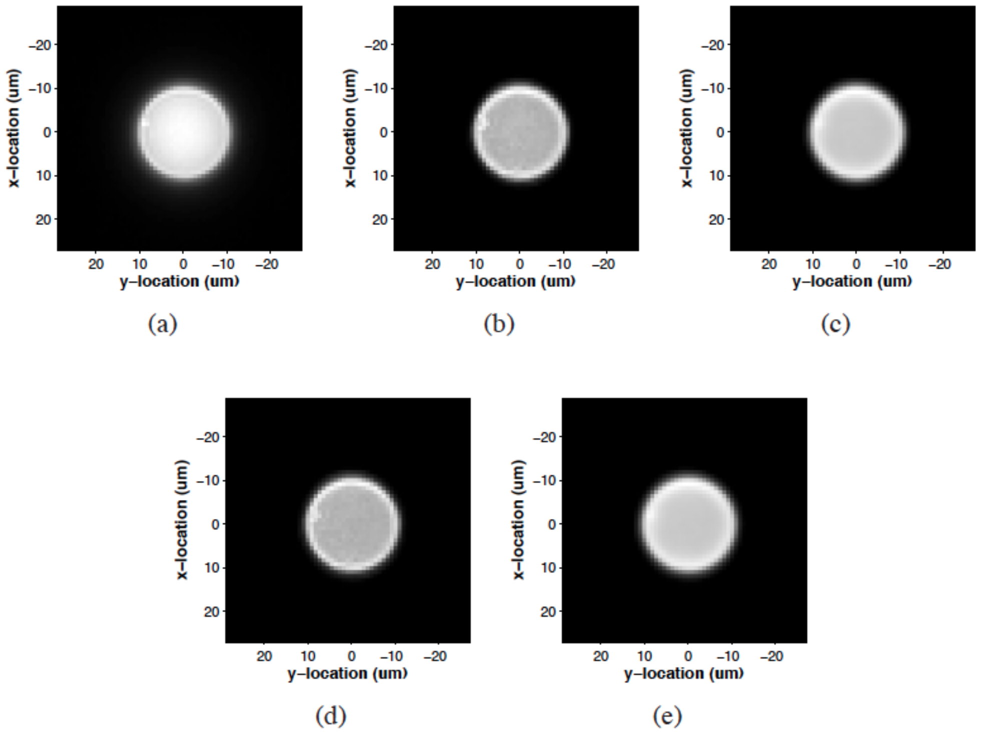

(a) (b) (c) (d) (e)

Figure 3.11: Images of xy profiles at $z = 17.97\ \mu m$ in real experiments: (a) observed; (b) INVRL; (c) INV-GEM; (d) DV-RL; (e) DV-GEM.

3.4 Discussion and Conclusion

Thic chpater investigated the deconvolution of 3D WFM images using the GEM algorithm that is based on penalized maximum likelhood estimation method and the depth-variant PSF. Using an estimated depth-variant PSF by fitting a parameterized Gibson's PSF model to an experimental microbead image, the proposed method applied the GEM algorithm for the deconvolution of 3D WFM images.

The proposed method is implemented on a PC using simuation and real images. In simulations experiments, the author evaluated performances by mean square error and normalized correlation coefficient. The proposed method showed better performance than the depth-invariant RL method, the depth-invariant GEM method, and the depth-variant RL method. And the proposed method clearly removed the axial blur in the simulation image. This result shows that the GEM algorithm could be a practical deconvolution method for WFM.

In real experiments, the auhtor conducted a qualitative performance evaluation since the ideal image is unknown. While the proposed method removes axial blur effectively in simulation experiments, the axial blur in the actual image could not removed completely. The result alludes that the experimental PSF is not accurate.

Chapter 4

Blind Deconvolution using Depth-variant PSF

This chapter addresses the challenging probelm on the axial blur removing in real images. In the previous chapter, even though previous chapter conducts depth-variant GEM deconvolution based on pre-PSF, the axial blur in the actual bead image is not completely suppressed relatively in comparison with simulation result. The result indicates that the PSF pre-measurement is meaningless. Therefore, the author assumed that the PSF should be estimated directly from captured images without any pre-measurement.

To the purpose, the author initially estimates PSF from intensity analysis of the observed image and refines the PSF from the maximum likelihood method in this chapter. A flowchart of the proposed method is depicted in Fig.4.1. From step A-a to step A-b shows the difference from the prior chapter. As depicted in Fig.4.1, the PSF is estimated from the observed image not an experimental PSF. This chapter binds step A-a, A-b and B as step 1 - estimation of depth-invariant PSF. Step C is handled as step 2 - generation of depth-variant PSF. Step D is introduced as step 3 - accelerated depth-variant GEM algorithm.

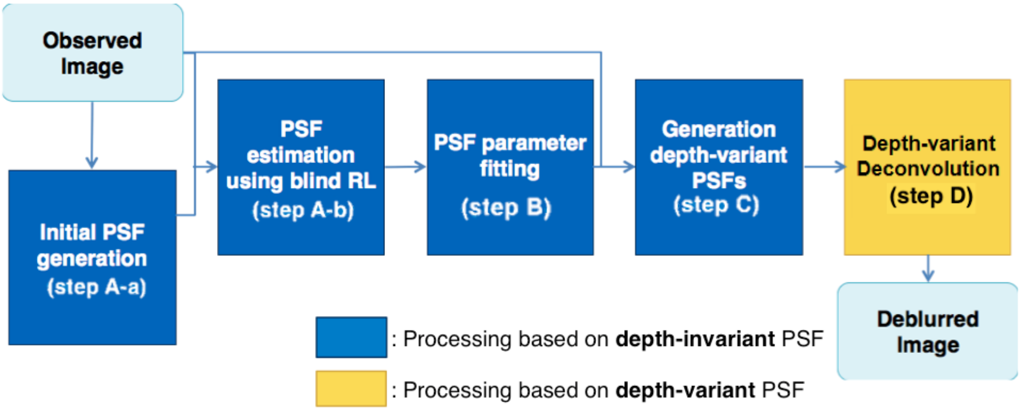

Figure 4.1: Flow chart of blind deconvolution using depth-variant PSF

The proposed deconvolution algorithm is implemented using a open data, for the comparision to exisitng studies. Since true object image of the open data is unknown, performances are evaluated by known diameter (length) of the object and known shape. These evaluation indicators are already used in the existing studies, the author also used the indicator for the comparision.

The major contributions of this study are as follows. First, a new practical WFM image deconvolution algorithm that reflects the depth variance of a PSF and actual imaging conditions is proposed. Second, it showed remarkable experimental results compared to commercial softwares and showed that the proposed algorithm solved the problem of the axial blurs.

4.1 Introduction

Aiming to improve the resolution and contrast of 3D WFM through image deconvolution, numerous studies have been carried out[1]. Most of them have conducted depth-invariant image restoration owing to a simplicity of PSF modelling[21, 37, 44, 25]. If the specimen is thin enough, the depth variance of PSF can be ignored, and their methods suppress the blur effectively, thereby increasing the resolution of 3D WFM up to that of confocal microscopy[58]. However, in case of an average size of common specimen ($10 - 20\mu m$), the axial blur along the z axis still remains [15]. For instance, the diameter of the blurred image of a $2500nm$ bead was measured as $4760nm$ (with axial blur) and $2867nm$ (with transverse blur), and after deconvolution of these values under the assumption that the specimen is thin enough, these results were respectively $4000nm$ and $2664nm$[26]. These deconvoluted values indicate that the restored image is lengthened along the optical axis. This phenomenon, called elongation, occurs when the image is restored by using a depth-invariant PSF which is only suitable for a specific plane[6]. In consideration of the fact that the general size of an animal cell is $10 - 20\mu m$, namely, much thicker than the $2500nm$ bead, the depth variance of PSF cannot be neglected. To handle the elongation problem, several researches have considered a depth-variant PSF. However, they tried only simulation[15] or bead experiments accompanied with pre-PSF measurement[6].

As for the pre-PSF measurement performed in previous studies, it was assumed that an actual PSF can be approximated by the captured 3D image of a point-like micro-bead. However, the pre-PSF measurement is meaningless because in the process of replacing a micro-bead with a cell specimen, the actual imaging condition changes. When users switch specimen into another specimen, the refractive index and the focal distance varies. This change makes the difference between the actual PSF and the result of pre-PSF measurement. In addition, a point-like micro-bead is merely a ‘point-like’ sphere and cannot be a perfect point source.

4.2 Proposed Method

The proposed method in this chapter consists of three steps. Step 1 and Step 2 are PSF estimation processes. They are divided into PSF estimation for central depth of object and depth-variant PSF generation. Step 3 is image deconvolution using the estimated PSFs in prior steps.

4.2.1 PSF Estimation

Step 1. Estimation of depth-invariant PSF

In step 1, an initial PSF is estimated first. Before the procedure for estimating PSF is explained, the method for generating the initial PSF and its specific setting are explained. The accuracy of the estimated PSF depends on the initial PSF. To generate the initial PSF, the Gibson's PSF model, which is based on Kirchhoffs integral formula (one of the most widely used PSF models for WFM), was applied [40]. This model generates a 3D WFM PSF by substituting optical parameters. These parameters are refractive indices and optical distances, which are determined by analyzing the intensity profile and objective lens information. The Gibson's PSF model is given as eq. (2.40).

A schematic of the optical path in a WFM is shown in Fig. 4.2. The OPD, $\Lambda\left(z_i, z_o, \rho\right)$, causes spherical aberration, which is modelled as [45]

$$\Lambda\left(z_i, z_o, \rho\right) = z_o\sqrt{{n_s}^2 - \mathrm{NA}^2\rho^2} + \left(z_o - z_i - \frac{z_o n_i}{n_s}\sqrt{{n_i}^2 - \mathrm{NA}^2\rho^2}\right), \tag{4.1}$$

where n_s and n_i represent the refractive indices of the specimen and the immersion layer. Since the components of a specimen are usually similar to those of water, n_s is set as the refractive index of water. Meanwhile n_i depends on the composition of immersion layer. In the case an oil-immersion objective is used, n_i is taken as the refractive index of oil.

Unknown parameter z_o denotes the position of the object on the z axis. The initial z_o setting is calculated from the intensity profile of the captured image. To make it easier to understand, setting of parameter z_o is depicted in Fig. 4.2. The object part

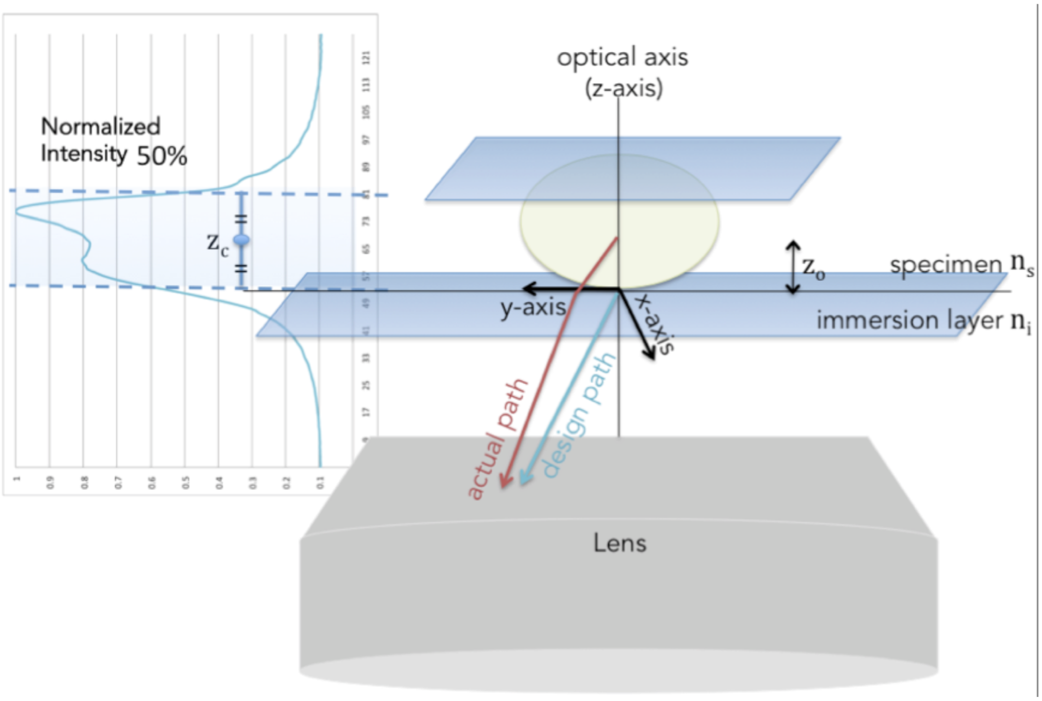

Figure 4.2: Schematic of optical path in WFM; the left graph illustrates the normalized intensity along the z axis to help understanding of initial parameter z_o. When the initial parameter z_o is set, the normalized intensity that is bigger than $[(\min(g(z_i)) + \max(g(z_i)))/2]$ in the centre of the x and y axes is supposed to be the object.

is set as normalized intensities greater than $[(\min(g(z_i)) + \max(g(z_i)))/2]$ at the origin of the x and y axes. z_o is then set as the central position z_c of the object part, under the assumption that the lowest position of the object part as $z_o = 0$. Then the initial PSF, $h(|\boldsymbol{r}_i - \boldsymbol{r}_o|, z_i; z_o = z_c)$ (in this chapter, h means $h_{DVRS(3)}$), is generated by using Equation (2.40) and (4.1).

After the initial PSF is generated, a single PSF for the overall region is estimated. In this step, a non-parameterized and image-based PSF model is used, while the initial PSF is derived from the parameterized equation. This is because the non-parameterized PSF estimation is quicker than parameterized PSF estimation.

Then the blind version of RL algorithm is used for estimating PSF.

$$\begin{aligned}\hat{f}^{s+1} &= f^{s}\left(h \otimes \frac{g}{h \otimes \hat{f}^{s}}\right)\\ \hat{h}^{s+1} &= h^{s}\left(f \otimes \frac{g}{f \otimes \hat{h}^{s}}\right)\end{aligned} \tag{4.2}$$

The blind RL algorithm iteratively estimates the true object f and the non-parameterized PSF h simultaneously from the acquired image g and the initial PSF, $h\left(\left|\boldsymbol{r}_i - \boldsymbol{r}_o\right|, z_i; z_o = z_c\right)$. The initial f is the acquired image, g. In this step, however, the blind algorithm is utilized only for estimating the PSF. The estimated PSF, $\hat{h} = h_{step1}$, is considered as the actual PSF corresponding to the centre of the object.

Step 2. Generation of depth-variant PSF

To construct depth-variant PSFs from a non-parameterized model, it is required to estimate PSFs for each depth. That estimation, however, is difficult and takes a lot of computational time. If the PSF is converted to a parameterized model, depth-variant PSFs could be effectively generated by controlling parameter z_o.

To do so, it is necessary to estimate z_o of Eq. (2.40) that minimizes a negative log-likelihood of a given $h_{step1}(\mathbf{p}_i)$ Poisson distribution.

$$(\hat{z_o}) = \arg\min_{z_o}\left\{\sum_{\boldsymbol{p}_i}\left(h\left(\left|\boldsymbol{r}_i - \boldsymbol{r}_o\right|, z; z_o\right) - h_{step1}\log\left(h\left(\left|\boldsymbol{r}_i - \boldsymbol{r}_o\right|, z; z_o\right)\right)\right)\right\} \tag{4.3}$$

Eq. (4.3) is minimized by a simplex method, which is a simple and fast mathematical optimization [53]. Iteratively, Eq.(4.3) is implemented until convergence. A parameterized PSF, $h_{step2}(\left|\boldsymbol{r}_i - \boldsymbol{r}_o\right|, z_i; z_o) = h(\left|\boldsymbol{r}_i - \boldsymbol{r}_o\right|, z_i; \hat{z_o})$, that reflects the position of the object can then be obtained. The PSF equation, namely, (2.40)(4.1), into which $z_o = \hat{z}_o$ is substituted becomes the actual parameterized PSF for the central depth of the object. And then, depth-variant PSFs are generated by shifting parameter z_o in accordance with the axial resolution of the acquired image.

4.2.2 Image Deconvolution

Step 3. Accelerated depth-variant GEM algorithm

In this step, a penalized depth-variant RL algorithm is used for restoring the depth-variant image. An image following a Poisson distribution is relatively weaker in respect to noise than a Gaussian distribution; thus, the penalized version of the RL algorithm[32] was chosen. To guarantee convergence, the GEM algorithm is used, which is defined as Eq. (2.36).

This iterative technique, however, is slow to converge toward the final result. To increase the speed of convergence, vector extrapolation is applied [4]. The acceleration method predicts where each pixel in the image is going from the correction obtained by each iteration. We restore the image using combination of Eq. (2.36) and Eq. (2.38).

4.3 Experimental Results

Datasets of the C. Elegans embryo cell and fluorescent micro-bead images were used in two experiments. The first experiment on cells aimed to show the applicability and the qualitative performance of the proposed algorithm for biological images. The second experiment on beads, applied the proposed algorithm to the images of a fluorescent micro-bead whose size and shape were given. It was thus possible to evaluate the performance of the proposed algorithm quantitatively by comparing its quantitative performance to those of three different deconvolution software packages (Huygens Pro, AutoDeblur, Deconvolution Lab) as reported by Griffa[26] and another depth-invariant method by Soulez[25]. The datasets can be downloaded from the website of the Biomedical Imaging Group (BIG) in EPFL (http://bigwww.epfl.ch/deconvolution).

Specific parameter settings and parameter curves in the case of the above-described experiments with a fluorescent bead and C. Elegans embryo cell are described in the following. Since the datasets were taken by an oil-immersion lens, the refractive index of the immersion layer is set as $n_i = 1.518$. The refractive index of the specimen is set as $n_s = 1.333$, which is the refractive index of water. Curves of parameter z_o for PSF fitting are shown in Fig. 4.3. It can be seen from the figure that the parameter-fitting procedure needs only few iterations and that the parameter curves all converge. In our experiments, the iteration was stopped if the parameter did not change three times in a row.

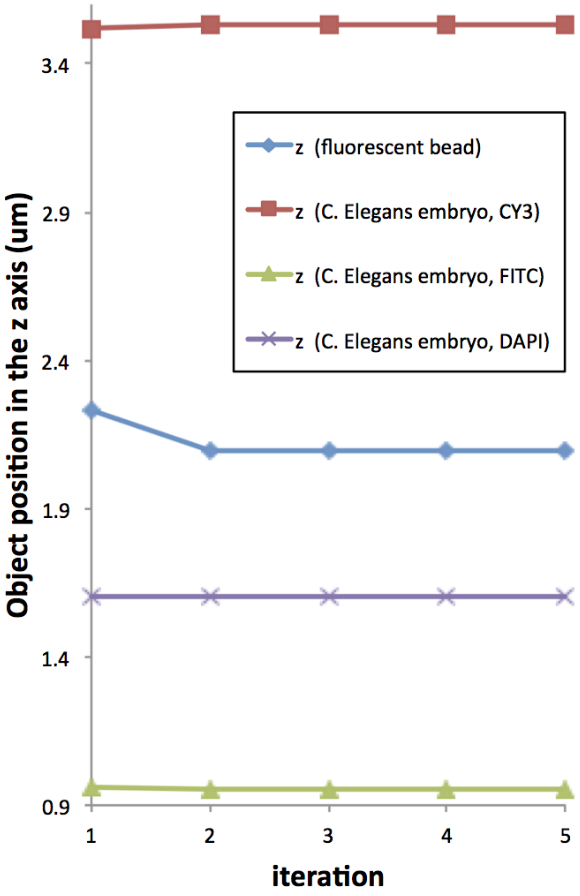

Figure 4.3: Stability of parameter z_o optimization

The regularization parameters were set as $\gamma = 0.5 \times 10^{-5}$ and 0.1×10^{-3} for the cell and bead experiments, respectively.

4.3.1 Cell Experiment

The dataset is the observation image of a C. Elegans embryo cell with a ×100, $1.4NA$ oil UPlanSApo objective. Enough image stacks should be taken to allow overall shape of a specimen to be observed. Unfortunately, the dataset did not satisfy this condition and bring artefacts on boundaries of the restored image. To avoid the boundary effect, a dataset that is pre-processed by a minimum filter is used. The specific procedure is as follows:

First, after a $672 \times 712 \times 216$ matrix was generated, the raw data of a C. Elegans embryo image ($672 \times 712 \times 104$) was put in the centre of the generated matrix (57-160 plane along z axis). Then, intensity values for the unfilled areas were determined by the minimum filter. Undetermined values bordering determined values were calculated as follows. The minimum values obtained by the minimum filter were found in the 3×3 matrix of neighbouring determined pixels, and the unfilled pixels right above or below the neighbouring determined pixels were filled in. In this way, the whole matrix was fully filled and could be used for the experiments. Through this procedure, enough z stacks could be obtained until most of the intensities along the z axis disappeared, thereby reducing artefacts at the boundary.

The data cube used was composed of $672 \times 712 \times 216$ voxels of size $64.5 \times 64.5 \times 200nm$. The PSF size ($x \times y \times z$) was set to $151 \times 151 \times 57$ voxels of size $64.5 \times 64.5 \times 200nm$. After deconvolution, the restored image was cropped to the original volume $672 \times 712 \times 104$. The dataset was composed of three stacks of images corresponding to three wavelengths. CY3 (red $634nm$), FITC (green $531nm$) and DAPI (blue $447nm$) staining represented the point-wise spots of protein, microtubule filaments and chromosomes in the nuclei, respectively. Each wavelength image was processed separately.

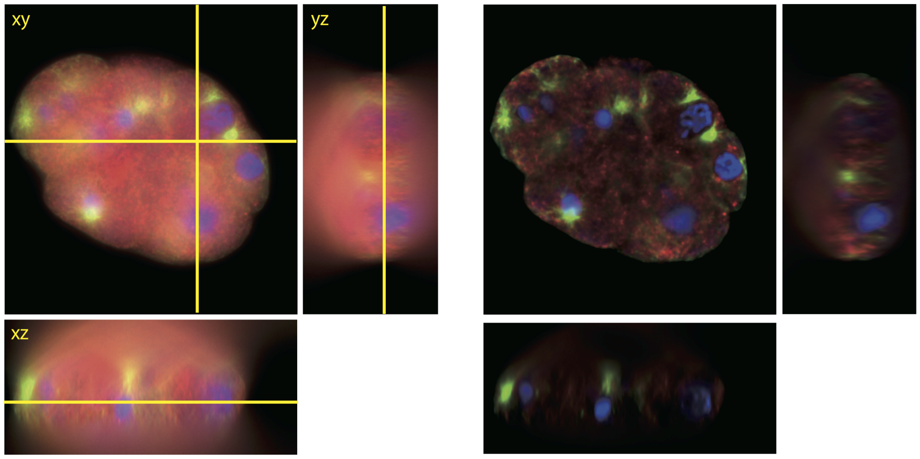

(a) Observed Image

(b) DeconvolutionLab + Downloaded PSF

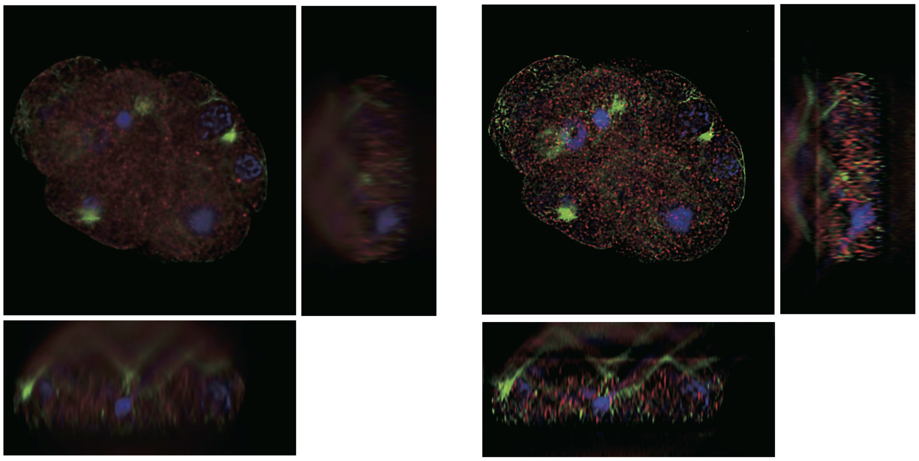

(c) DeconvolutionLab + Estimated depth-invariant PSF

(d) Our algorithm + Estimated depth-invariant PSF

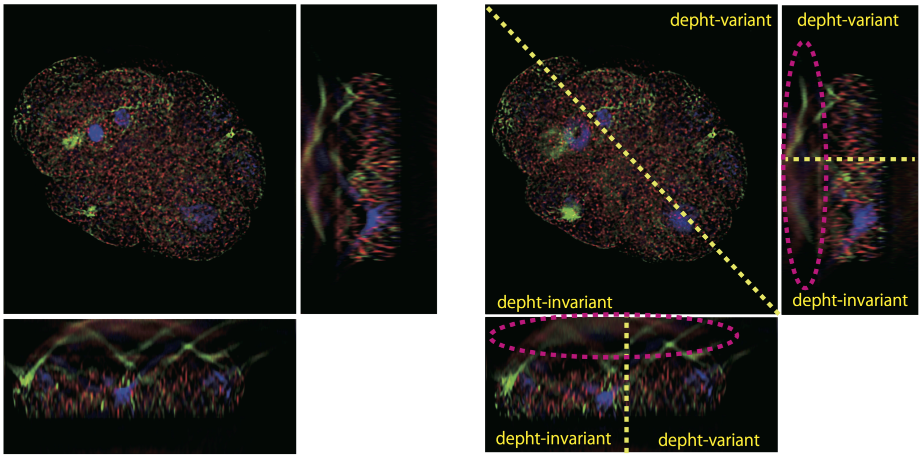

(e) Our algorithm + Estimated depth-variant PSF

(f) Comparision between our algorithm with depht-invaraint and variant PSF

Figure 4.4: Result of image restorations by proposed algorithm and by DeconvolutionLab

Table 4.1: Experimental conditions for comparison.

	Algorithm	PSF
(b)	RL (DeconvolutionLab)	PSF data from BIG
(c)		Depth-invariant PSF in step 2
(d)	GEM (Proposed algorithm)	Depth-invariant PSF in step 2
(e)		Proposed depth-variant PSF

To compare the performance of the proposed algorithm with those of existing algorithms, the results of deconvolution by a commercial software package DeconvolutionLab as well as those obtained by the proposed deconvolution algorithm are depicted in Fig. 4.4. All the experiments using ours and DeconvolutionLab were implemented with the same number of iterations 150. Table.4.1 summarizes the experimental conditions. The x-y, y-z and x-z profiles shown in Fig. 4.4 are depicted when $z = 63$, $x = 260$ and $y = 450$ pixel, respectively. Performance of each algorithm was examined in terms of qualitative visibility and computational cost.

In raw data, the image detail is represented in a narrow intensity range. The acquired images corresponding to the CY3, FITC and DAPI channels have intensity ranges of (215-2842), (209-2929) and (206-2687), respectively. Each image was deconvoluted, the ranges were widened to (0-45898), (0-24773) and (0-16292), respectively.

An observed image of a C. Elegans embryo cell is shown in Fig. 4.4(a). Since the image is blurry and unsharpened, it is difficult to identify its cellular components. A set of images restored by using DeconvolutionLab with a PSF downloaded from BIG, which was generated without consideration of actual aberration, is shown in Fig. 4.4(b). As shown in the figure, only components that had strong intensity remained, and even the remaining components are blurry. The result of image restoration using the depth-invariant PSF which was estimated in step 2 of the proposed algorithm is shown in Fig. 4.4(c). The result is still blurry, but it is improved from the viewpoint of observing specific components. It can be inferred from this result that the downloaded PSF did not reflect the actual imaging condition.

The result obtained with the proposed accelerated generalized expectation-maximization (GEM) algorithm with the depth-invariant PSF is shown in Fig. 4.4(d). The proposed algorithm had a clearer visibility than DeconvolutionLab after the same number of iterations since the image restoration was designed to guarantee the convergence and converge fast by means of vector extrapolation. The result of deconvolution by the proposed algorithm used depth-variant PSFs is depicted in Fig. 4.4(e). While the restored image in Fig. 4.4(d) is almost the same as that in Fig. 4.4(e), the restored image in Fig. 4.4(f) shows that the elongation phenomenon was suppressed by our depth-variant GEM image algorithm. Moreover, it seems that the depth-variant GEM algorithm removed blur more effectively than the depth-invariant one, as represented in the pink elliptical area in Fig. 4.4(f). When the observed C. Elegans embryo cell image in Fig. 4.4(a) is compared with the restored image in Fig. 4.4(e), it becomes clear that the proposed algorithm improves the visibility of the cellular structure. In addition, blue chromosomes, green filaments and red spots can be distinguished.

The processing time when DeconvolutionLab was used was five hours. The depth-invariant version of the proposed algorithm took only 113 minutes, which is obviously much faster than DeconvolutionLab. While the proposed depth-variant algorithm achieved better performance than that of the depth-invariant one in terms of qualitative visibility, it took more computational time (27.5 hours) than the depth-invariant version. In other words, a trade-off between performance and computational time exists.

4.3.2 Bead Experiment

Observations of a InSpeck green fluorescent hollow bead with a diameter of $2500nm$ were used as a fluorescent micro-bead dataset. The observations were taken with an Olympus Cell R microscope with a $\times 63$, 1.4 NA oil-immersion objective. The data cube was composed of $256 \times 256 \times 128$ voxels with size $64.5 \times 64.5 \times 160nm$. The PSF size $(x \times y \times z)$ was set to $151 \times 151 \times 57$ voxels of size $64.5 \times 64.5 \times 160nm$.

The diameter of the restored image was measured in terms of the full width at half maximum (FWHM), which is depicted in Fig. 4.5. As the FWHM value became closer to the real diameter ($2500nm$), the method was regarded as better one.

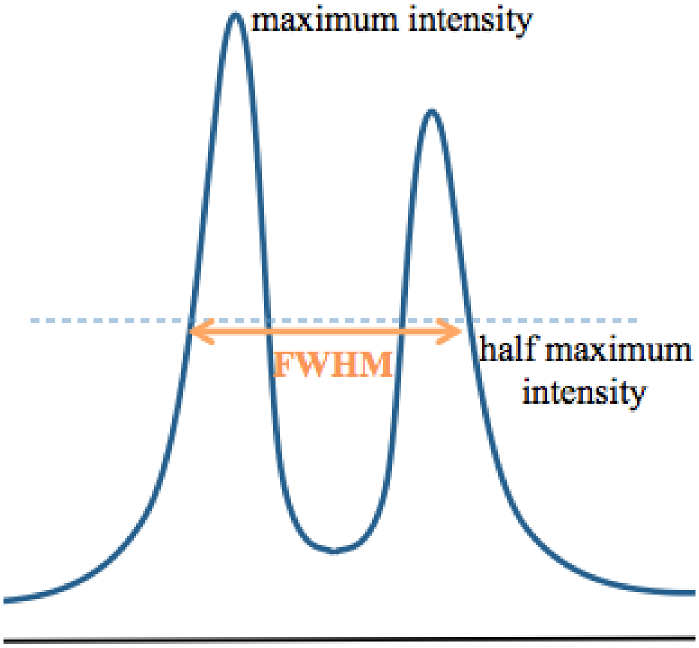

Figure 4.5: Full width at half maximum (FWHM).

The relative contrast between the border and the centre of the sphere used as a performance indicator because it was already known that the fluorescent bead was empty inside. When the relative contrast is calculated, the maximum intensity in the sphere is regarded as the border intenstiy. I described how to calculate the relative contrast in Fig. 4.6. As the relative contrast became higher, the boundary between the shell of the fluorescent bead and the hollow bead inside became more clearly distinguishable.

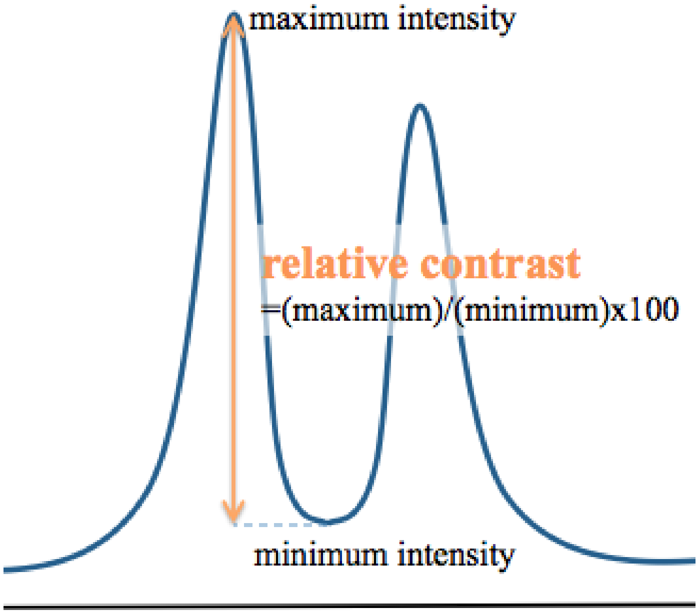

Figure 4.6: Calculation of relative contrast

Observed images and images restored by the proposed algorithm are shown in Fig. 4.7. The images were normalized by dividing maximum intensity. Images observed along the transverse axis and the optical axis are shown in Fig. 4.7(a) and (d), respectively. Images of a clear sphere shape restored from the ambiguous images in Fig. 4.7(a) and (d) respectively are shown in Fig. 4.7(b) and (e). Intensity profiles along the centre line (dotted line) in Fig. 4.7(a) and (b) are plotted in Figure 2(c), in which the horizontal axis represents the position of the transverse axis. Blue and red lines depict the intensity of the observed and restored images, respectively. As can be seen from Fig. 4.7(c), the border between the shell of the bead and the centre of the hollow sphere is definitely distinguishable. The relative contrast was calculated from the transverse intensity profiles in Fig. 4.7(c). The axial intensity profiles shown in Fig. 4.7(f) show the same tendency as those shown in Fig. 4.7(c).

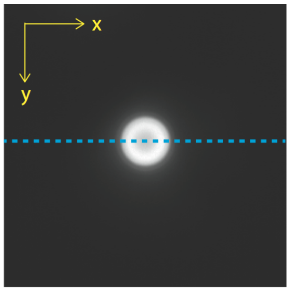

(a) Observed (xy plane)

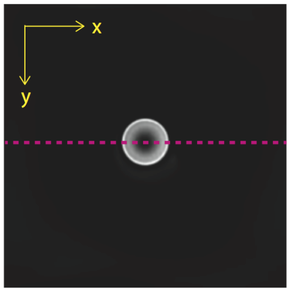

(b) Restored (xy plane)

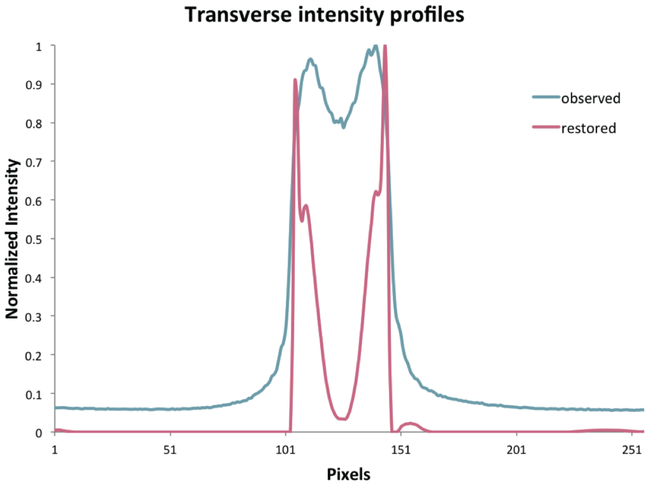

(c) Transverse intensity profiles of observed and restored image

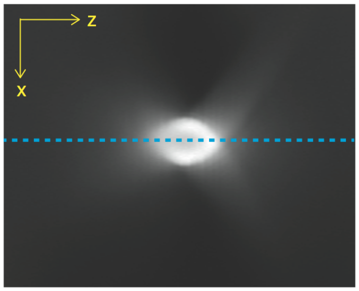

(d) Observed (xz plane)

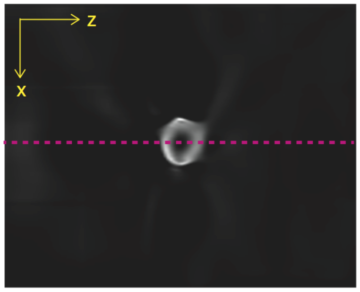

(e) Restored (xz plane)

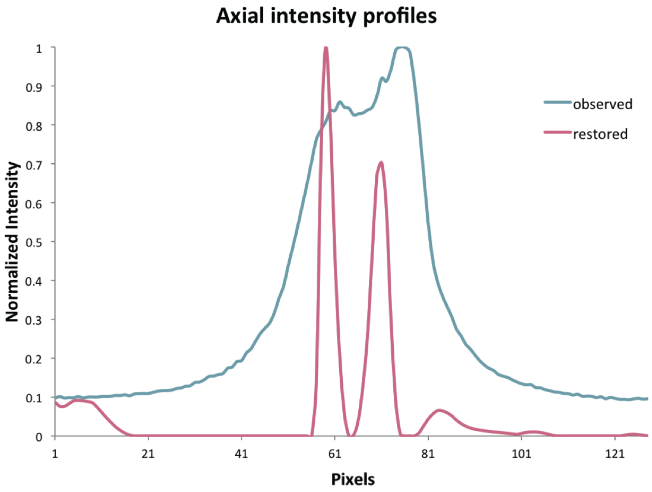

(f) Axial intensity profiles of observed and restored image

Figure 4.7: Blind depth-variant deconvolution results of 3D real fluorescence microbead images. Transverse intensity profiles in (c) are cuts along the blue dotted line in image (a) and the red dotted line in image (b). Axial intensity profiles in (f) are cuts along the blue dotted line in image (d) and the red dotted line in image (e).

It is apparent from Fig. 4.7(a) and (d) that the observed image is especially blurred along the optical axis in comparison to the transverse axis. As shown by the restored image and the intensity profile in Fig. 4.7(e) and (f), respectively, the proposed algorithm clearly removed the blur along the optical axis. This result demonstrates that the elongation phenomenon was effectively suppressed.

x-y and x-z bead image changes during iteration of image restoration are depicted respectively in Fig. 4.8 and Fig. 4.9. The bead surrounding blurs are almost removed during 10 iteration. After 40 iteration, the estimated image takes a hollow sphere form. shell of sphere and the hollow inside are quite distinct over 60 iteration.

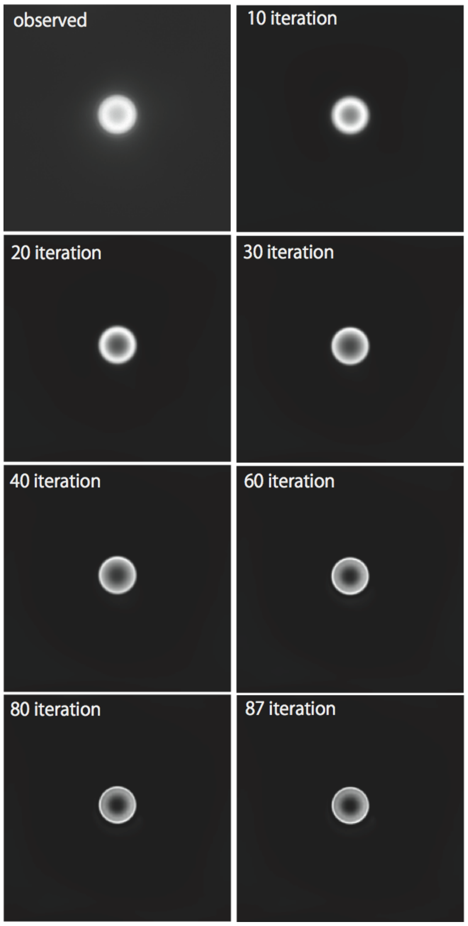

Figure 4.8: x-y bead image changes during iteration of image restoration.

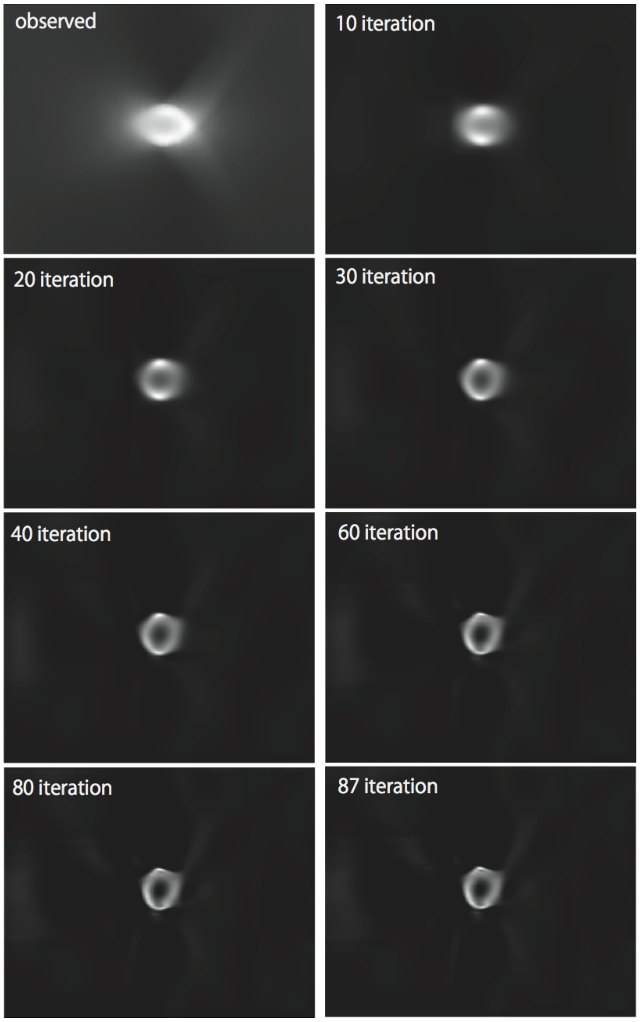

Figure 4.9: x-z bead image changes during iteration of image restoration.

Changes in the objective function, FWHM and relative contrast value during iteration of image restoration of the fluorescent bead image are shown in Fig. 4.10(a), (b) and (c), respectively. The objective function represents a negative log-likelihood function, which is calculated from Eq. (4.3). The smaller the negative log-likelihood function, the more accurately the true object is estimated. In Fig. 4.10(a), it is clear that the objective function converges enough. The iteration is stopped when the variation of obejctive function is less than 100. The results were obtained after 87 iterations. In Fig. 4.10(b), the axial FWHM value changes rapidly for ten iterations, whereas the transverse FWHM curve changes smoothly. In Fig. 4.10(c), the relative contrast rapidly increases in the early stage, namely, a similar tendency with the axial FWHM curve.

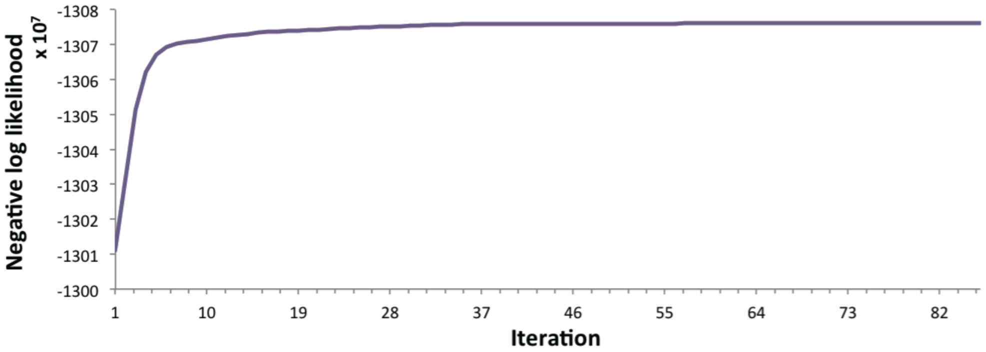

(a) objective function

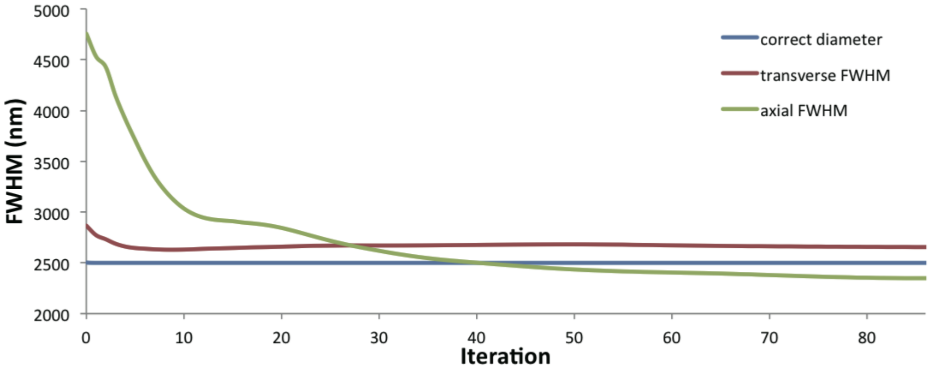

(b) FWHM curves

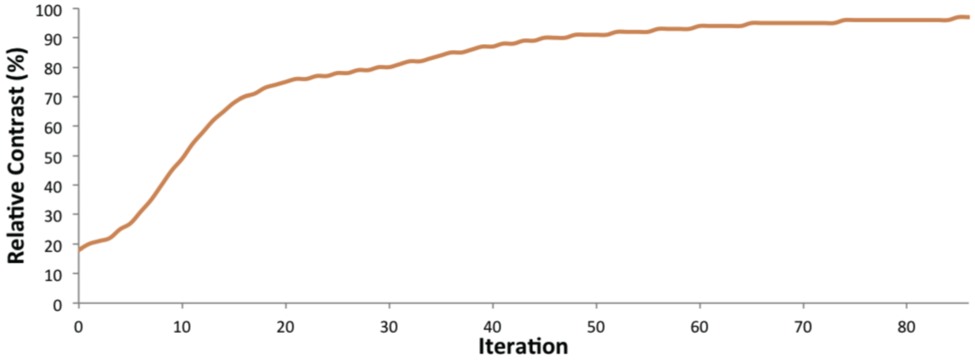

(c) relative contrast curve

Figure 4.10: (a) Objective function curve; (b) transverse and axial FWHMs computed at each iteration; (c) relative contrast curve.

Table 4.2: Performance comparison of previous [25] and proposed methods; As FWHM gets closer to true diameter (2500), the performance of the deconvolution method is better.

	Raw data	Huygens	Au.Deblur	Dec.Lab	ISBI12	Proposed
Transverse FWHM (nm)	2867	2709	2709	2664	2736	2655
Axial FWHM (nm)	4760	4000	4640	4160	2977	2349
Relative Contrast (%)	18	53	78	68	88	97

To compare the quantitative evaluation, bead diameter and relative contrast after previous deconvolution methods were applied to the images are listed in Table.4.2. As previously mentioned, the bead diameter was calculated as FWHM.

Parameter values of the observed image are presented in the 'Raw data' column. From the FWHM values of raw data, it is clear that the blur was far severer along the optical than transverse axis. As the FWHM of a deconvolution result gets closer to the true diameter (2500), the deconvolution has better performance. As shown in Table.4.2, the axial FWHM value given by the proposed algorithm was superior to those given by the other algorithms, which was closest to the true value. This is because all of them except our algorithm assumed depth-invariant PSFs; thus, this result indicated the importance of applying depth-variant PSFs. The error in the axial FWHM value given by the proposed algorithm is $151nm$, which is less than the voxel size along the optical axis ($160nm$). Although the error in the transverse FWHM value given by the proposed algorithm is $155nm$, which is equivalent to 2.34 pixels on the transverse axis, the proposed algorithm gives the best transverse FWHM value. Besides, the relative contrast given by the proposed algorithm is also superior to those values given by the other algorithms. That is, the relative contrast given by the proposed method algorithm is 97%, and those values given by the other algorithms do not surpass 90%.

4.4 Discussion and Conclusion

This study was undertaken to design a deconvolution algorithm for 3D WFM. Our proposed method removed axial blur effectively and solved the elongation problem via an accurate PSF estimation and a depth-variant image restoration. The proposed algorithm estimates a parameterized PSF reflecting actual imaging conditions, and it generates depth-variant PSFs controlling the depth parameter. A depth-variant image restoration algorithm, which is accelerated by vector extrapolation, was implemented. Results of the C. Elegans embryo cell and fluorescent bead experiment show that the proposed algorithm removes axial blur that could not be removed by algorithms developed in previous studies. Moreover, the performance values given by the proposed algorithm are superior to those given by a commercial software package used in this study. These findings suggest that 3D WFM images should be restored by a depth-variant deconvolution, and they imply that the PSF from an observation is more accurate than PSF measurement.

According to the result of the experiment with fluorescent beads, the restored image has a shape of an asymmetric sphere. In this study, however, it was assumed that the PSF is x-y symmetric. To improve the quality of the restorated image, modelling the depth-variant asymmetric PSF is considered as the next task. Further, the proposed algorithm is also applicable to other image models that have a space-variant PSF.

Chapter 5

Blind Deconvolution using Depth-variant Asymmetric PSF

For correcting distortions that occurs in deconvolution result, in this chapter, the author proposes a new deconvolution algorithm that uses a depth-variant asymmetric PSF. The proposed method estimates an actual PSF based on 3D asymmetric depth-variant model designed by Hanser [43], which reflects actual imaging condition including all aberration information. The depth-variant asymmetric PSF model is designed from a pupil function. The pupil function is composed of Zernike polynomials and parameters that represent degrees of aberrations. Since parameters are estimated from the observed image it reflects the actual imaging condition.

A flowchart of the proposed method is depicted in Fig.5.1. The process is same as the proposed method Chapter 3, however, the used PSF model is different. While Chapter 3 uses Gibson's PSF model, thie chapter uses Zernike polynomial PSF to reflect asymmetric PSF characteristic. Therefore, the pink boxed region - step A-a, step A-b and step B are different from the prior chapter. This chapter binds pink boxed rigion (step A-a, A-b and step B) as step 1 - estimation of depth-invariant PSF for central depth of object. Step C is handled as step 2 - generation of depth-variant PSF. Step D is illustrated as step 3 - accelerated GEM algorithm.

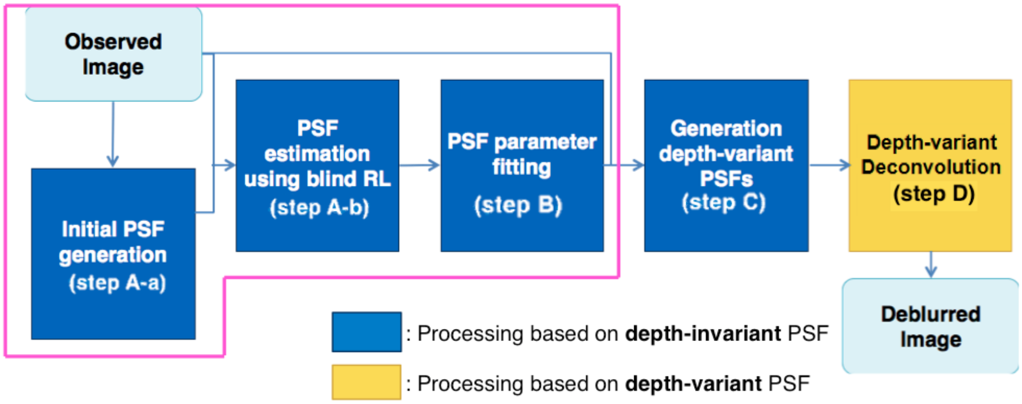

Figure 5.1: Flow chart of blind deconvolution using depth-variant asymmetric PSF

The author tests the proposed algorithm through actual images of C. Elegans embryo cell and micro-bead as same as prior chapter. The micro-bead has determined diameter and hollow sphere shape. The diameter and the relative contrast between shell and hollow inside is used for performance indicators. Also, to evaluate symmetry, the author added standard deviation values of diameter and shell intensities along x, y and z as symmetry indicators. The author shows performances according to all indicators - diameter, relative contrast and standard deviations. Experimental results show distortion free and more accurate deconvolution result.

Moreover, the author summarizes performance and computational cost according to deconvolution algorithms, thereby, which makes users have easier and wiser choice among various algorithms. An analysis of the computational cost in terms of image size is also addressed, which makes users predict computational cost according to image size.

5.1 Introduction

The estimation of 3D WFM PSF is tricky because the PSF has unique characteristics such as depth-variance, axial asymmetry and specimen-dependence. Axial asymmetry occurs by mismatch between the refractive indices of the immersion medium and the specimen. As the WFM focuses on a deeper depth of specimen, this mismatch becomes severe. This is why the PSF has depth-variant characteristic. Besides, specimen-dependence is because each sample has different refractive index and different focal point (depth) for that.

A simple existing method to obtain 3D WFM PSF is an observation of a point-like object at each depth[6]. The observation is called an experimental PSF and it reflects an imaging condition such as actual diffraction and aberration information. However, the experimental PSF has a difficulty to place the point-like object at specific depths, and it involves noises. And above all, the imaging condition of experimental PSF is different from one of actual imaging; therefore, the experimental PSF is not practical. On the other hand, most existing studies use Gibson and Lanni PSF parametric model[40]. The parametric PSF model is noise free, however, it is also not practical since it contains unknown parameters such as the actual depth and the actual refractive index of specimen. To apply actual images, the authors have already proposed a blind depth-variant deconvolution method in Chapter 4, which estimates the PSF directly from the captured images. Its experimental results outperform the previous methods in terms of suppressing blur along optical (depth) axis. This result indicates that the blind deconvolution is promising way to achieve accurate deconvolution result. However, the deconvolution result image of a perfect sphere object showed a distorted sphere shape. This result implies that PSF include non-ignorable radial asymmetry as well as depth-variance, axial asymmetry and specimen-dependence.

To involve the radial asymmetry in PSF, this paper utilizes Hanser's PSF model [43]. The Hanser's PSF model can express radial asymmetry of PSF through desigining distorted pupil fuction of lens[43]. We simplify parameters of the Hanser's PSF model so as to be applicable to practical image. Then, we directly estimate practical parameters of the simplified Hanser's PSF model from the observed image. Details are described in proposed method section. Deconvolution results show that our proposed method improves distortion as well as out-of-focus blur. Moreover, we compare performances and computational costs of previous and our algorithms.

5.2 Proposed Method

We first introduce our simplified Zernike polynomial PSF model. Then we describe process of our deconvolution algorithm. Our method is composed of three steps - estimation of depth-invariant PSF for central depth of object (step 1), generation of depth-variant PSF (step 2) and accelerated generalized expectation-maximization (GEM) algorithm (step 3). Since step 1 and 2 are based on the simplified Zernike polynomial PSF model, step 1 and 2 of the proposed method are different from our previous method in Chapter 4.

Subsequently, memory requirement for our algorithm is described, which helps users to select suitable PSF model in accordance with required performance and memory specifications. Also, performance indicators for quantitative performance evaluation in bead experiment are introduced. Due to lack of symmetry indicators, we devised new indicators for quantitative evaluation. We also introduce them in detail.

5.2.1 PSF Parameterization

We use Zernike polynomial PSF model that can describe depth-variant and asymmetric characteristics of a WFM PSF. However, Zernike polynomial PSF model has too many parameters (79 parameters) and it can lead a bad estimated result although well fitted data. Also, involving all types of aberration parameters requires expensive computational cost; choosing several parameters of major aberrations is required. We propose to remove of phase part ϕ and minor aberration parameters in modulus part ω which are minor influence factors to PSF. Then the distorted pupil function in Eq. (2.46) is simplified as:

$$p(k_x, k_y) = \omega(k_x, k_y) = \sum_{n=4,7,8,12} M_n Z_n(k_x, k_y) \tag{5.1}$$

Among various aberrations due to lens imperfection, coma and spherical aberration are major influence factor to PSF, we parameterized amplitudes of following aberrations - defocus M_4, spherical M_7, x-coma M_8 and y-coma M_{12} aberration. These aberration factors are dominant than other aberrations [59]. As piston and tilt aberration have no effect on the PSF, we set $M_0 = M_1 = M_2 = 0$. In addition, location (depth) in z axis in the object space, z_o is also involved. Namely, unknown and to be estimated parameters are set as 5 parameters - depth z_o, defocus M_4, spherical M_7, x-coma M_8 and y-coma M_{12}. We defined the aberration parameters vector as $\mathbf{M} = \{M_4, M_7, M_8, M_{12}\}$.

The author that proposed Zernike polynomial PSF not only derived the PSF model but also successfully reconstructed an observation of a point-like object [43]. Few previous studies proposed that such reconstruction of a point-like object can be utilized as PSF [6, 60]. However, the reconstruction is not accurate because the observation of an point-like object is different from a sample to observe. Therefore, we directly estimate PSF from observed image (which is called blind deconvolution) to reflect observation environment and specimen-dependence of PSF. All process of our algorithm is implemented based on the simplified Zernike polynomial PSF model.

5.2.2 Blind Deconvolution

Step1: estimation of depth-invariant PSF for central depth of object

Before estimating the PSF, first we generate an initial PSF. Most algorithms generate initial PSF as no aberration PSF. Since accuracy of PSF estimation result relies on initial PSF, we generate an initial aberrated PSF through analyzing the observed image, which is already proposed in our previous chapter. An initial parameter for depth z_o is determined under the assumption that the object is placed in normalized intensities bigger than $[(\min(g(0,0,z_i)) + \max(g(0,0,z_i)))/2]$. Then, the central position z_c in the object becomes the initial depth. Other initial parameters that represent degrees of lens aberrations $\mathbf{M}$ are assumed as 0. Applying these initial parameters to the parameterized PSF model in Eq. (2.43) and Eq. (2.44) generates the initial PSF h_{init}.

After the initial PSF generation, we find depth-invariant PSF using blind Richardson-Lucy (RL) algorithm, which plays a role in modification of the PSF. This procedure is the same with our previous chapter except PSF model for initial PSF generation. The found depth-invariant PSF h_{step1} is regarded as the PSF for the center of the object and it is non-parameterized.

Step2: generation of depth-variant PSF

This step parameterizes and generates depth-variant PSFs. For keeping the form of WFM PSF and easy generation of depth-variant PSFs, the estimated depth-invariant PSF should be parameterized. Eq. (5.2) illustrates the depth-invariant PSF fitting to the simplified Zernike polynomial PSF model. z_o and aberration parameters

M_4,M_7,M_8 and M_{12} in pupil function are alternatively and iteratively estimated.

$$\begin{aligned}
(\hat{z_o}) &= \arg\min_{z_o} \left| \sum_{\boldsymbol{p}_i} \left\{ h_{DV(4)}\left(\boldsymbol{p}_i, z_o; \mathbf{M}\right) - h_{step1} \log\left(h_{DV(4)}\left(\boldsymbol{p}_i, z_o; \mathbf{M}\right)\right)\right\} \right| \\
\left(\hat{\mathbf{M}}\right) &= \arg\min_{\mathbf{M}} \left| \sum_{\boldsymbol{p}_i} \left\{ h_{DV(4)}\left(\boldsymbol{p}_i, \mathbf{M}; z_o\right) - h_{step1} \log\left(h_{DV(4)}\left(\boldsymbol{p}_i, \mathbf{M}; z_o\right)\right)\right\} \right|
\end{aligned} \tag{5.2}$$

Since the effect of refractive index mismatch on actual PSF is relatively bigger than one of aberration parameters in pupil function, parameter estimation of PSF starts from z_o estimation. After estimation of z_o and $\mathbf{M}$, depth-variant asymmetric PSFs are then easily computed by shifting the parameter z_o in accordance with the axial resolution of the acquired image. The image location in z axis z_i also should be shifted as much as z_o moved. All the generated PSFs are normalized so its sum adds up to 1. Depth-variant PSFs generated this way become practical PSFs that reflect actual imaging condition since parameters are found from the observed image.

Step3: accelerated GEM algorithm

Using generated depth-variant asymmetric PSFs, the depth-variant GEM algorithm is implemented. GEM algorithm is well known as a solution of ill-posed problem and guarantees convergence [27]. The accelerated GEM algorithm is introduced in Chapter 4.

5.2.3 Memory Requirement

Table.5.1 shows memory requirements corresponding to each PSF model. Second, third and forth column in Table.5.1 represent memory requirements for space-invariant PSF ($h_{SIRS(2)}$ and $h_{SI(3)}$), depth-variant PSF ($h_{DVRS(3)}$ and $h_{DV(4)}$) and space-variant PSF ($h_{F(6)}$), respectively. X, Y and Z in Table.5.1 represent observed

Table 5.1: Memory requirements of the proposed deconvolution using each PSF model

	$h_{SIRS(2)}$, $h_{SI(3)}$	$h_{DVRS(3)}$, $h_{DV(4)}$	$h_{F(6)}$
image g loading	$XYZD$		
PSF h loading	$XYZD$	XYZ^2D	$(XYZ)^2D$
sum of multiples between f and h			
sum of multiples between g and $\frac{h}{\sum(fh)}$			
total variation $R(f)$	$7XYZD$		
Total memory	$11XYZD$	$(8+3Z)XYZD$	$(8+3XYZ)XYZD$

Table 5.2: Memory requirements according to image sizes with double data type

$x \times y \times z$ voxel size	$h_{SIRS(2)}$ and $h_{SI(3)}$	$h_{DVRS(3)}$ and $h_{DV(4)}$	$h_{F(6)}$
$256 \times 256 \times 128$ (exp 1)	0.688GB	24.5GB	1.50PB
$672 \times 712 \times 216$ (exp 2)	8.47GB	505GB	228PB

image size along x, y and z-axis. D in Table. 5.1 denotes data size per voxel. For example, image with double data type has 8 bytes for 1 voxel.

As shown in Table.5.1, adding depth-variance (variance along z axis) increases total memory required ($11XYZD \rightarrow (8+3Z)XYZD$). In addition, adding radial-variance (variance in x-y plane) increases the total memory required even more ($(8+3Z)XYZD \rightarrow (8+3XYZ)XYZD$). From this, it can be noted that total memory requirement for our deconvolution method depends on the degree of space-variance.

The total amount of memory requirements of our deconvolution method is sum of memory requirements of followed procedures in image loading, PSF loading, two sums of multiples and total variation. Eq.(2.37) shows that our deconvolution method involves these procedures. In case of PSF loading, even if PSF size is smaller than image size, PSF size is expanded to observed image size in order to multiple in frequency domain. We generated PSFs so that the sum of all the pixels of the PSF be unity. Since the sum of PSF in the whole image domain is impossible, we assumed that intensity spreads inside the PSF size. Total variation for all types of PSF involves derivatives of pixels and it requires 7 times of image size (front, back, left, right, top and bottom from reference image). Memory requirement for total variation holds a large percentage in space-invariant algorithm, however not in depth-variant and space-variant algorithms.

In case of deconvolution using a space-invariant radially symmetric PSF, sum of multiples can be replaced with a convolution operation. Since the PSF is space-invariant, sum of multiples can be calculated by a single convolution operation. On the other hand, deconvolution using depth-variant PSFs requires depth-variant PSFs as a number of depth and the sum of multiples can be replaced with a convolution operation for every single depth, regardless of radial asymmetry. In case of deconvolution using a space-variant PSF, space-variant PSFs are needed as a number of pixels and the sum of multiples cannot be replaced with a convolution operation. Therefore, deconvolution using space-variant PSFs requires huge amounts of memory.

Memory requirements for images that will handle in expeirment section are also depicted in Table.5.2. Table.5.2 assumes double data type. The memory requirement for each experiment and other possible image sizes can be obtained by formulas in Table.5.1, this means the memory requirement of the proposed algorithm according to various image sizes can be expected easily. We will compare expected memory requirements in Table.5.2 and actual computational memory in the experiment section.

Total memory requirements for $256 \times 256 \times 128$ voxels using a space-invariant radially symmetric PSF, depth-variant PSFs and space-variant PSFs are approximately 0.688GB, 24.5GB and 1.5PB, relatively. Total memory requirements for $672 \times 712 \times 216$ voxels using a space-invariant radially symmetric PSF, depth-variant PSFs and space-variant PSFs are approximately 8.47GB, 505GB and 228PB. These expected memory requirements are depicted in 2nd and 3rd row of Table.5.2. At present, a regular desktop PC can have 512GB RAM on Windows 8 Pro and Enterprise. From these values, depth-variant deconvolution is possible in the present.

5.2.4 Evaluation Method

As introduced in related works, image deconvolution result of micro-bead can be utilized to evaluate deconvolution performances since the bead has determined diameter and hollow sphere shape. The diameter and relative contrast between shell and hollow inside were used as performance indicators. The diameter of the restored image was measured in terms of the full width at half maximum (FWHM). As the FWHM value becomes closer to the real diameter, the method is regarded as better one. The relative contrast between the border and the center of the sphere also used as a performance indicator because it was already known that the fluorescent bead is empty inside. As the relative contrast value becomes higher, the boundary between the shell of the fluorescent bead and the hollow bead inside becomes more clearly distinguishable.

However, these values do not show symmetry of the sphere. Therefore, we added performance indicators that represent symmetry - standard deviation values of FWHM and intensity peak ratio. The intensity peak ratio is depicted in Fig.5.2.

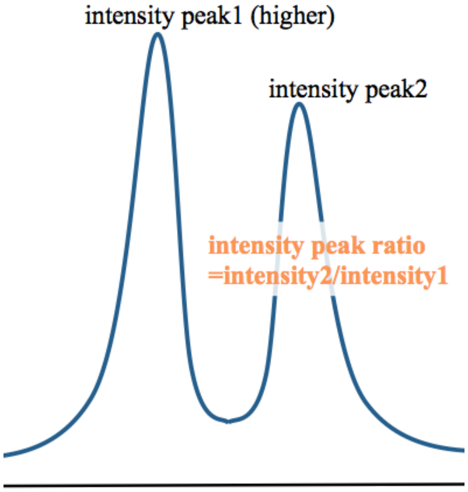

Figure 5.2: Intensity peak ratio

After obtaining FWHM and intensity peak ratio along x, y and z axis, their standard deviation values are calculated by:

$$\begin{aligned}\sigma_{FWHM} &= \sqrt{\frac{\left\{\left(X_F - \bar{F}\right)^2 + \left(Y_F - \bar{F}\right)^2 + \left(Z_F - \bar{F}\right)^2\right\}}{3}} \\ \sigma_{PA} &= \sqrt{\frac{\left\{\left(X_P - \bar{P}\right)^2 + \left(Y_P - \bar{P}\right)^2 + \left(Z_P - \bar{P}\right)^2\right\}}{3}}\end{aligned} \tag{5.3}$$

X_F, Y_F and Z_F denote FWHM along x, y and z axis. X_P, Y_P and Z_P denote intensity peak ratio along x, y and z axis. $\bar{F}$ represents average of FWHM values, which is calculated by $\bar{F} = \left(\frac{X_F+Y_F+Z_F}{3}\right)$. Similarly, $\bar{P}$ represents average of intensity peak ratio, which is calculated by $\bar{P} = \left(\frac{X_P+Y_P+Z_P}{3}\right)$. Standard deviation values in Eq. (5.3) express the symmetry of diameter and intensity symmetry, respectively. As their values become smaller, the result has symmetric shape and better performance. In the following section, we evaluate and compare performances of the proposed and previous algorithms not only qualitatively but also quantitatively by introduced performance indicators-FWHM, relative contrast and standard deviation values of FWHM and intensity peak ratio.

5.3 Experimental Results

Datasets for experiments are observations of fluorescent micro-bead and C. Elegans embryo cell; the datasets can be downloaded from the website of the Biomedical Imaging Group (BIG) in EPFL (http://bigwww.epfl.ch/deconvolution). The following section shows the deconvolution result of the proposed algorithm to the images of a fluorescent micro-bead whose size and shape were given. It is thus possible to evaluate the performance of the proposed algorithm quantitatively by comparing size and shape of deconvolution result. Lastly, the C. Elegans embryo cell experiment shows the validity of proposed method to biological images.

5.3.1 Bead Experiment

In this section, an observation of InSpeck green fluorescent hollow bead with a diameter of $2500nm$ was used (http://bigwww.epfl.ch/deconvolution/?p=bead). The observation was taken with an Olympus Cell R microscope with a ×63, 1.4 NA oil-immersion objective. The downloaded data cube was composed of $256 \times 256 \times 256$ voxels. We cropped the data as $256 \times 256 \times 128$ voxels with size $64.5 \times 64.5 \times 160nm$ so as to compare performances of previous methods and ours. Because previous methods also used the cropped version. The PSF size $(x \times y \times z)$ was set to $151 \times 151 \times 57$ voxels of size $64.5 \times 64.5 \times 160nm$. The regularization parameter in bead experiment was set as $\gamma = 0.1 \times 10^{-3}$.

Fig.5.3 summarizes bead image deconvolution results of previous and our algorithms. Fig.5.3 (a) shows the cropped raw data and yellow dotted line in Fig.5.3 represents $2500nm$. The bead shape in deconvolution result fits closer to yellow dotted line, the deconvolution algorithm shows better performance. We also summarized FWHM (bead diameter), relative contrast, standard deviation of FWHM and standard deviation of intensity for each algorithm in Table.5.3. These quantitative results correspond to the deconvolution result in Fig. 5.3. To easier understand, FWHM and relative contrast values of deconvolution result of each algorithm are plotted on a graph, which is depicted in Fig. 5.4. We also make a graph of computational costs for each algorithm, which is represented in Fig. 5.5. First, we compared blind and non-blind deconvolution results. The PSF for non-blind deconvolution is the downloaded PSF in the website of the Biomedical Imaging Group (BIG) in EPFL (http://bigwww.epfl.ch/deconvolution/?p=bead). The PSF for blind deconvolution is found by our proposed PSF estimation method with Gibson and Lanni

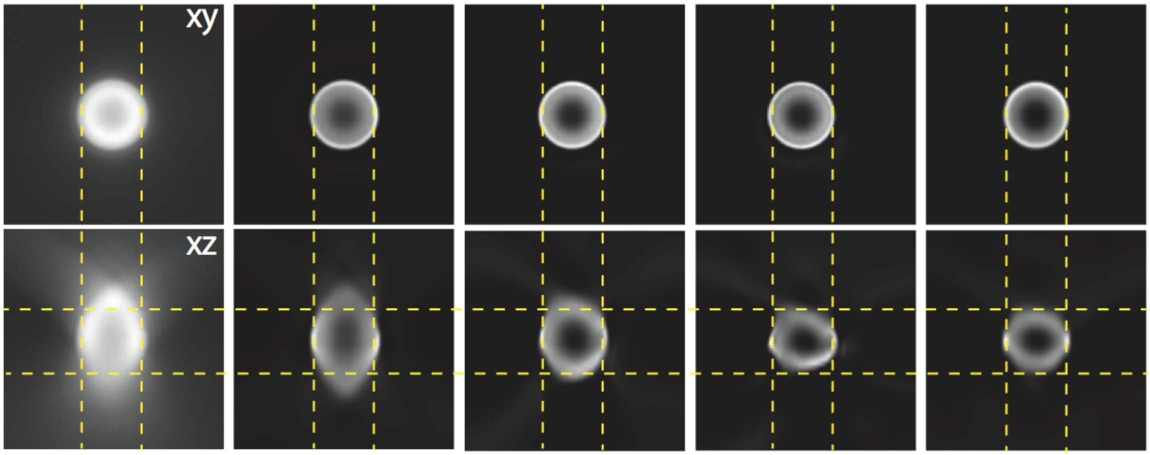

(a) raw data
(b) non-blind (downloaded PSF)
(c) blind (depth-invariant radial symmetric PSF)
(d) blind (depth-variant radial symmetric PSF)
(e) blind (depth-variant asymmetric PSF)

Figure 5.3: Comparison of Deconvolution methods for 3D data of a fluorescence bead

Table 5.3: Comparison of Deconvolution methods for 3D data (256 x 256 x 128) of a 2500 nm diameter bead

			ISBI12	(b)	(c)	(d)	(e)
		Blind	✓		✓	✓	✓
		Depth-dependent				✓	✓
		Asymmetric	✓				✓
FWHM	Reconstruction Error	Transverse (nm)	236	243	153	155	180
		Axial (nm)	477	1834	670	151	84
	Standard Deviation (nm)		-	-	-	190	143
Intensity	Relative Contrast (%)		88	86	94	97	98
	Standard Deviation (%)		-	-	-	12.8	4.4
Comp. Cost	Processing Time (min)		-	4.6	80	155	164
	Memory (GB)		-	2.04	1.82	22.2	22.2

PSF model[40]. For the sake of comparision, we used a single Gibson and Lanni PSF in this experiment so that the PSF has depth-invariant and radially symmetric characteristics, which is the same condition as the downloaded PSF. Fig.5.3 (b) and (c) depict their deconvolution results.

While the deconvolution result of non-blind deconvolution in Fig.5.3 (b) is still blurry, the blind algorithm result in Fig.5.3 (c) has a remarkable contrast between shell and hollow inside of micro-bead. Both transverse (x-y axis) and axial (z axis) diameters of the bead in the deconvolution result are elongated since they do not consider depth-variance.

Their quantitative performance values are summarized in (b) and (c) column in Table.5.3. Their relative contrast values are 86 and 94%, respectively, which is consistent with the qualitative result. Transverse FWHM values of the non-blind and blind deconvolution are 2743 and 2653nm, respectively. Axial FWHM values are 4333 and 3170nm, respectively. The blind algorithm has closer FWHM value to the true diameter (2500) than one of non-blind algorithm. However, their FWHM values still far from the true diameter, which is also in accordance with qualitative performance evaluation result. Their processing time and the used memory are 4.6, 80 minutes and 2.04, 1.82 GB, respectively. Through the qualitative and quantitative performance evaluation in non-blind and blind deconvolution experiments, it is shown that blind deconvolution is more suitable for actual WFM image than non-blind deconvolution. Although computational cost is more required in blind deconvolution, we focused accuracy of deconvolution results.

We depict blind deconvolution results using depth-variant radially symmetric PSF and proposed depth-variant asymmetric PSF in Fig.5.3 (d) and (e). The Fig.5.3 (d) is the result of our previous work and its PSF model is also Gibson and Lanni model. The proposed depth-variant asymmetric PSF is the simplified Zernike polynomial model that is introduced in proposed method section. Both results remove axial blurs that could not be suppressed by using depth-invariant algorithms. However, the result of deconvolution using depth-variant radially symmetric PSF exists artifact. Besides, the shell has a distorted sphere shape. On the contrary to this, the result of deconvolution using depth-variant asymmetric PSF shows a perfect sphere shape and no artifacts. This result shows the validity of asymmetric PSF model.

Quantitative results of blind deconvolution using depth-variant radially symmetric PSF and proposed depth-variant asymmetric PSF are summarized in (d) and (e) column in Table.5.3. The FWHM values are as follows: deconvolution results using radially symmetric PSF (transverse $2655nm$, axial $2349nm$) and asymmetric PSF (transverse $2680nm$, axial $2416nm$). While deconvolution using asymmetric PSF has slightly the worse transverse FWHM, its axial FWHM values has far closer to $2500nm$ than FWHM values of deconvolution using radial symmetric PSF. The relative contrast values of depth-deconvolution result using radially symmetric and asymmetric PSF are 97 and 98%, respectively. The deconvolution using asymmetric PSF is slightly better than the one using radially symmetric PSF. Standard deviation values of FWHM and intensity peak ratio as follows: x-y symmetric ($190.3nm$, 12.8%) and x-y asymmetric PSF ($142.7nm$, 4.4%). In the view of the symmetry, the deconvolution using asymmetric PSF shows remarkable performances. It is consistent with qualitative performance evalution.

Also, we compared actual computational costs in Table.5.3 with expected memory requirements in Table.5.2 that are calculated by formulas in Table.5.1. In case of deconvolution using space-invariant PSF, the difference between actual and expected memory is 1.2GB, approximately. In case of deconvolution using depth-variant PSF, the difference is 2.8GB. Though they are slightly different from expected costs, they are acceptable errors to expect memory requirements. Also, as expected, actual computational costs for the depth-variant image deconvolution requires much larger processing time and memory requirements than invariant ones. Plus, there is no difference of memory requirements between two depth-invariant algorithms or two depth-variant algorithms, which correponds to the expected result in Table.5.2.

We also compare existing algorithm[25] and its deconvolution result is depicted in ISBI12 column in Table.5.3. The existing algorithm excutes blind deconvolution using depth-invariant asymmetric PSF and its PSF model is Zernike polynomial model[43]. While our proposed algorithm simplifies parameters of Zernike polynomial PSF model, our deconvolution result is superior to the existing algorithm. Plus, a quantitative performance comparision between the existing algorithm and our previous (d) algorithm indicates that depth-variance is more significant factor than radial asymmetry. From the deconvolution results described in Table.5.3, Fig. 5.4 and Fig. 5.5, we could draw several conclusions. The more reflects characteristics of PSF, deconvolution algorithm has more remarkable performance in terms of removing axial blur. In view of the relative contrast value, blind deconvolution affected and their results surpass 90%. From standard deviation values in Table.5.3, the blind depth-variant deconvolution using asymmetric PSF has lower standard deviation of both FWHM and intensity peak ratio, this result indicates the validity of applying depth-variant asymmetric PSF.

From Table. 5.3 and Fig. 5.5, it is shown that the depth-variance is critical factor for memory requirement and processing time for step 3. This is because depth-varying convolution in depth-variant deconvolution requires convolution operations as the number of z planes of observed image. Whereas depth-invarying convolution in depth-invariant deconvolution can be computed with only a single convolution. With regard to processing time, not only depth-dependence but also blind deconvolution is critical factor. This is because non-blind deconvolution has a given PSF and it does not require PSF estimation and generation procedures of step 1 and step 2. Processing time for step 2 increases after each adding PSF characteristics. As the method adds depth-variance ((b)→(c)) and asymmetry ((c)→(d)), the processing time for step 2 shows the gradual increase, which is depicted in Fig. 5.5.

The Flowchart is added in Fig.5.6 in order to enhance our experiment understanding. The (b), (c), (d) and (e) in Fig.5.6 correspond to each deconvolution methods in Fig.5.3 and Table.5.3.

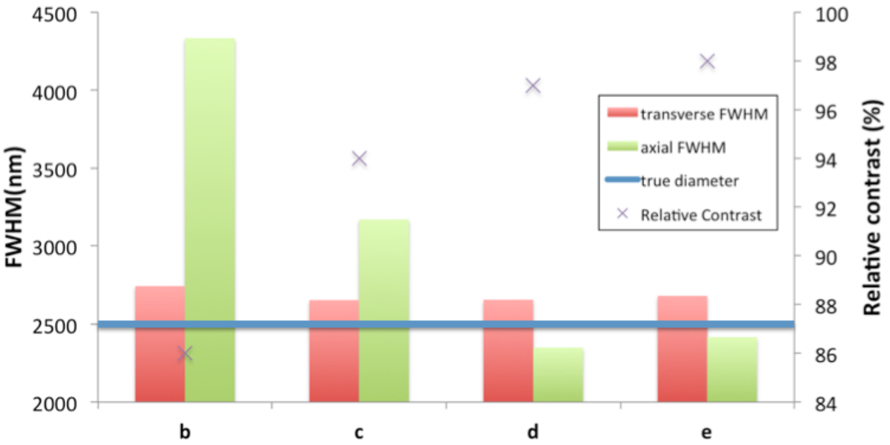

Figure 5.4: FWHM and relative contrast according to deconvolution methods (b) non-blind (downloaded PSF) (c) blind (depth-invariant radial symmetric PSF) (d) blind (depth-variant radial symmetric PSF) (e) blind (depth-variant asymmetric PSF)

5.3.2 Cell Experiment

We tested the proposed algorithm to C. Elegans embryo cell images as biological data, which shows the applicability and the qualitative performance. The dataset is the observation image of a C. Elegans embryo cell with a ×100, $1.4NA$ oil UPlanSApo objective (http://bigwww.epfl.ch/deconvolution/?p=bio). Enough image stacks should be taken to allow overall shape of a specimen to be observed. Unfortunately, the dataset did not satisfy this condition and bring artifacts on boundaries of the restored image. To avoid the boundary effect, a dataset that is pre-processed by a minimum filter is used, which is also used in our previous work. The data cube after pre-processing is composed of $672 \times 712 \times 216$ voxels of size $64.5 \times 64.5 \times 200nm$. The PSF size $(x \times y \times z)$ was set to $151 \times 151 \times 57$ voxels of size $64.5 \times 64.5 \times 200nm$. After deconvolution, the deconvolution result was cropped to the original volume size of $672 \times 712 \times 104$. The dataset was composed of three wavelength image cubes stacks: CY3 (red $634nm$), FITC (green $531nm$) and DAPI (blue $447nm$) staining depicts the point-wise spots of protein, microtubule filaments and chromosomes in the nuclei,

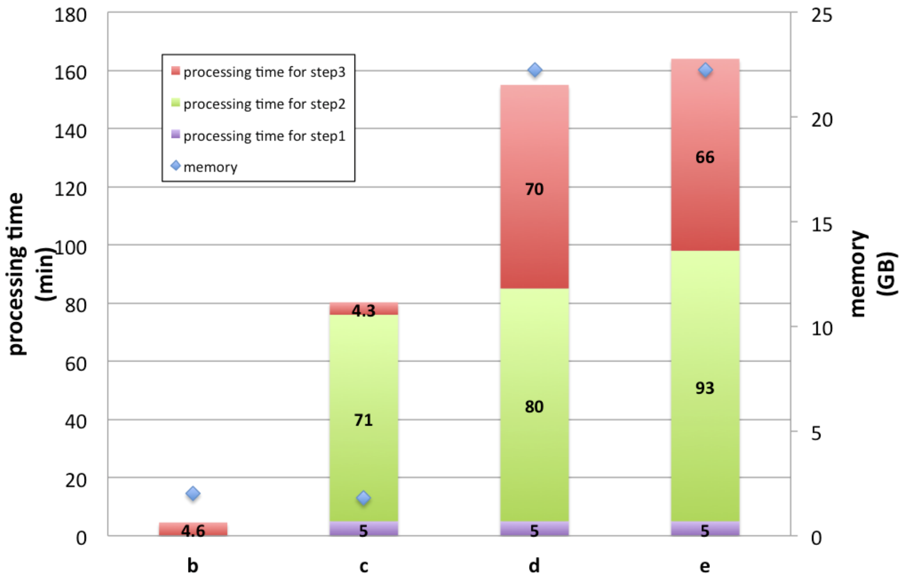

Figure 5.5: Computational cost according to deconvolution methods
(b) non-blind (downloaded PSF) (c) blind (depth-invariant radial symmetric PSF)
(d) blind (depth-variant radial symmetric PSF) (e) blind (depth-variant asymmetric PSF)

respectively. Deconvolution of each wavelength image was implemented. separately. The regularization parameter in cell experiment was set as 0.1×10^{-5}.

We compared deconvolution results between the blind deconvolution using depth-variant radially symmetric PSF (our previous work, Chapter 4) and one using depth-variant asymmetric PSF (proposed), which is depicted in Fig. 5.7 (b) and (c), repectively. Red spots of protein and green microtubule filaments in the deconvolution result using asymmetric PSF has more sharp shapes than one in the deconvolution result using radially symmetric PSF. It is remarkable that artifacts in boundaries of the restoration result using radially symmetric PSF are removed clearly.

5.3.3 Computational Cost according to Image Size

This subsection addresses the computational cost for the C. Elegans embryo cell experiment according to image size. The processing time in this subsection expresses

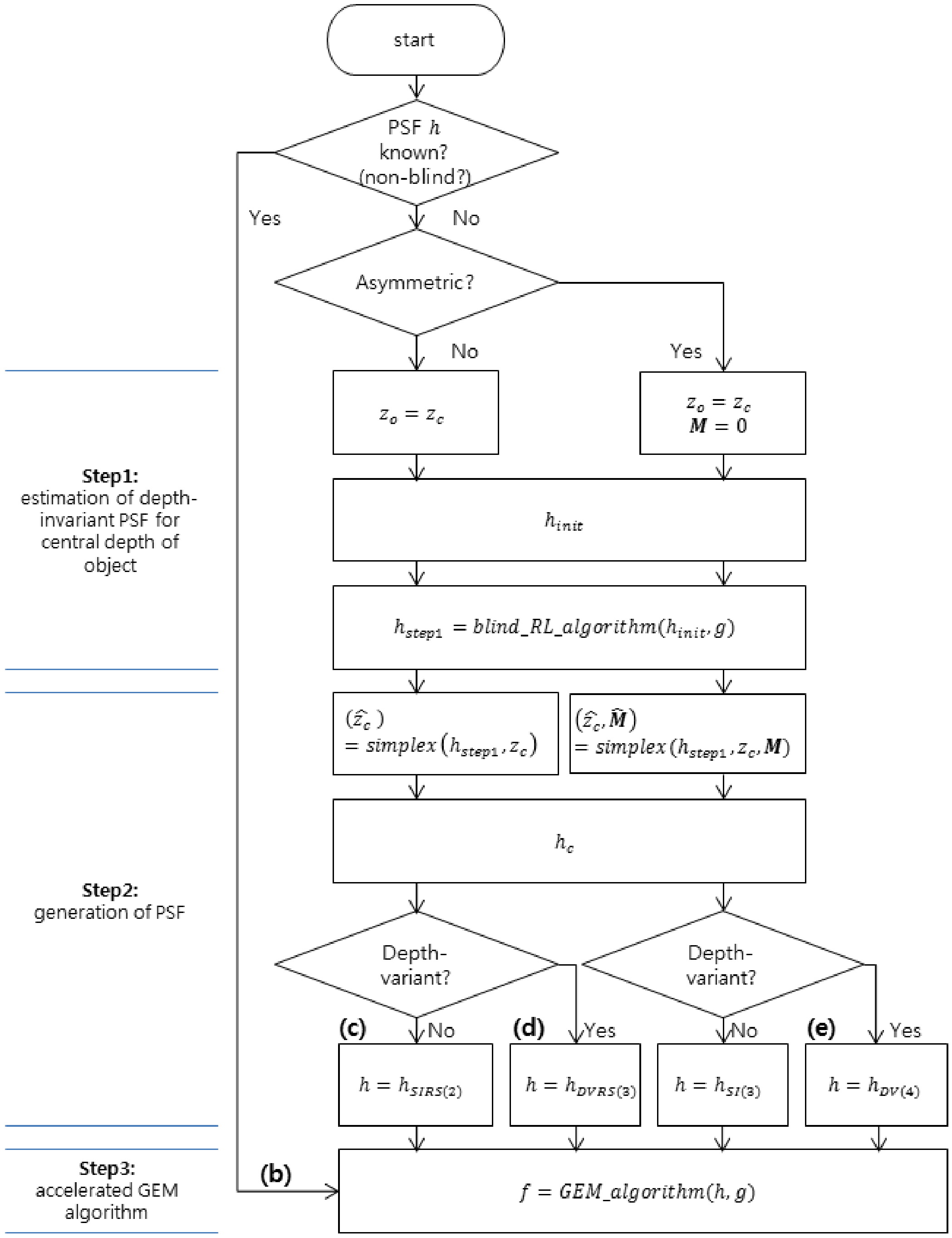

Figure 5.6: Flowchart of methods that are used in bead experiment: (b) Non-blind deconvolution using space invariant radially symmetric PSF (c) Blind deconvolution using space-invariant radially symmetric PSF (d) Blind deconvolution using depth-variant radially symmetric PSF (e) Blind deconvolution using depth-variant asymmetric PSF

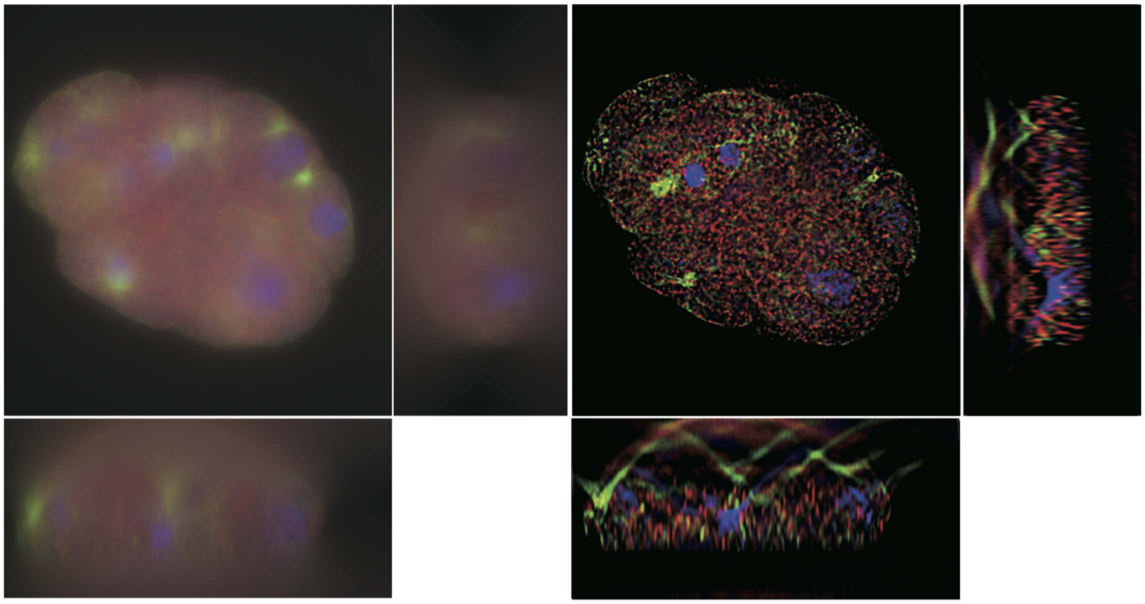

(a) raw data

(b) blind deconvolution using depth-variant radial symmetric PSF

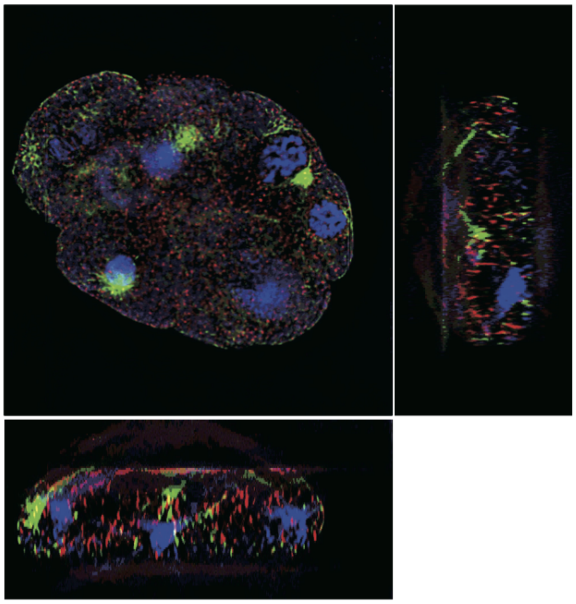

(c) blind deconvolution using depth-variant asymmetric PSF

Figure 5.7: Deconvolution result of C. Elegans embryo cell.

processing time only for step 3. The cell data cube for deconvolution is $672 \times 712 \times 216$ voxels with double data type. Based on Table.5.1, total memory requirements for deconvolution using a space-invariant radially symmetric PSF, depth-variant PSFs and space-variant PSFs are 8GB, 505GB and 228PB, relatively. In the cell experiment, this paper expanded data size for avoiding boundary artifacts. As depicted in the experiment section, we crop the deconvolution result as same as the observed image size after implementation of our algorithm using the preprocessed data. Therefore, expanded area in preprocessed image excutes depth-invariant deconvolution, which can save memory and avoid artifacts on the boundary, simultaneously. The data cube after pre-processing has upper and lower expanded parts along z-axis with original data cube as the center. Memory requirement based on equations in Table.5.1 can be obtained as follows:

$$M_{pre} = XYZ_{pre}(3Z + 8)D \tag{5.4}$$

where M_{pre} and Z_{pre} denote memory requirement for preprocessed data and preprocessed image size on z-axis, respectively. Eq.(5.4) is the sum result of depn-invariant deconvolution in upper and lower expanded parts (image loading: $XYZD$, PSF loading: $2XYZD$, multiple operations: $4XYZD$, total variation: $7XYZD$) and depth-variant deconvolution in original data parts (PSF loading: $XYZZ_{pre}D$, multiple operations: $2XYZZ_{pre}D$. Since image loading and total variation parts are overlapped with depth-invariant deconvolution, their computation can be omitted). Fig. 5.8 depicts a computational cost according to x-y image size. All procedures were carried out in MATLAB 2014a on parallel Intel Xeon E5-2680 processors (2.8 GHz) 448GB RAM, running Windows 8. Memory and time for implementation of the proposed algorithm increase proportionally to x-y image size. Memory and time increase as increase rate of the image size. Fig. 5.8 shows that deconvolution with a twice increased image size needs a twice increased memory and time. It is consistent with our calculation in Eq.(5.4).

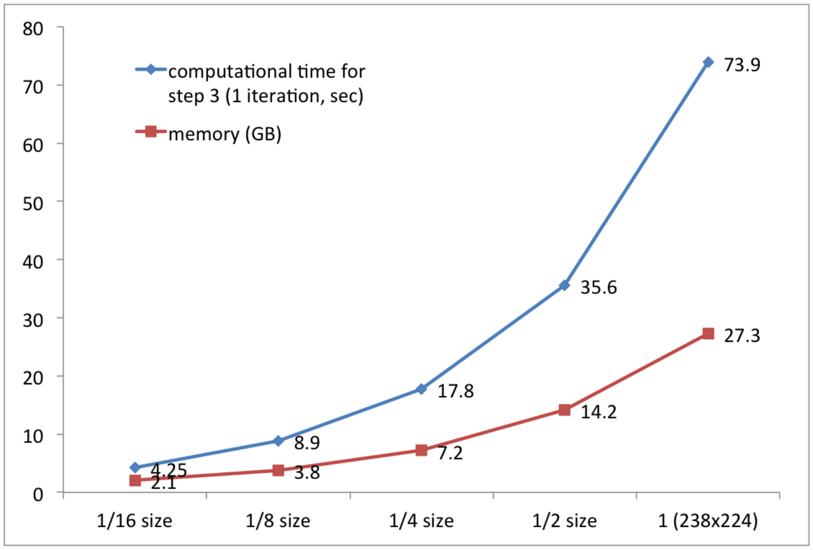

Figure 5.8: Computational cost according to x-y image size

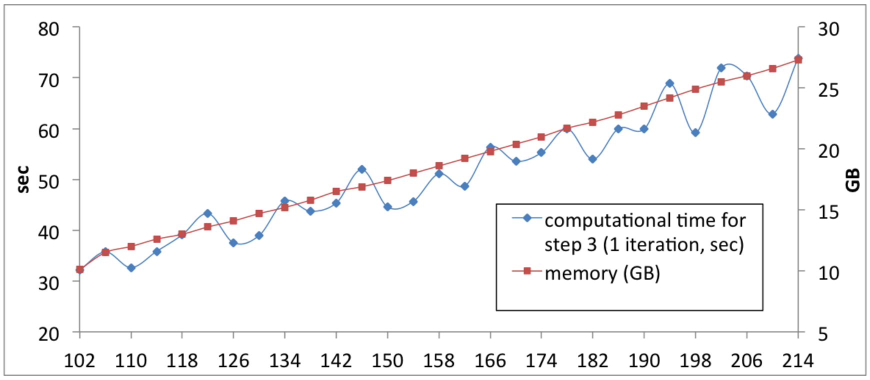

Figure 5.9: Computational cost according to z image size

Fig. 5.9 depicts a computational cost according to z image size. Memory and time for implementation of deconvolution algorithm also increase proportionally to z image size. In case of 238×224 pixel size x-y image, as 1 pixel size increases in z-axis, computational time and memory increases 0.357 sec and 0.143GB, respectively. As shown in Fig. 5.8 and Fig.5.9, the z image size has an effects on greater time and memory than x-y size. This is because the increase of z image size means increase of z_{im} and z_{pre} in Eq.(5.4).

The preprocessed cell data in this paper has $712 \times 672 \times 214$ pixel size, its x-y resolution should be 9 times of the depicted 238×224 size in Fig. 5.8. Using Eq.(5.4), we can caculate expected memory size for our algorithm. Supposing double precision (8 byte), the memory size should be 244GB ($712 \times 672 \times 214 \times (3 \times 104 + 8) \times 8$ byte), approximately. As we expected, the experiment took up 11 minites per 1 iteration and 246GB memory, the computational cost is 9 times of the depicted 238x224 size in Fig.5.8 and Fig.5.9.

5.4 Discussion and Conclusion

The proposed method in this chapter removes blur clearly and solves distortion problem via blind deconvolution algorithm using depth-variant asymmetric PSF. The PSF of the proposed method is consist of distorted pupil function and aberration function that refractive index mismatch induces, its parameters express asymmetry and depth-variance of PSF, effectively.

To obtain suitable parameters of the PSF model, the proposed algorithm estimates PSF and specimen function using the observed image. The observed image indicates a rough location of object. From this information, the proposed algorithm generates initial PSF for central location of the object. Then, RL algorithm modifies the PSF and a simplex algorithm parameterizes the modified PSF. Subsequently, depth-variant PSFs are generated by shifting depth parameters and they are used for deconvolution algorithm. The deconvolution algorithm in the proposed method is an accelerated GEM algorithm.

While the proposed algorithm simplifies parameters of Zernike polynomial model, it supresses distortions and asymmetry that are remained problem in deconvolution using radially symmetric PSF. Moreover, the proposed algorithm performance surpasses one of previous works including existing algorithm using non-simplified Zernike polynomial PSF. Performance is verified through experiments of micro-bead that has determined diameter and hollow sphere shape. The accuracy of the deconvolution results is evaluated by the FWHM (diameter) and relative contrast of the deconvolution results since the dataset is an observation of a micro-bead given diameter and hollow sphere shape. The symmetry of the deconvolution results is evaluated by standard deviations of the FWHM (diameter) and intensity peak ratios.

Not only deconvolution performance but also computational costs for each algorithms are handled in this paper. Also, the specific computational cost according to algorithms and image size is described, which enables users to predict the computational cost.

The work in this chapter would have wide application in images including space-variant blurs. Images of Hubble space telescope wide-field/planetary camera can be possible application examples.

Chapter 6

Conclusion

6.1 Summary

In order to overcome the resolution limit in WFM, in this thesis, deconvolution algorithms, which can remove out-of-focus blurs and correct distortions, are proposed and implemented on a PC. By introduction practical algorithm to WFM and improving PSF estimation, novel deconvolution algorithms for 3D WFM are developed as shown in Table.6.1.

Table 6.1: Overview of the deconvolution algorithms proposed in this thesis

		Proposal 1	Proposal 2	Proposal 3
Practical image deconvolution		✓	✓	✓
PSF	Depth-variance	✓	✓	✓
	Specimen-dependence		✓	✓
	xyz Asymmetry			✓

Proposal 1: Depth-variant Deconvolution

The first work proposes a depth-variant deconvolution based on single PSF pre-measurement. As fitting a formulated Gibson's PSF to a pre-measured PSF, the proposal 1 can get a parameterized PSF. Adjusting z coordinates in the parameterized PSF enables to obtain depth-variant practical PSFs with ease. Existing methods - experimental PSF and formulated PSF have limitations such as noise existence and unknown parameters; thereby they could not apply to actual images. Using the obtained depth-variant PSFs, the author first brought a GEM algorithm to WFM. The GEM accurately estimates the object image and avoids the ill-posed problem. In this work, performance evaluation is implemented by MSE and COR values through simulation experiments. The deconvolution result shows the axial elongation that could not be suppressed by existing depth-invariant methods is suppressed. Also, the deconvolution result of GEM algorithm shows noise robust performance than existing algorithm. The proposed deconvolution algorithm GEM algorithm based on depth-variant imaging model estimates the object image with appropriate noise model and imaging model for 3D thick specimen, which is superior to existing algorithms. The GEM algorithm is also used following proposals.

Proposal 2: Blind Deconvolution using Depth-variant PSF

The second work proposes depth-variant PSF estimation from the observed image. The refractive index and focal distance are changed since the point-like object sample for the pre-measurement and the actual specimen is different. The remained blur in deconvolution result using the first work refers the inaccuracy of pre-measured PSF. The method first estimates the position of the object roughly from an intensity analysis of the observed image. Then, the initial PSF is generated based on the roughly estimated object position. A maximum likelihood function estimator finds the precise depth-invariant PSF from the initial PSF. The fitting of the parameterized

Gibson's PSF model to the precise depth-invariant PSF is implemented by simplex method, which enables to simply generate practical depth-variant PSFs. Adjusting z coordinates in the parameterized PSF model generates depth-variant PSFs. The GEM deconvolution algorithm in this work is modified to converge the objective function fast and save an implementation time. In case of the blind deconvolution for actual image, MSE and COR values could not be used since the object image is unknown. Therefore, the performances are evaluated by the diameter and the relative contrast of the object since a diameter and hollow sphere shape of the object are known. The quantitative and qualitative evaluation shows that the second proposal suppresses the elongation perfectly.

Proposal 3: Blind Depth-variant Deconvolution using Depth-variant Asymmetric PSF

The third work proposes an asymmetric PSF estimation utilizing a Zernike polynomial PSF model, which prevents to distortion in deconvolution result. The Zernike polynomial model can express the complex depth-variant and asymmetric PSF characteristics by a combination of Zernike polynomials and aberration parameters. Among a lot of aberration parameters, the author limited the parameters as z location in object space, defocus, spherical, x-coma and y-coma aberrations that are major factors to determine a PSF shape. The PSF model in the first and second work covers only spherical and defocus aberration, which has a x-y symmetric shape. First, the method estimates the location of object roughly. Then, the initial depth-invariant PSF is generated based on the roughly estimated object location with no aberration. A maximum likelihood estimator estimates the precise depth-invariant PSF from the initial PSF. To easily obtain practical depth-variant asymmetric PSFs, fitting the parameterized Zernike polynomial PSF model to the estimated PSF is implemented by simplex method. The depth-variant PSFs are obtained by adjusting parameters related to z coordinates. Finally, the accelerated depth-variant GEM deconvolution algorithm is implemented. Performance evaluation is implemented by standard deviation values of diameter and relative contrast along each axis. From standard deviation values, it is shown that the third work suppresses the asymmetric intensity amplification. Finally, the third work summarizes the performance and computational cost according to deconvolution methods, which enables users to select algorithm that has desired performance and computational cost.

Fig. 6.1 depicts summarization of proposed deconvolution algorithms in this thesis.

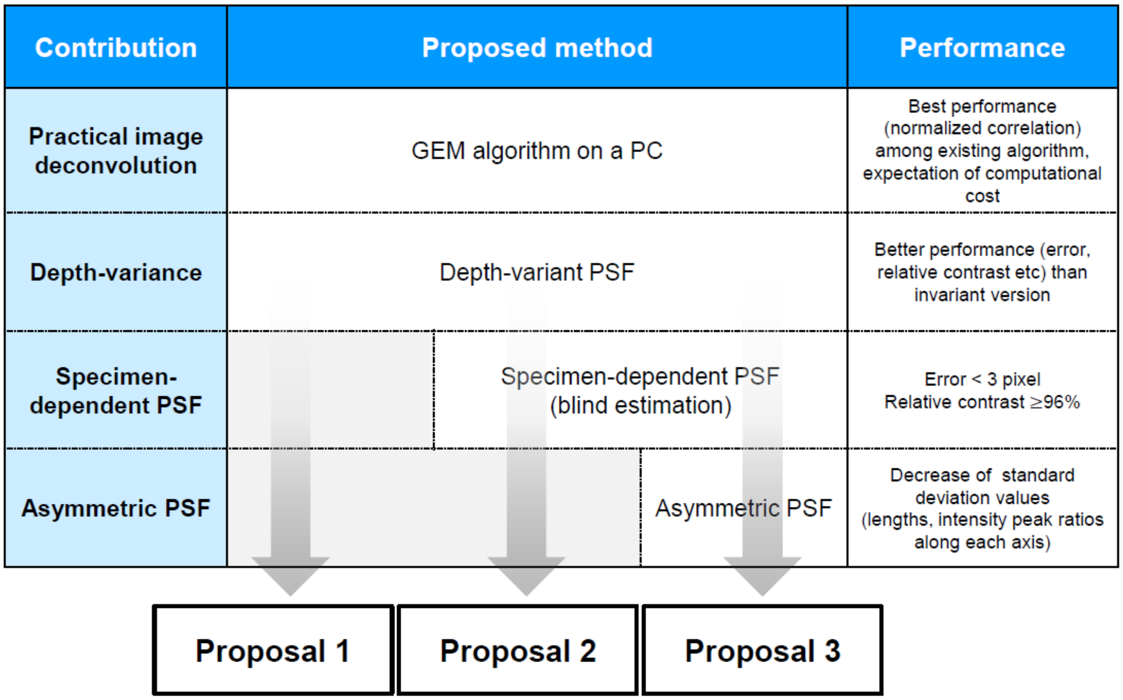

Contribution	Proposed method	Performance
Practical image deconvolution	GEM algorithm on a PC	Best performance (normalized correlation) among existing algorithm, expectation of computational cost
Depth-variance	Depth-variant PSF	Better performance (error, relative contrast etc) than invariant version
Specimen-dependent PSF	Specimen-dependent PSF (blind estimation)	Error < 3 pixel Relative contrast ≥96%
Asymmetric PSF	Asymmetric PSF	Decrease of standard deviation values (lengths, intensity peak ratios along each axis)

Figure 6.1: Summarization of proposed deconvolution algorithms in this thesis

6.2 Future Work

The results of discussion on this dissertation showed the limitations of proposed methods and provided some directions for future works.

Shift-variant deconvolution

To support uneven specimen, shift-invariance of PSF is required. However, proposed PSF models assume that the specimen is composed of even materials. Although the proposed methods cover the difference between specimen and immersion layer, the specimen inhomogeneity is not included. Typically, a targeted live cell is placed in culture medium, which means the inhomogeneity is exist in specimen. Moreover, the targeted cell has various cellular components. These factors cause shift-invariance of PSF. To overcome this problem, shift-variant deconvolution could be an interesting research direction.

PSF estimation using depth-variant PSFs

This thesis generates depth-variant PSFs after finding PSF in the central depth of the object. Proposal 2 and 3 generate a PSF in the central depth from intensity analysis of the observed image and estimate the PSF under the assumption that effect of the illuminations in the central depth is the highest. The PSF estimation is implemented under the depth-invariant imaging model. Then, depth-variant PSFs are generated depending on the estimated PSF in the central depth.

However, in case object illuminations are not concentrated in the central depth, the generated depth-variant PSFs become inaccurate. Particularly, it is difficult to apply our proposed method to an object image that has distributed shape.

For robust PSF estimation regardless of intensities distribution, depth-variant PSF estimation from every depth of the observed image could be a future work. For that, more computational time for the PSF estimation will be required. Therefore, the author believes that the PSF estimation using depth-variant PSFs at several depths would be a solution.

Deconvolution for other fluorescence microscopy

This thesis considered the problem of image deconvolution for WFM images, which can applicable to other microscopy images. While the confocal microscopy has the limitation of slow image acquisition and photobleaching, the confocal has been also widely used for the higher resolution than WFM. To surpass even the high resolution of the confocal microscopy, deconvolution algorithms for that is also has been studied by researchers.

The confocal microscopy has similar properties with those of WFM. The PSF for confocal microscopy also has the depth-variant and asymmetric PSF. Moreover, the noise model follows Poisson distribution. Although PSF modeling for confocal microscopy is slightly different, the properties are same with the WFM. Existing deconvolution methods for confocal microscopy also has similar problems such as local minimum in deconvolution algorithm and blurs[61]. Therefore, the author believes that the proposed methods with transformed PSF for confocal microscopy can be applied to the confocal microscopy images.

For another application to the fluorescence microscopy, stimulated emission depletion (STED) microscopy with proposed deconvolution algorithm can be. Since the STED is one of the fluorescence microscopy, it also follows Poisson distribution with noise, which provides application availability of proposed algorithm. By minimizing the region of illumination at the focal point using the selective deactivation of fluorophores, the STED microscopy can see details smaller than half the wavelength of light could not be resolved by using confocal microscope. As the STED microscopy also has resolution limit, deconvolution for the STED began to appear[62].

Use of images that suffers from depth-variant blurs

Astronomical images taken by Hubble space telescope wide-field/planetary also suffer from the depth-variant blurs. In case of the astronomical images, the specimen becomes the space that is taken.

Also, the medical images such as positron emission tomography (PET) have depth-variance. In case of the PET images, specimen becomes the body that is observed.

PSF for the astronomical and PET images is also varying with the distance from the camera. Proposed deconvolution algorithm with them enables to provide clear images by removing depth-variant blurs.

Real-time implementation

If a real-time implementation is possible, users can observe a clear biological image immediately. The execution time for proposed algorithms is discussed in the chapter 5, yet the algorithm does not operate in real time. An image restoration step for 712x672x214 pixel size needs about 150 minutes and 246GB. Proposed algorithms require convolution operations as much as the number of the observed image stacks. Also, the PSFs are required as the number of the observed image stacks. Naturally, the larger observed image size, the more memory and time are demanded.

For surpass the problem, new shift-variant deconvolution algorithms began to appear[63]. Also, the development of hardware will bring the real-time implementation of proposed algorithm. The real-time of proposed methods will help live cell observations with clear resolution.

Bibliography

[1] P. Sarder and A. Nehorai, "Deconvolution methods for 3-d fluorescence microscopy images," *Signal Processing Magazine, IEEE*, vol. 23, no. 3, pp. 32–45, 2006.

[2] "The Fluorescence Microscope help scientists explore hidden worlds. the nobel foundation. retrieved 2008-09-28.." `http://www.nobelprize.org/educational/physics/microscopes/fluorescence/`. Accessed: 2015-11-30.

[3] "Introduction to Fluorescence Microscopy." `https://www.microscopyu.com/articles/fluorescence/fluorescenceintro.html`. Accessed: 2015-11-30.

[4] D. S. Biggs and M. Andrews, "Acceleration of iterative image restoration algorithms," *Applied optics*, vol. 36, no. 8, pp. 1766–1775, 1997.

[5] J. G. McNally, T. Karpova, J. Cooper, and J. A. Conchello, "Three-dimensional imaging by deconvolution microscopy," *Methods*, vol. 19, no. 3, pp. 373–385, 1999.

[6] J. W. Shaevitz and D. A. Fletcher, "Enhanced three-dimensional deconvolution microscopy using a measured depth-varying point-spread function," *JOSA A*, vol. 24, no. 9, pp. 2622–2627, 2007.

[7] "Scientific Volume Imaging - spherical aberration." `http://www.svi.nl/SphericalAberration`. Accessed: 2014-11-22.

[8] J.-B. Sibarita, "Deconvolution microscopy," in *Microscopy Techniques*, pp. 201–243, Springer, 2005.

[9] J. B. de Monvel, E. Scarfone, S. Le Calvez, and M. Ulfendahl, "Image-adaptive deconvolution for three-dimensional deep biological imaging," *Biophysical journal*, vol. 85, no. 6, pp. 3991–4001, 2003.

[10] J.-A. Conchello and J. W. Lichtman, "Optical sectioning microscopy," *Nature methods*, vol. 2, no. 12, pp. 920–931, 2005.

[11] Rayleigh, "Xxxi. investigations in optics, with special reference to the spectroscope," *Philosophical Magazine Series 5*, vol. 8, no. 49, pp. 261–274, 1879.

[12] C. Preza, M. I. Miller, L. J. Thomas Jr, J. G. McNally, *et al.*, “Regularized linear method for reconstruction of three-dimensional microscopic objects from optical sections,” *JOSA A*, vol. 9, no. 2, pp. 219–228, 1992.

[13] T. Tommasi, A. Diaspro, and B. Bianco, “3-d reconstruction in optical microscopy by a frequency-domain approach,” *Signal processing*, vol. 32, no. 3, pp. 357–366, 1993.

[14] J.-A. Conchello and J. G. McNally, “Fast regularization technique for expectation maximization algorithm for optical sectioning microscopy,” in *Electronic Imaging: Science & Technology*, pp. 199–208, International Society for Optics and Photonics, 1996.

[15] C. Preza and J.-A. Conchello, “Depth-variant maximum-likelihood restoration for three-dimensional fluorescence microscopy,” *JOSA A*, vol. 21, no. 9, pp. 1593–1601, 2004.

[16] C. Preza and V. Myneni, “Quantitative depth-variant imaging for fluorescence microscopy using the cosmos software package,” in *BiOS*, pp. 757003–757003, International Society for Optics and Photonics, 2010.

[17] E. Maalouf, *Contribution to fluorescence microscopy, 3D thick samples deconvolution and depth-variant PSF*. PhD thesis, Université de Haute Alsace-Mulhouse, 2010.

[18] T. J. Holmes, “Blind deconvolution of quantum-limited incoherent imagery: maximum-likelihood approach,” *JOSA A*, vol. 9, no. 7, pp. 1052–1061, 1992.

[19] J. Markham and J.-A. Conchello, “Parametric blind deconvolution: a robust method for the simultaneous estimation of image and blur,” *JOSA A*, vol. 16, no. 10, pp. 2377–2391, 1999.

[20] B. Kim and T. Naemura, “Robust blind deconvolution for fluorescence microscopy using gem algorithm,” in *SPIE Medical Imaging*, pp. 86692L–86692L, International Society for Optics and Photonics, 2013.

[21] S. Joshi and M. I. Miller, “Maximum α posteriori estimation with good’s roughness for three-dimensional optical-sectioning microscopy,” *JOSA A*, vol. 10, no. 5, pp. 1078–1085, 1993.

[22] W. A. Carrington, R. M. Lynch, E. Moore, G. Isenberg, K. E. Fogarty, and F. S. Fay, “Superresolution three-dimensional images of fluorescence in cells with minimal light exposure,” *Science*, vol. 268, no. 5216, pp. 1483–1487, 1995.

[23] V. Krishnamurthi, Y.-H. Liu, S. Bhattacharyya, J. N. Turner, and T. J. Holmes, “Blind deconvolution of fluorescence micrographs by maximum-likelihood estimation,” *Applied optics*, vol. 34, no. 29, pp. 6633–6647, 1995.

[24] T. Kenig, Z. Kam, and A. Feuer, "Blind image deconvolution using machine learning for three-dimensional microscopy," *Pattern Analysis and Machine Intelligence, IEEE Transactions on*, vol. 32, no. 12, pp. 2191–2204, 2010.

[25] F. Soulez, L. Denis, Y. Tourneur, and E. Thiébaut, "Blind deconvolution of 3d data in wide field fluorescence microscopy," in *Biomedical Imaging (ISBI), 2012 9th IEEE International Symposium on*, pp. 1735–1738, IEEE, 2012.

[26] A. Griffa, N. Garin, and D. Sage, "Comparison of deconvolution software: a user point of view–part 2," *GIT Imaging & Microscopy*, vol. 12, no. EPFL-ARTICLE-163628, pp. 41–43, 2010.

[27] J. A. Fessler, "Image reconstruction: Algorithms and analysis," *Under preparation*, 2008.

[28] W. H. Richardson, "Bayesian-based iterative method of image restoration," *JOSA*, vol. 62, no. 1, pp. 55–59, 1972.

[29] L. B. Lucy, "An iterative technique for the rectification of observed distributions," *The astronomical journal*, vol. 79, p. 745, 1974.

[30] J.-F. Aujol, "Some first-order algorithms for total variation based image restoration," *Journal of Mathematical Imaging and Vision*, vol. 34, no. 3, pp. 307–327, 2009.

[31] S. Bonettini and V. Ruggiero, "An alternating extragradient method for total variation-based image restoration from poisson data," *Inverse Problems*, vol. 27, no. 9, p. 095001, 2011.

[32] P. J. Green, "On use of the em for penalized likelihood estimation," *Journal of the Royal Statistical Society. Series B (Methodological)*, pp. 443–452, 1990.

[33] J. A. Fessler and A. O. Hero, "Penalized maximum-likelihood image reconstruction using space-alternating generalized em algorithms," *Image Processing, IEEE Transactions on*, vol. 4, no. 10, pp. 1417–1429, 1995.

[34] J.-H. Chang, J. M. Anderson, and J. Votaw, "Regularized image reconstruction algorithms for positron emission tomography," *Medical Imaging, IEEE Transactions on*, vol. 23, no. 9, pp. 1165–1175, 2004.

[35] P. J. Huber, *Robust statistics.* Springer, 2011.

[36] A. R. De Pierro, "A modified expectation maximization algorithm for penalized likelihood estimation in emission tomography.," *IEEE Transactions on Medical Imaging*, vol. 14, no. 1, pp. 132–137, 1994.

[37] J. Markham and J.-A. Conchello, "Parametric blind deconvolution of microscopic images: Further results," in *BiOS'98 International Biomedical Optics Symposium*, pp. 38–49, International Society for Optics and Photonics, 1998.

[38] C. Preza and J.-A. Conchello, "Image estimation accounting for point-spread function depth cariation in three-dimensional fluorescence microscopy," in *Biomedical Optics 2003*, pp. 135–142, International Society for Optics and Photonics, 2003.

[39] L. Lipson and Tannhauser, *Optical physics*, p. 340. United Kingdom: Cambridge, 1998.

[40] S. Frisken Gibson and F. Lanni, "Experimental test of an analytical model of aberration in an oil-immersion objective lens used in three-dimensional light microscopy," *JOSA A*, vol. 8, no. 10, pp. 1601–1613, 1991.

[41] F. Aguet, D. Van De Ville, and M. Unser, "An accurate psf model with few parameters for axially shift-variant deconvolution," in *Biomedical Imaging: From Nano to Macro, 2008. ISBI 2008. 5th IEEE International Symposium on*, pp. 157–160, IEEE, 2008.

[42] M. Born and E. Wolf, *Principles of optics: electromagnetic theory of propagation, interference and diffraction of light.* Cambridge university press, 1999.

[43] B. Hanser, M. Gustafsson, D. Agard, and J. Sedat, "Phase-retrieved pupil functions in wide-field fluorescence microscopy," *Journal of microscopy*, vol. 216, no. 1, pp. 32–48, 2004.

[44] J. Markham and J.-A. Conchello, "Fast maximum-likelihood image-restoration algorithms for three-dimensional fluorescence microscopy," *JOSA A*, vol. 18, no. 5, pp. 1062–1071, 2001.

[45] P. Pankajakshan, B. Zhang, L. Blanc-Féraud, Z. Kam, J.-C. Olivo-Marin, and J. Zerubia, "Blind deconvolution for diffraction-limited fluorescence microscopy," in *Biomedical Imaging: From Nano to Macro, 2008. ISBI 2008. 5th IEEE International Symposium on*, pp. 740–743, IEEE, 2008.

[46] S. Ben Hadj, L. Blanc-Féraud, G. Aubert, and G. Engler, "Blind restoration of confocal microscopy images in presence of a depth-variant blur and poisson noise," in *Acoustics, Speech and Signal Processing (ICASSP), 2013 IEEE International Conference on*, pp. 915–919, IEEE, 2013.

[47] S. Ben Hadj, L. Blanc-Feraud, E. Maalouf, B. Colicchio, and A. Dieterlen, "Depth-variant image restoration in 3d fluorescence microscopy: two approaches under gaussian and poissonian noise conditions," in *Biomedical Imaging (ISBI), 2012 9th IEEE International Symposium on*, pp. 1671–1674, IEEE, 2012.

[48] S. Ben Hadj and L. Blanc-Féraud, "Modeling and removing depth variant blur in 3d fluorescence microscopy," in *Acoustics, Speech and Signal Processing (ICASSP), 2012 IEEE International Conference on*, pp. 689–692, IEEE, 2012.

[49] P. J. Verveer and T. M. Jovin, "Efficient superresolution restoration algorithms using maximum a posteriori estimations with application to fluorescence microscopy," *JOSA A*, vol. 14, no. 8, p. 1696, 1997.

[50] N. Dey, L. Blanc-Feraud, C. Zimmer, Z. Kam, J.-C. Olivo-Marin, and J. Zerubia, "A deconvolution method for confocal microscopy with total variation regularization," in *Biomedical Imaging: Nano to Macro, 2004. IEEE International Symposium on*, pp. 1223–1226, IEEE, 2004.

[51] B. Kim, D. Kim, and J. Kim, "Psf modeling and image deconvolution for 3d fluorescence microscopy images," in *Korea signal processing conference*, pp. 81–84, Korea Information and Communications Society, 2009.

[52] B. Kim, D. Kim, and J. Kim, "An experimental study on the estimation of depth variant point spread function for fluorescence microscopy," in *Korea signal processing conference*, Korea Information and Communications Society, 2010.

[53] J. C. Lagarias, J. A. Reeds, M. H. Wright, and P. E. Wright, "Convergence properties of the nelder–mead simplex method in low dimensions," *SIAM Journal on optimization*, vol. 9, no. 1, pp. 112–147, 1998.

[54] F. Crimins, "Numerical recipes in c++: The art of scientific computing," *Applied Biochemistry and Biotechnology*, vol. 104, no. 1, pp. 95–96, 2003.

[55] J. Llacer and E. Veklerov, "Feasible images and practical stopping rules for iterative algorithms in emission tomography," *Medical Imaging, IEEE Transactions on*, vol. 8, no. 2, pp. 186–193, 1989.

[56] N. Nguyen, P. Milanfar, and G. Golub, "Efficient generalized cross-validation with applications to parametric image restoration and resolution enhancement," *Image Processing, IEEE Transactions on*, vol. 10, no. 9, pp. 1299–1308, 2001.

[57] F. Aguet, D. Van De Ville, and M. Unser, "A maximum-likelihood formalism for sub-resolution axial localization of fluorescent nanoparticles," *Optics Express*, vol. 13, no. 26, pp. 10503–10522, 2005.

[58] L. Schermelleh, R. Heintzmann, and H. Leonhardt, "A guide to super-resolution fluorescence microscopy," *The Journal of cell biology*, vol. 190, no. 2, pp. 165–175, 2010.

[59] P. Vermeulen, E. Muro, T. Pons, V. Loriette, and A. Fragola, "Adaptive optics for fluorescence wide-field microscopy using spectrally independent guide star and markers," *Journal of biomedical optics*, vol. 16, no. 7, pp. 076019–076019, 2011.

[60] J. Kim, S. An, S. Ahn, and B. Kim, "Depth-variant deconvolution of 3d wide-field fluorescence microscopy using the penalized maximum likelihood estimation method," *Optics express*, vol. 21, no. 23, pp. 27668–27681, 2013.

[61] N. Dey, L. Blanc-Feraud, C. Zimmer, P. Roux, Z. Kam, J.-C. Olivo-Marin, and J. Zerubia, "Richardson–lucy algorithm with total variation regularization for 3d confocal microscope deconvolution," *Microscopy research and technique*, vol. 69, no. 4, pp. 260–266, 2006.

[62] R. Zanella, G. Zanghirati, R. Cavicchioli, L. Zanni, P. Boccacci, M. Bertero, and G. Vicidomini, "Towards real-time image deconvolution: application to confocal and sted microscopy," *Scientific reports*, vol. 3, 2013.

[63] N. Chacko and M. Liebling, "Fast spatially variant deconvolution for optical microscopy via iterative shrinkage thresholding," in *Acoustics, Speech and Signal Processing (ICASSP), 2014 IEEE International Conference on*, pp. 2838–2842, IEEE, 2014.

Publications

Journal Paper

[1] Jeongtae Kim, Suhyeon An, Sohyun Ahn and Boyoung Kim, "Depth-variant deconvolution of 3D widefield fluorescence microscopy using the penalized maximum likelihood estimation method", Opt. Express 21, 27668-27681 (November 18, 2013).
url: https://www.osapublishing.org/oe/fulltext.cfm?uri=oe-21-23-27668& id=274136

[2] Boyoung Kim and Takeshi Naemura, "Blind Depth-variant Deconvolution of 3D Data in Wide-field Fluorescence Microscopy", Scientific Reports 5, Article number: 9894 (May 07, 2015)
url: http://www.nature.com/articles/srep09894

[3] Boyoung Kim and Takeshi Naemura, "Blind Deconvolution of 3D Fluorescence Microscopy using Depth-variant Asymmetric PSF", Microscopy Research and Technique [Submitted]

Conference Paper

[4] Boyoung Kim, Daeun Kim and Jeongtae Kim, "PSF modeling and image deconvolution for 3D fluorescence microscopy images", Korea signal processing conference, Vol 22, No.1, pp81-84 (2009). in Korean

[5] Boyoung Kim and Jeongtae Kim, "An experimental study on the estimation of depth variant point spread function for fluorescence microscopy", Korea signal processing conference, Vol 23 (2010). in Korean

[6] Boyoung Kim and Takeshi Naemura, "Robust blind deconvolution for fluorescence microscopy using GEM algorithm", Proc. SPIE 8669, Medical Imaging 2013. Image Processing, 86692L (March 13, 2013)
url: http://proceedings.spiedigitallibrary.org/proceeding.aspx?articleid=1667564